

POLITECNICO DI MILANO

Scuola di Ingegneria Industriale e dell'Informazione
Corso di Laurea Magistrale in Ingegneria Matematica
Indirizzo Modelli Computazionali in Micro e Nano Elettronica



Electro-Thermal Computational Modeling for 3D Heterogeneous Memory Devices

Relatore: Prof. Riccardo SACCO

Correlatori: Dott. Aurelio MAURI

Prof. Maurizio VERRI

Tesi di Laurea di:
Silvia SORBELLO
Matr. 765222

Anno Accademico 2012-2013

*a mio nonno
che mi ha trasmesso
la passione per la matematica,
e a mia sorella Antonella
che è sempre nei miei pensieri*

Contents

Estratto della Tesi	9
Introduction	12
I Resistive Non-volatile Memories	15
1 Introduction to Resistive Memory Devices	16
1.1 ReRAM Devices	17
1.1.1 Device operation principle	17
1.1.2 Main electrical characteristics	18
1.1.3 Nature of the filament and its implications	19
1.2 PCM Devices	22
1.2.1 Device operation principle	22
1.2.2 Chalcogenide materials properties	24
1.3 General Framework on Reference Memory Devices	26
1.3.1 Electronic module	28
1.3.2 Thermal module	28
1.3.3 Chemical module	29
1.3.4 Mechanical module	29
II Multi-Physics Modeling of Resistive Memories	30
2 Electro-Thermal Model in Heterogeneous Media	31
2.1 Electrical and Thermal Conservation Laws	31
2.1.1 The electric charge conservation law	33
2.1.2 The thermal energy conservation law	37
2.2 Model Derivation	40

<i>CONTENTS</i>	3
-----------------	---

2.2.1	The general Poisson equation	40
2.2.2	Electro-thermal transport	42
2.2.3	Initial conditions	43
2.2.4	Boundary conditions	43
2.3	Generalized Model Form	46
3	Numerical Methods	49
3.1	Time Semi-Discretization	49
3.2	Continuous Weak Formulation	50
3.2.1	General Poisson equation weak form	51
3.2.2	Continuity equation weak form	52
3.2.3	Heat equation weak form	53
3.3	Well-Posedness Analysis	54
3.3.1	General Poisson equation well-posedness	54
3.3.2	Continuity and temperature equation well-posedness	56
3.4	Finite Element Discretization and Matrix Form	58
3.4.1	Galerkin approximation	58
3.4.2	Matrix form	59
3.4.2.1	The stiffness matrix	60
3.4.2.2	The load vector	64
3.4.3	Enforcing the essential boundary conditions	65
III	Simulations and Results	66
4	Implementation Details	67
4.1	Implemented Model and Solution Algorithm	67
4.2	Resistive Memory Cell Geometries	69
4.2.1	The parallelepiped structure	69
4.2.2	The cylindrical structure	73
4.3	Information about the Code	77
5	Validation Tests	79
5.1	Validation of the Poisson Equation	79
5.2	Validation of the Heat Equation	81
5.2.1	Test case 1: variation of the external temperature values	83
5.2.2	Test case 2: variation of the thermal conductivity	83

<i>CONTENTS</i>	4
5.2.3 Test case 3: dominant transport	85
5.2.4 Test case 4: variation of the heat transfer coefficient	86
6 Simulations	93
6.1 Analysis of the Thermal Shift of Electrons	93
6.2 Heterogeneous Properties	98
6.3 Thermo-Electric Transport in the Cylindrical Structure	104
6.3.1 Electric transport	104
6.3.2 Electric field vs thermal field	106
Conclusions and Future Works	110

List of Figures

1	Expectation for the market of the emerging non-volatile memories.	12
1.1	SET and RESET operations in a ReRAM cell.	17
1.2	Exponential dependence of the SET speed on the SET voltage in a ReRAM cell.	19
1.3	$I - V$ curves in a ReRAM device.	20
1.4	Illustration of the power-law dependence of the ON-state resistance R_{ON} on maximum current during SET I_C	20
1.5	Dissolution of the metallic filament in a ReRAM cell during RESET process.	22
1.6	Schematic cross-section of a PCM cell and temperature curves during read and programming operations.	23
1.7	I-V characteristics of SET and RESET states in a PCM cell.	24
1.8	Conductivity in the amorphous and crystalline phases of a PCM cell. .	25
1.9	Schematic diagram of the modules composing the model.	27
2.2	Analysis of the free electron mobility model in a dielectric material. . .	35
2.3	Thermopower absolute values at $T = 300K$	37
2.4	Thermal conductivity of a metal as a function of the temperature. . . .	38
2.5	Thermal conductivity of a non-metal material as a function of the temperature.	39
4.1	General solving algorithm for the model (4.1).	68
4.2	Parallelepiped structure representing a sample resistive memory cell. .	70
4.3	Cross and longitudinal section of the parallelepiped structure.	71
4.4	Parallelepiped structure: illustration of the contacts.	72
4.5	Parallelepiped structure: illustration of the active material portion of the cell.	72
4.6	Cylindrical structure representing a sample resistive memory cell. . .	73

4.7	Cross and longitudinal section of the cylindrical structure.	74
4.8	Cylindrical structure: illustration of the contacts.	75
4.9	Cylindrical structure: illustration of the active material portion of the cell.	75
5.1	Poisson equation validation test: comparison between the potential computed with our code and the solution given by the commercial software in the parallelepiped structure.	80
5.2	Poisson equation validation test: comparison between the potential computed with our code and the solution given by the commercial software in the cylindrical structure.	81
5.3	Temperature equation validation test 1: comparison between analytical solutions and numerical solutions with different values of the external temperatures for the boundary conditions.	87
5.4	Temperature equation validation test 2: comparison between analytical solutions and numerical solutions with different values of the thermal conductivity.	88
5.5	Temperature equation validation test 2: illustration of the duration of the transient regime Δt^{trans} as a function of the thermal conductivity. .	89
5.6	Temperature equation validation test 3: comparison between analytical solutions and numerical solutions with different values of the thermal conductivity.	90
5.7	Temperature equation validation test 4: comparison between analytical solutions and numerical solutions with different values of the heat transfer coefficient.	91
5.8	Temperature equation validation test 4: illustration of the duration of the transient regime Δt^{trans} as a function of the heat transfer coefficient. .	92
6.1	Study of the thermal transport of electrons: temperature fields and corresponding electron concentrations in the active material for different values of the external temperatures in the boundary conditions.	96
6.2	Study of the thermal transport of electrons: electron concentrations along the z -axis for different values of the external temperatures in the boundary conditions.	97
6.3	Study of the thermal transport of electrons: electron concentrations in the active material for different values of the thermopower.	97
6.4	Study of the thermal transport of electrons: electron concentrations along the x -axis for different values of the thermopower.	98

6.5	Test on heterogeneous AM properties: subdivision of the active material in three layers along the z -axis.	99
6.6	Test on heterogeneous AM properties:electrostatic potential.	100
6.7	Test on heterogeneous AM properties:temperature fields and electron concentrations for set A (a-b), set B (c-d), and set C (e-f) of parameters. .	102
6.8	Test on heterogeneous AM properties: comparison of the temperature curves and of the electron concentrations along the z -axis.	103
6.9	Test on the electric transport in the cylindrical cell: potential curves and corresponding electron concentration for different voltage applied. . . .	105
6.10	Test on the thermal-eletric transport in the cylindrical cell: temperature curves and electron concentrations for different values of the external temperatures in the boundary conditions.	108
6.11	Test on the thermal-eletric transport in the cylindrical cell: tempera- ture curves and electron concentrations for different values of the voltage applied to Γ_{C1}	109

List of Tables

2.1	Values of thermal conductivity for different materials at room temperature.	39
5.1	Common parameters values for the one-dimensional model.	83
5.2	Temperature equation validation test 1: common parameters values. . .	83
5.3	Temperature equation validation test 2: common parameters values. . .	84
5.4	Temperature equation validation test 2: values of the Péclet number for different values of the thermal conductivity.	84
5.5	Temperature equation validation test 3: common parameters values. . .	85
5.6	Temperature equation validation test 3: values of the Péclet number for different values of the thermal conductivity.	85
5.7	Temperature equation validation test 4: common parameters values. . .	86
6.1	Study of the thermal transport of electrons: common parameters values for the continuity equation.	94
6.2	Study of the thermal transport of electrons: common parameters values for the temperature equation.	94
6.3	Test on heterogeneous AM properties: values of the common parameters.	99
6.4	Test on heterogeneous AM properties: parameter set A.	99
6.5	Test on heterogeneous AM properties: parameter set B.	100
6.6	Test on heterogeneous AM properties: parameter set C.	100
6.7	Test on the electric transport in the cylindrical cell: parameters values.	104
6.8	Test on the thermal-electric transport in the cylindrical cell: parameters values.	106

Estratto della Tesi

I dispositivi di memoria sono una parte fondamentale dei moderni circuiti integrati VLSI (very-large-scale-integration). Essi vengono classificati in tre categorie a seconda della tipologia di ritenzione dei dati: SRAM (static random-access memory), DRAM (dynamic random-access memory), e NVRAM (non-volatile random-access memory). Le memorie SRAM e DRAM hanno il vantaggio di offrire un rapido accesso (in scrittura e lettura) ai dati contenuti, ma lo svantaggio di mantenere le informazioni solo se alimentate. Al contrario, le memorie non volatili (NVM) garantiscono di conservare l'informazione senza bisogno di alimentazione elettrica.

Dal momento che moltissimi dispositivi (unità USB, smartphones, tablets, dischi a stato solido, computers portatili) richiedono di poter mantenere i propri dati, il campo delle memorie non-volatili è estremamente vasto e in rapida evoluzione, come mostrato in Fig. 1. La necessità di spazi di memoria sempre maggiori si traduce in una forte esigenza di miniaturizzazione (o scalabilità). Tuttavia le memorie tradizionali non sono più in grado di sostenere tale domanda. Diventa perciò indispensabile ricercare nuove tecnologie che possano superarne i limiti e garantire un adeguato trend di scalabilità.

Tra le tante memorie non-volatili emergenti, le memorie di tipo resistivo sono considerate le più promettenti. Questo lavoro di tesi si inserisce nello studio modellistico di due di questi dispositivi (ReRAM e PCM) che viene condotto dalla Micron Technology (azienda leader nel mondo dei semiconduttori) con il duplice obiettivo di:

1. sviluppare un modello matematico che attraverso equazioni alle derivate parziali riesca a descrivere i processi che avvengono all'interno di una cella di memoria,
2. scrivere un codice, usando il linguaggio C++, che gestisca griglie tridimensionali e risolva su queste le equazioni del modello teorico del passo 1.

Dal momento che il progetto generale di comprensione e modellizzazione di tutti i fenomeni fisici coinvolti risulta essere decisamente superiore all'impegno di un lavoro di tesi, ed è inoltre sottoposto a una severa riservatezza per ragioni di confidenzialità,

questo elaborato si concentra sugli aspetti elettrici e termici del funzionamento di una generica cella di memoria di tipo resistivo. In queste memorie lo stato 0 si associa a un alto valore di resistenza elettrica, mentre lo stato 1 corrisponde a un basso valore di resistenza. Grandi sforzi sono stati compiuti per rendere il modello matematico il più generale possibile, in modo tale da fornire un valido strumento con cui poter realizzare simulazioni numeriche nel maggior numero di situazioni e applicazioni possibili.

Il modello matematico proposto è costituito da tre equazioni alle derivate parziali, tempo-dipendenti, che permettono di determinare il potenziale elettrico, la temperatura e la concentrazione di cariche elettriche all'interno della cella di memoria. Nel modello abbiamo tenuto in considerazione non solo la presenza di materiali diversi (metallici e non), ma anche di proprietà eterogenee all'interno dello stesso materiale.

Dopo lo sviluppo del modello teorico ci siamo concentrati sulla sua discretizzazione in tempo e in spazio. Abbiamo posto particolare attenzione nella scelta di metodi numerici in grado di garantire che le proprietà del problema continuo (specialmente il principio del massimo) continuino ad essere valide anche nel problema discreto. Quindi ci siamo occupati di parte dell'implementazione, in linguaggio C++, del modello discreto. Grazie ai dati ottenuti dalla risoluzione delle equazioni è possibile calcolare grandezze fisiche significative per il funzionamento della memoria, in particolare la corrente elettrica che scorre in essa.

Successivamente, per validare il modello teorico e i metodi risolutivi adottati, abbiamo condotto alcuni test in cui le soluzioni numeriche sono state confrontate con soluzioni analitiche note. Infine abbiamo effettuato simulazioni mirate ad analizzare gli aspetti più significativi del modello.

L'elaborato è organizzato nel modo seguente:

Parte I in questa parte descriviamo brevemente le memorie emergenti su cui ci siamo basati per sviluppare il modello, fornendo le informazioni più significative inerenti il loro funzionamento e i fenomeni fisici che vi stanno alla base. Infine presentiamo lo schema concettuale che spiega come sia stato sviluppato il modello in base alle caratteristiche dei dispositivi precedentemente descritti.

Parte II questa parte è costituita da due capitoli. Nel Capitolo 2 viene mostrato il modello matematico teorico sviluppato, con la sua derivazione. Mentre nel

Capitolo 3 sono descritti i metodi numerici che sono stati adottati per la discretizzazione delle equazioni del modello.

Parte III questa parte contiene tutte le informazioni riguardanti la reale implementazione del modello matematico e i risultati delle simulazioni effettuate. Nel Capitolo 4 viene mostrato il modello realmente implementato e l'algoritmo adottato per la risoluzione del sistema non lineare, con alcune informazioni essenziali sul codice. Nel Capitolo 5 sono presentati i test di validazione del modello proposto. Infine nel Capitolo 6 mostriamo i risultati delle simulazioni effettuate.

Introduction

Memory devices are a basic functional block in modern VLSI (very-large-scale-integration) chips. Depending on the retention of information in the cells, they can be classified into three categories: static random-access memory (SRAM), dynamic random-access memory (DRAM), and non-volatile random-access memory (NVRAM). SRAMs and DRAMs offer a fast access to the data, but they keep the information only when they are powered. On the contrary, the non-volatile memories (NVM) ensure to retain the information without needing electrical power.

The field of non-volatile memory technology is extremely broad and rapidly evolving, as shown in Fig. 1, since many devices (USB drivers, smartphones, tablets, PCs and SSDs) require to be able to maintain their data. The demand for larger storage

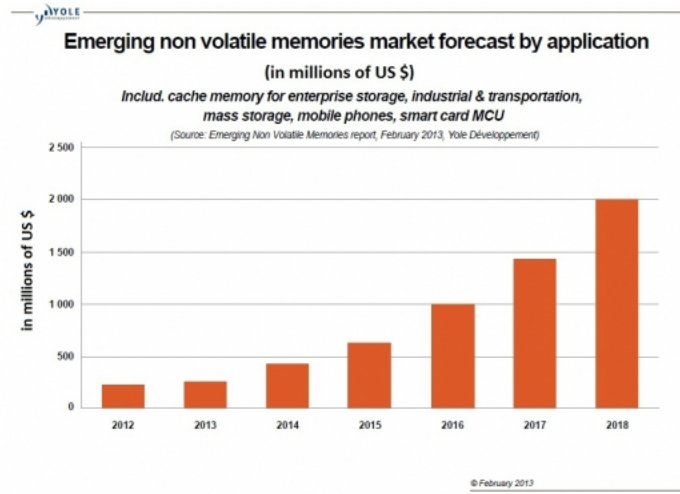


Figure 1: Expectation for the market of the emerging non-volatile memories.

spaces results in a strong need for miniaturization (or scalability). However, the traditional NVM technology is no longer able to sustain such request. Thus it has became indispensable to search for new non-volatile memory devices which can overcome the limitations and ensure a proper trend of scalability.

Among the many emerging NVMs, the resistive type memories are considered the most promising. This thesis work fits in the modeling study of two of these devices (ReRAM and PCM) which is conducted by Micron Technology (a leading company in the semiconductor industry) with the twofold aim:

1. to develop, using partial differential equations, a mathematical theoretical model which can describe what happens inside a memory cell,
2. to write a code in C++ language which can handle three-dimensional meshes and resolve upon them the equations of the previous step.

The general project of understanding and modeling of all physical phenomena involved proves to be far superior to the efforts of a thesis. Moreover it is subject to a strict confidentiality for secrecy reasons. Therefore this work focuses only on the electrical and thermal aspects of the operation of a generic resistive memory cell. In these memories state 0 is associated with a high value of electrical resistance, while state 1 corresponds to a low value of resistance. Great efforts have been accomplished in order to make the mathematical model as general as possible, so as to provide a valuable tool with which one can perform numerical simulations in several different situations and applications.

The proposed mathematical model consists of three partial differential equations, time-dependent, which allow to determine the potential, the temperature and the electric charge concentration within the memory cell. In the model we considered not only the presence of different materials (metals and not), but also heterogeneous properties within the same material.

After developing the theoretical model we focused on its discretization in time and in space. We paid special attention to the choice of the numerical methods in order to ensure that the properties of the continuous problem (in particular, the maximum principle) continue to apply also in the discrete problem. Then we dealt with a part of the implementation, in C++ language, of the discrete model. With the data obtained from the solution of the equations we can compute physical quantities significant to the memory operation, in particular the electric current flowing in the cell.

Then, in order to validate the theoretical model and the adopted solution methods, we conducted some tests in which the numerical solutions were compared to known analytical solutions. Finally, we performed simulations aimed to analyze the most significant aspects of the model.

The thesis is organized as follows:

- Part I** in this part we briefly describe the emerging memories on which we based the development of the model, providing the most important information about their operation, and the physical phenomena that underlie it. Finally, we present the conceptual scheme which explains how the model was developed according to the characteristics of the devices previously described.
- Part II** this part consists of two chapters. In Chapter 2 we show the theoretical mathematical model developed with its derivation. In Chapter 3 we describe the numerical methods that were adopted to discretize the model equations.
- Part III** this part contains all the information regarding the actual implementation of the mathematical model and the results of the simulations performed. In Chapter 4 we show the model actually implemented and the algorithm adopted to solve the non-linear system, with some basic information on the code. In Chapter 5 we present the validation tests of the proposed model. Finally, in Chapter 6, we show the simulation results.

Part I

Resistive Non-volatile Memories

Chapter 1

Introduction to Resistive Memory Devices

As we mentioned in the introduction, the market for non-volatile memories is expected to grow. However traditional Flash memories can not sustain this growth. Traditionally, NVMs are based on charge storage devices called floating gate in which the electronic charge has been stored in a floating polysilicon layer. In floating gate devices the bit 0 corresponds to a high threshold voltage (negative stored charge), while bit 1 corresponds to a low threshold voltage (no stored charge) ([1]). The tremendous problem of the scalability of such devices has opened the way to the exploration of the resistive memories which present a very promising new concept for data storage. The basic idea of a resistive memory is to use an electrically switchable resistance element to store the information: the two logical states (SET and RESET) of a bit correspond to different values of the cell resistance. We focused on two emerging resistive memories. One is the resistance (switching) random access memory (ReRAM). The other is the phase change memory (PCM).

ReRAMs rely on the electrochemical dissolution and deposition of an active electrode metal to perform the resistive switching operation. They demonstrate a high potential for scalability, and a decisive advantage is also the fast read, write and erase speed at low voltages and operating currents.

As switchable resistance element, PCMs utilize a phase change material, exploiting the large resistivity contrast between the crystalline (low resistivity) phase and the amorphous (high resistivity) phase. PCMs are now the most mature of the emerging memory technologies.

1.1 ReRAM Devices

1.1.1 Device operation principle

The basic ReRAM cell is a metal-ion conductor-metal (MIM) system, composed of an insulating or resistive material ' I ' (solid electrolyte) sandwiched between two (possibly different) electron conductors ' M '. The two electrodes have different characteristics: one is made from an electrochemically active electrode (AE) metal, such as Ag, Cu, or Ni, the other one is an electrochemically inert counter (CE), such as Pt, Ir, W, or Au. Figure 1.1 schematically shows the principle of operation of a ReRAM memory cell. The distinguishing feature of ReRAM devices is that the active electrode is composed of a metal that can be easily electrochemically dissolved into, and conducted through, the ion conducting layer (I), whereas the counter electrode cannot.

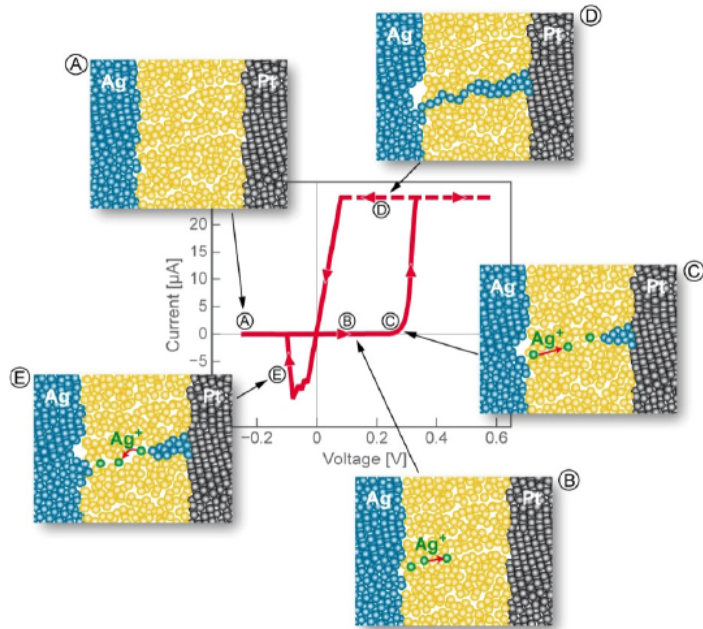


Figure 1.1: Sketch of the steps of the SET (A-D) and RESET (E) operations of a ReRAM cell.

In the initial high resistance state (OFF-state) of the cell no electrodeposit of the metal M is present on the inert electrode or in the electrolyte (Fig. 1.1(A)).

A SET, or programming, process occurs if a sufficiently positive bias voltage is applied to the active electrode allowing the diffusion of the AE metal M through the electrolyte. Then, chemical reactions occur involving M and the free electrons of the electrolyte or the inert electrode (Fig. 1.1(B)). Finally the metal is deposited at the

surface of the CE (Fig. 1.1(C)) and precipitated in the electrolyte. Hence, the SET process can be summarized as follows:

1. anodic dissolution of the metal M according to the reaction



where M^{z+} represents the metal cations in the solid electrolyte thin film;

2. migration of the M^{z+} cations across the solid electrolyte thin film under the action of the high electric field;
3. reduction and electro-crystallization of M on the surface of the inert electrode according to the cathodic deposition reaction



The three processes outlined above lead to the formation of an agglomerate of metal percentiles connecting the two electrodes (Fig. 1.1(D)). After the metal filament has grown sufficiently far to make an electronic contact to the opposite electrode, the cell has switched to the ON-state (Fig. 1.1(D)). The cell retains the ON-state unless a sufficient voltage of opposite polarity is applied and the electrochemical dissolution of the metal filament RESETs the cell (Fig. 1.1(E)) to its initial OFF-state (Fig. 1.1(A)).

The process of the filament formation involves the kinetics of the electrode reactions at both electrodes, i.e. dissolution of the M electrode and deposition of M metal on the inert counter electrode. Depending on the type of solid material used to ensure the ionic transport, the kinetics of the ionic movement may play a crucial role instead of the electrode kinetics. It is evident that these processes must be considered carefully in order to physically describe the cell operation. Therefore, let us analyze the main electrical evidences and the physics behind the filament formation.

1.1.2 Main electrical characteristics

A fundamental characteristic of ReRAM cells is that their SET speed depends strongly on voltage. From the operation principles we know that a cell in its high-resistance (OFF) state can be SET to a low-resistance (ON) state by applying appropriate programming or write voltage pulses V_{wr} . The write voltage V_{wr} should be in the range of a few hundred mV to few V . The length of the write voltage pulses t_{wr} is desired to be

below 100 ns in order to compete with the present devices. As we can see in Fig. 1.2 the time required to SET a ReRAM cell increases exponentially as the voltage is reduced toward zero ([6]).

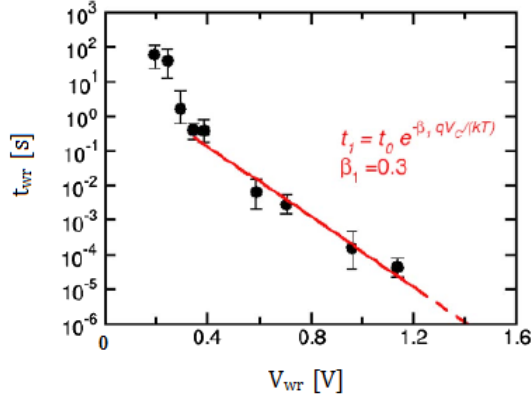


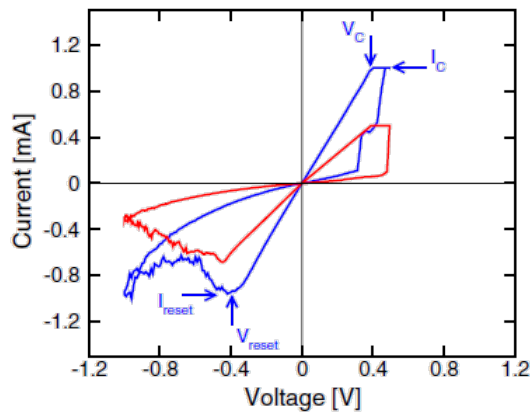
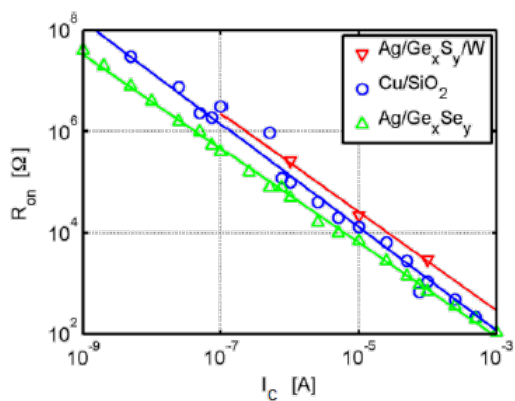
Figure 1.2: Illustration of the exponential dependence of the SET speed on the SET voltage.

Since the state of a ReRAM cell corresponds to a high or low value of its resistance, in order to detect the state of a cell we have to apply a read voltage V_{rd} . To prevent a change of the resistance during the read operation, the read voltage V_{rd} has to be significantly smaller than the write voltage V_{wr} . The read time t_{rd} must be in the order of t_{wr} or preferably shorter. ReRAM arrays with read speeds comparable to $\sim 10\text{ ns}$ and approaching $\sim 1\text{ ns}$ have already been demonstrated for several ReRAM technologies ([6]).

Figure 1.3 shows measured $I - V$ characteristics of a ReRAM device. The SET-state resistance decreases and the RESET current increases for increasing compliance current, that is the maximum current during SET operation ([7]). The monotonic decrease of the SET-state resistance with the maximum current that is allowed to flow through the device during SET, shown in Fig. 1.4, is one of the fundamental characteristics of ReRAMs ([16, 8, 9, 14]). This means that it is possible to build different low resistive states allowing multi-bit programming. Moreover, it seems that this resistance variation is directly correlated with the spatial dimension of the filament.

1.1.3 Nature of the filament and its implications

The abrupt variation of the resistance in ReRAMs is due to the formation of a metallic filament within the cell. Thus the process of filament formation and rupture is still in

Figure 1.3: $I - V$ curves in a ReRAM device.Figure 1.4: Illustration of the power-law dependence of the ON-state resistance R_{ON} on maximum current during SET I_C .

the primary focus of interest in the physical comprehension of the devices operation. First of all, the filamentary nature of the resistive switching effect is widely accepted and up to now no reasonable alternative has been suggested (see [6]). However no direct observation of a complete metal filament in a vertical cell has been published to date. The arguments supporting the formation of metal filament are:

- the drastic change in the conductivity (resistance)
- the possibility to vary the SET resistance (i.e. the filament thickness) by the applied current
- the fact that in most cases the resistance does not scale with the electrode diameter
- the observation that the resistive switching effect occurs only with soluble active electrodes (Ag, Cu) but not with noble metals.

We have already described the formation of the filament, now, considering the RESET operation, we wonder where the bridging metal filament connecting the two electrodes will start to dissolve. Since the active metal is present at both electrodes and forms the bridge, the answer to this question is not obvious. During the RESET operation, negative voltage polarity is applied to the active electrode and a positive polarity is applied to the counter electrode. Besides an electronic current across the metallic bridge, there is an electrochemical current through the electrolyte which is supported by the electrochemical dissolution of the metal M at sites of positive potential, and by the metal M deposition at sites of negative potential at the surface of the metal. Electric fields simulations (see [11]) show that the RESET process starts by dissolution of the metal M at the connective neck formed between the M dendrite and the planar counter electrode, i.e., at the position at which the metal filament first touched the CE during the SET process (Fig. 1.5).

As previously mentioned, the dimension of the filament is not constant in space. It is very likely that the expansion of the metallic filament within the electrolyte causes a large mechanical stress in the ReRAM cell. The stress will depend on the thickness of the metallic filament. To avoid this stress, the metal filament needs to grow in nanopores of the ion conductor. Alternatively, some stress may be released by the formation of the metal filament at the interface of the ion conductor and a neighboring phase.

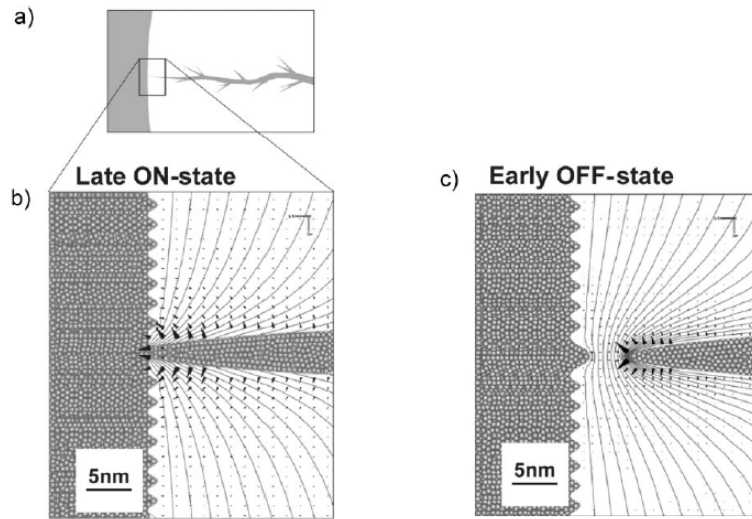


Figure 1.5: Field simulation of the front-most Ag filament touching the Ag electrode shown in a cross-section during the RESET process (a) sketch of the location, b) late ON state, c) early OFF state). The lines are equipotential lines. The black triangles show the direction and strength of the electrical field.

From the brief description we have just provided on ReRAM devices, it is clear that the key points for ReRAMs modeling are:

- electron transport
- ion transport mechanisms
- chemical reactions
- mechanical stress phenomena.

1.2 PCM Devices

1.2.1 Device operation principle

In a PCM device (Fig. 1.6(a)), a phase change material is sandwiched between two metal electrodes, allowing for the application of an electrical voltage and for the consequent phase change between a crystalline (low resistivity) SET state and an amorphous (high resistivity) RESET state. The crystalline phase can be transformed into an amorphous phase by heat-induced melting and fast quenching, resulting in the loss of the

long range order and in the development of a covalently bonded structure. The materials used to achieve the phase variation are typically chalcogenide alloys that are widely employed in the common DVDs.

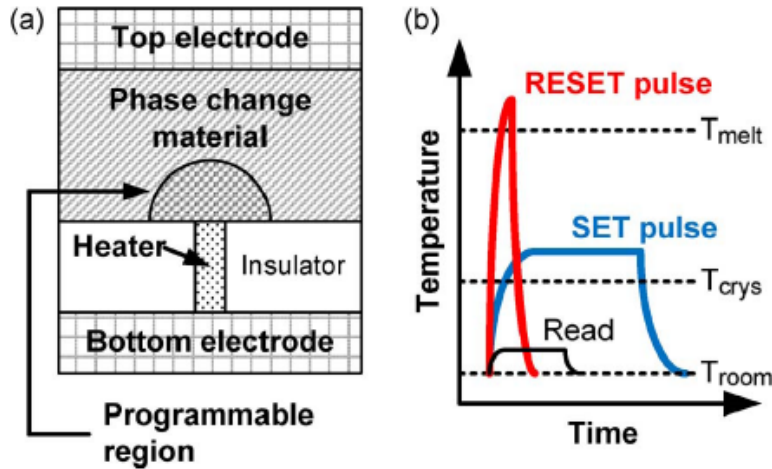


Figure 1.6: (a) Schematic cross-section of the conventional PCM cell. The electrical current passes through the phase change material between the top electrode and the heater. Current crowding at the heater to phase change material contact results in a programmed region illustrated by the mushroom boundary. This is typically referred to as the mushroom cell. (b) PCM cells are programmed and read by applying electrical pulses which change temperature accordingly.

Figure 1.7 shows current–voltage ($I-V$) curves of the SET and RESET states. The SET and RESET states have large resistance contrast for voltages below the threshold switching voltage V_T . The RESET state is in the high-resistance state below V_T (sub threshold region) and shows electronic threshold switching behavior at V_T , i.e., a negative differential resistance. This is reversible if the voltage pulse is removed very quickly. But if the voltage is applied for a longer time than the crystallization time, it leads to memory switching and the cell reaches the low-resistance state for an applied voltage larger than V_T .

The SET process critically depends on an electronic threshold switching effect. When the electric field across the amorphous region reaches a threshold value, the resistance of the amorphous region goes into a lower resistance state which has resistivity comparable to that of the crystalline state. This electronic threshold switching phenomenon is the key to successful SET programming of the PCMs. When the PCM is in the RESET state, its resistance is too high to conduct enough current to provide

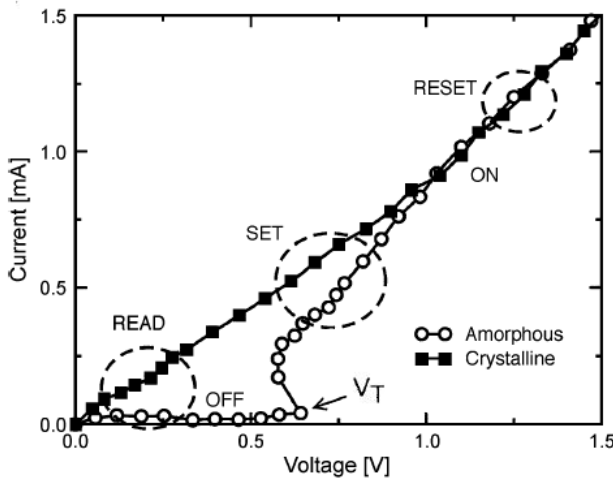


Figure 1.7: I-V characteristics of SET and RESET states in a PCM cell. The RESET state shows switching behavior at the threshold switching voltage. The RESET state stays in the high-resistance state below the threshold voltage (subthreshold region) and switches to the low-resistance state at V_T .

Joule heating to crystallize the PCM cell. The electronic threshold switching effect lowers the resistance of the phase change material to the dynamic resistance and enables SET programming.

RESET programming consumes the largest power since the cell needs to reach the melting temperature. RESET current is determined by various material properties such as the resistivity and thermal conductivity as well as the device structure.

In general, the operating speed of PCMs is limited by the SET programming time because it takes a finite time to fully crystallize the amorphous region. For a more detailed discussion of PCM devices we refer to the literature ([19]-[31]).

Now we describe the most significant properties of the chalcogenide materials exploited in the PCM devices.

1.2.2 Chalcogenide materials properties

Almost any material including metals, semiconductors, and insulators can exist in an amorphous phase and a crystalline phase. However, a very small subset of these materials have simultaneously all the properties that make them useful for data storage technologies where the information is stored in form of the phase of the material. The chalcogenide material is most of the times, a $Ge - Sb - Te$ ternary alloy (GST). The GST alloy has a large contrast between its optical properties in the amorphous phase

and in the crystalline phase. Moreover it can be rapidly and repeatedly switched between the amorphous, low reflectivity and crystalline, high reflectivity phases using laser pulses. Phase change materials have also a large electrical contrast. This large electrical contrast allows for a large on/off ratio in PCM cells. In practical devices the resistance difference between the two phase states is typically two orders of magnitude.

The electrical conduction in the crystalline phase can be described straightforwardly with the drift-diffusion behavior of a doped semiconductor resulting in Ohmic behavior for low voltages. Non-Ohmic behavior of PCM cells for higher voltages can be attributed to Joule heating by the current ([30]). On the other hand, the electrical conductivity in the amorphous phase can be described by thermally activated hopping transport. A Poole–Frenkel transport of carriers through traps leads to a current which is linear with voltage for very small voltages and exponential for high voltages.

Figure 1.8 shows the conductivity of a PCM cell in the amorphous and crystalline state over time. While the conductivity in the crystalline state is nearly constant, in the amorphous state it changes substantially, decreasing with time. The origin of this resistance drift in the amorphous phase is still being debated. Explanations include stress release [25], [26], decrease of defect density [23], shift of the Fermi level, or increase of the band gap [25].

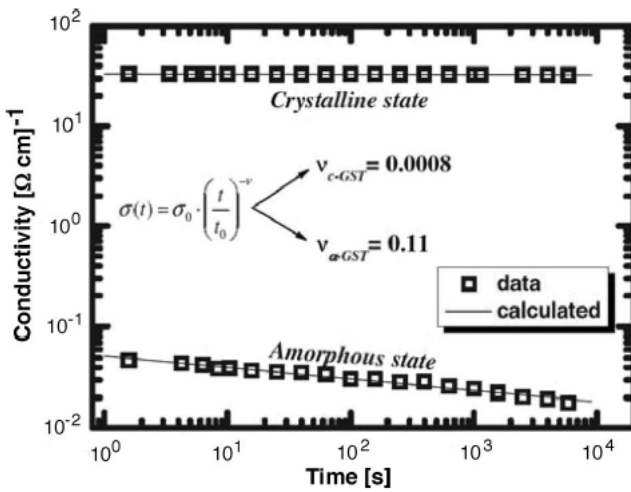


Figure 1.8: Conductivity in the amorphous and crystalline phases of $Ge_2Sb_2Te_5$ as a function of time.

Not only optical and electrical properties are different in respect to the phase, but also thermal properties are related to the material phase. In fact, we have thermal conductivities at room temperature in ranges of $1.4 - 2.9$, $2.8 - 5.5$, and $8.3 - 17.6 \frac{mW}{cmK}$

in the amorphous, rock-salt, and hexagonal phases, respectively ([27]). We point that typical melting temperatures for phase change materials are in the range of 773–1173 K. In PCM devices the role of the temperature is essential to determine not only their properties but also the operations speed: programming, RESET, reading.

It is evident that the physical properties outlined in this section do non depend only on the type of the chalcogenide material, but also on the relative composition of the alloy used in the device itself.

From the characterization of the PCM devices just shown, it is clear that the key points for PCMs modeling are:

- electron transport
- mass transport effect
- thermal phenomena.

1.3 General Framework on Reference Memory Devices

In order to address the investigation of the resistive memory devices, a general framework has been developed. The main phenomena which we outlined are:

1. Mass transport of chemical species (ions in ReRAMs, alloys in PCMs),
2. Thermal phenomena,
3. Electrical conduction,
4. Mechanical stress.

We have also addressed how to consider the heterogeneous properties of materials composing the resistive cells. We decided to model the generic resistive cell as composed of three main material layers: two metals M1 and M2, and an active material layer AM.

The metals represent the device electrodes (active and counter for ReRAMs, top and bottom for PCMs). The AM can consist of multiple layers of different materials. Or it can be made by a single material formed by overlapping planes, each with different

physical or chemical properties. In PCMs the AM layer will be the GST alloy which, in turn, will be formed by various materials with different electrical, thermal and chemical characteristics. In ReRAM devices the AM layer will be the electrolyte/ion conductor.

The cell operation will be controlled by physical processes of electronic, thermal, chemical and mechanical nature. Some processes involve physical quantities defined on the whole structure, while others concern physical phenomena related to a single component of the cell. For instance, transport mechanisms (both electronic and chemical) will take place mainly in the AM layer.

Fig. 1.9 shows the scheme used both in the theoretical model and in the code to describe what happens within a generic resistive cell. Each pattern unit is responsible for managing the processes of one of the four categories, and for interacting with the other modules.

We will now briefly describe each module, reminding that this work focuses on the electronic and thermal aspects of the cell operation in resistive devices. Therefore our mathematical model will include just these two modules and it will not consider their interactions with the others. Finally we want to remark that the mechanical module has not been included in the overall model nor in the code, yet, and it will be the object of a future continuation of the present activity.

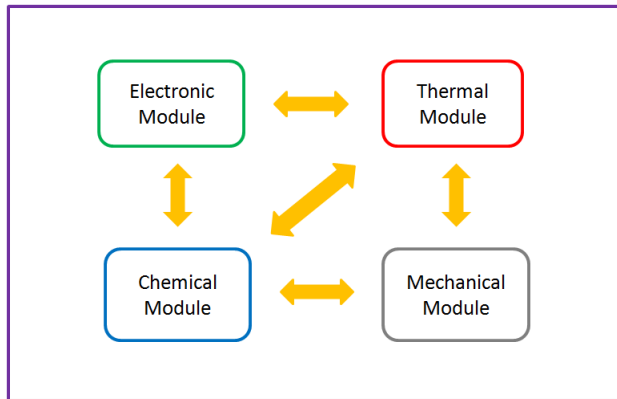


Figure 1.9: Schematic diagram of the modules which compose the theoretical model, and also the code. Three of them (electronic, thermal and chemical module) have already been implemented. One, the mechanical module, has yet to be shaped. The arrows represent the interactions between the modules.

1.3.1 Electronic module

The electronic module is responsible for calculating the electric potential within the structure, and the concentration of charge carriers in the AM layer. It contains one, two or three equations (see [36, 37]).

The first equation to be set up is the Poisson one, which computes the electrostatic potential. The other two equations are the continuity equations for electrons and holes. They compute the electron and hole concentrations, respectively, and they investigate the carriers motion. These equations are not always assembled. In fact holes may not always be present in the cell. Electrons are usually always present in the AM layer, but their concentration might be negligible or their motion may not affect the cell operation. The Poisson equation is solved on the whole cell structure, while the continuity equations are solved just in the active material. This is because in metals the electron concentration is assumed to be constant and holes are completely neglected.

If at least one of the continuity equations is included in the module, then we have a non-linear system to solve. Its resolution requires a linearization method. The method we used is the Gummel map which is a fixed point iteration method ([37]).

The electronic module interacts with the thermal and the chemical module. The Poisson equation requires data about the carrier and ion concentrations to compute the net charge density. On the other hand, the continuity equations require the cell temperature field, because the temperature gradient is considered a driving force for carrier transport, and moreover, the temperature is used to calculate the carrier mobilities and diffusion coefficients. The continuity equations could also include generation or recombination terms due to chemical reaction which involve electrons or holes. Therefore the electronic module will receive feedback from the chemical module and the thermal module.

1.3.2 Thermal module

The thermal module computes the temperature over the entire memory cell. It contains only one equation, the heat equation. This module interacts with all the others. It requires feedback from the electronic module. In fact, we consider not only heat diffusion but we also assume that heat is carried out by the drift current of the electrons. The temperature gradient is considered as a driving force for both charge carrier and ion transport. Therefore the thermal module has to broadcast its outcome to the chemical and the electronic ones.

1.3.3 Chemical module

The chemical module deals with the mass transport within the cell. In particular it provides the concentrations of all the chemical species involved in the cell operation. This module contains a number of equations equal to the number of chemical species involved in the cell operation (which can be also none).

Each equation contains a diffusion term, one or two transport terms, and may contain recombination or generation terms due to the chemical reactions which occur among the species (see [3]). We distinguish two types of chemical species: neutral and ionized. Both of them diffuse, and for both the temperature gradient represents a driving force of their transport. In addition ionized species are moved by the electric field which, of course, does not affect the neutral species. We assume that the diffusion and the transport of chemical species occur only in the AM layer, so the chemical equations are solved only in it.

The chemical module interacts with all the others as previously described.

1.3.4 Mechanical module

Since there could be very significant changes in temperature (PCM) and phase (PCM, the metallic filament formation and rupture in ReRAM) in the cell, it is very likely that the mechanical stress significantly affects the memory cell operation. Therefore a mechanical module has been included within the model. In order to quantify the phase and temperature changes occurred within the cell, the mechanical module will need information about the concentrations of the chemical species and the temperature, from the chemical and the thermal modules, respectively.

Stress is usually correlated with various effects on materials, possibly including changes in physical and electrical properties. For instance, many materials exhibit stress dependence through the mobility or the number of charge carriers as a function of the volume of the material. Volume changes affect the energy gap between the valence and the conduction band. Hence, the number of carriers and the resistivity change. Then, it is equally evident that a stress analysis can provide important information about parameters used in other modules.

Part II

Multi-Physics Modeling of Resistive Memories

Chapter 2

Electro-Thermal Model in Heterogeneous Media

The aim of the model proposed in this work is to investigate the electrical and thermal processes which take place in a generic resistive memory cell. In particular our purpose is to compute the electrostatic potential φ , the electron concentration n and the temperature field T within the cell. The three physical quantities influence each other. The model also allows to treat materials with very different characteristics, and moreover, to handle heterogeneous properties within the same material.

The computational domain representing the generic cell is quite simple (Fig. 2.1). At the upper and lower ends of the cell there are the metal electrodes (Ω_{M1} and Ω_{M2}). Between them there is the active material (Ω_{AM}). We focus on one single cell, but it is also important to remember that a memory is composed by an array of bits. Therefore we decided to introduce a dielectric material which will aim to isolate each cell from its neighbours. The active material of each cell will then be surrounded by an insulator (Ω_d). We also define the following interfaces: $\Gamma_{m1} = \Omega_{AM} \cap \Omega_{M1}$, $\Gamma_{m2} = \Omega_{AM} \cap \Omega_{M2}$, $\Gamma_{diel} = \Omega_{AM} \cap \Omega_d$, $\Gamma_{diel-met} = \{\Omega_{M1} \cap \Omega_d\} \cup \{\Omega_{M2} \cap \Omega_d\}$. The global domain is $\Omega = \Omega_{M1} \cup \Omega_{M2} \cup \Omega_{AM} \cup \Omega_d$, with $\partial\Omega = \Gamma_{C1} \cup \Gamma_{C2} \cup \Gamma_{ext}$.

We will now proceed showing the derivation of the mathematical model.

2.1 Electrical and Thermal Conservation Laws

The electron concentration and the temperature field are determined by the solution of suitable conservation laws. A generic conservation law states that a particular measurable property of an isolated physical system does not change as the system evolves.

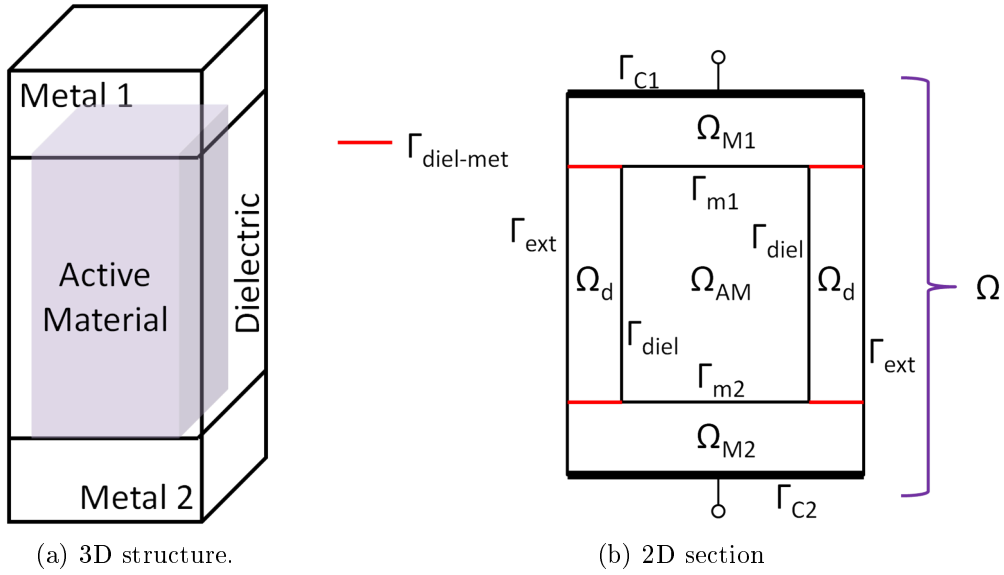


Figure 2.1: Computational domain representing a generic resistive memory cell.

Let $\Upsilon \subset \mathbb{R}^3$ be the computational domain representing the isolated physical system, and let $u : \Upsilon \rightarrow \mathbb{R}$ be a scalar physical quantity which is conserved within the system. Then we can write the following conservation law

$$\frac{\partial u}{\partial t} + \operatorname{div} \mathbf{j}_u(u) = \mathcal{N}_u \quad \text{in } \Upsilon \quad (2.1)$$

where t is the time, \mathbf{j}_u represents the vector flux function of the quantity u , and \mathcal{N}_u is the net production rate of the quantity u . It is evident that Eq. (2.1) states that the quantity u is conserved in Υ . In fact, integrating over the domain, we obtain

$$\frac{\partial}{\partial t} \int_{\Upsilon} u d\mathbf{x} = - \int_{\partial\Upsilon} \mathbf{j}_u(u) \cdot \boldsymbol{\nu} d\sigma + \int_{\Upsilon} \mathcal{N}_u d\mathbf{x} \quad (2.2)$$

$\boldsymbol{\nu}$ being the outward unit normal vector to the domain boundary $\partial\Upsilon$. Eq. (2.2) equals the time rate of change of $\int_{\Upsilon} u d\mathbf{x}$ to the outward flux of \mathbf{j}_u through $\partial\Upsilon$ plus the net generated quantity $\int_{\Upsilon} \mathcal{N}_u d\mathbf{x}$.

We consider the memory cell as an isolated system, and we write two conservation laws, one formulating the conservation of the electrical charge and one stating the conservation of the thermal energy.

2.1.1 The electric charge conservation law

Consider equation (2.1): $\Upsilon = \Omega$ will represent the whole cell, while u will be the electric charge density ρ associated to a charge carrier species. In general we can express ρ as $\rho = qC$, where q is the charge ($[C]$) of an electron, and C is the concentration ($[cm^{-3}]$) of the charge carrier. We consider two charge carrier species: electrons and holes. In the case of the electrons we note C as n , while, in the case of the holes we note C as p . We will describe only the conservation law associated with the electron species, since the one related to the holes does not show significant differences. In this work we do not consider chemical reactions involving electrons nor the presence of holes in the active material, thus we will assume $\mathcal{N}_n = 0$. Writing Eq. (2.1) in the case u = electron charge density, we obtain

$$-q\frac{\partial n}{\partial t} + \operatorname{div}\mathbf{j}_n = 0 \quad \text{in } \Omega_{AM} \quad (2.3)$$

$$\operatorname{div}\mathbf{j}_n = 0 \quad \text{in } \Omega_{M1} \cup \Omega_{M2}. \quad (2.4)$$

Eq. (2.3) is the well known electron continuity equation. The electric charge conservation law is not imposed in Ω_d because in an ideal dielectric there are no free mobile charges. Since in metals the number of conducting electrons is constant, and there are not recombination/generation mechanisms, we have that equation (2.3) degenerates into (2.4).

The flux function \mathbf{j}_n is the electron current density ($[C cm^{-2}s^{-1}]$) which has the following phenomenological definition ([33, 34])

$$\mathbf{j}_n = \mathbf{j}_n^{el} + \mathbf{j}_n^{th}. \quad (2.5)$$

This relation expresses the total electron current density as the sum of two contributions. One contribution (\mathbf{j}_n^{el}) is of electrical nature, while the other (\mathbf{j}_n^{th}) is of thermal nature.

The electrical contribution represents the traditional drift-diffusion current density:

$$\mathbf{j}_n^{el} = q D_n \nabla n - q \mu_n n \nabla \varphi \quad (2.6)$$

where D_n is the electron diffusion coefficient ($[cm^2/s]$) and μ_n the electron mobility ($[cm^2 V^{-1}s^{-1}]$). The drift-diffusion model for the electron current density can be derived exploiting the Boltzmann transport equation, through a linearization of the distribution

function in phase space around its equilibrium value (see [36]). Eq. (2.6) states that the electron current density is formed by two terms. The former is the diffusion term which expresses the tendency of electrons to move towards the spots where their concentration is lower. The latter is the drift term which expresses the motion of electrons due to an applied electric field ($\mathbf{E} = -\nabla\varphi$).

Several different models can be used in order to represent the electron mobility. This quantity characterizes how quickly an electron can move in a material when pulled by an electric field. We described the electron mobility with the following approach ([38]):

$$\mu_n = \mu_n(E, T) = \frac{\mu_0}{\left[1 + \left(\mu_0 \frac{E}{v_{sat}}\right)^\beta\right]^{1/\beta}} \quad (2.7)$$

where

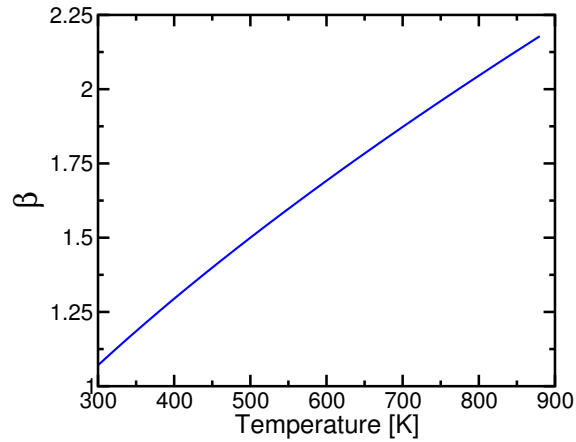
$$\beta = 1.109 \left(\frac{T}{300}\right)^{0.66}, \quad (2.8)$$

E is the magnitude of the electric field \mathbf{E} , μ_0 is a reference value of the carrier mobility in the active material (it could also be space dependent), and v_{sat} is the magnitude of the saturation velocity \mathbf{v}_{sat} . The velocity saturation is a phenomenon occurring at high electric fields regime (see [2, 36]). It is evident that the drift velocity of the charge carriers increases as the electric field increases, but this growth is limited. At high fields, the average carrier energy increases and electrons lose their energy by optical-phonon emission nearly as fast as they gain it from the field. This results in a decrease of the carriers velocity until the drift velocity reaches a limit value $v_{sat} \approx 10^7 \text{ cm/s}$. Eq. (2.7) represents a simplified version of the model reported in [38], able to include temperature and electric field effects on carrier transport. Figure 2.2 is useful to understand the mobility model of Eq. 2.7. As we can see, the parameter β increases as the temperature increases (Fig. 2.2(a)), resulting in a rise of electron mobility (Fig. 2.2(b)) when the applied electric field is constant and the parameters v_{sat} and μ_0 are fixed. As regards the field dependence, Fig. 2.2(c) shows that the electron mobility decreases as the electric field increases, when the temperature is constant and the parameters v_{sat} and μ_0 are fixed. Finally we use the mobility to obtain the diffusion coefficient. In fact, in order to compute the diffusivity, we use the Einstein relation ([36])

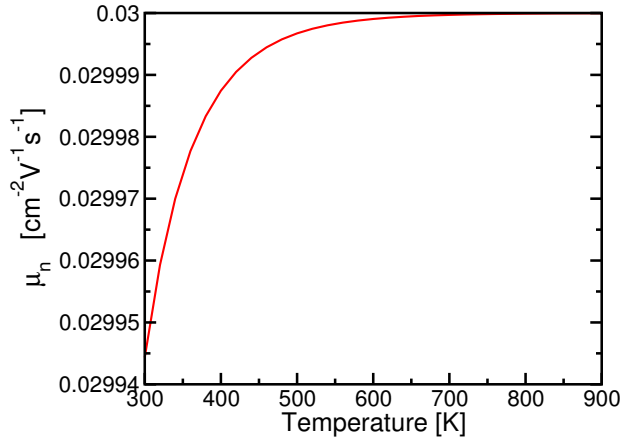
$$D_n = \mu_n \frac{k_B T}{q} \quad (2.9)$$

where k_B is the Boltzmann constant.

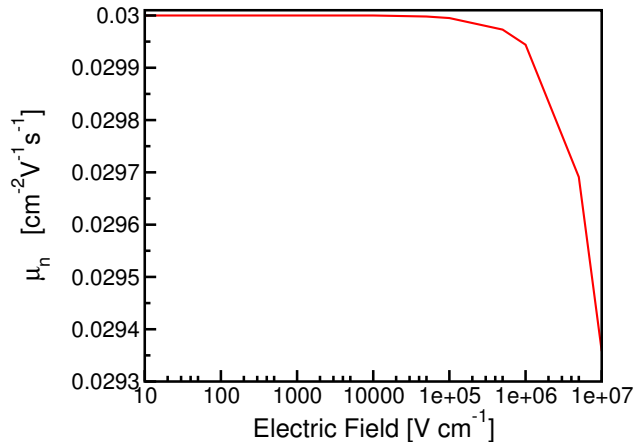
We assume that the above formulas (Eq. (2.6) and (2.7)) and the Einstein relation,



(a) Parameter β as a function of temperature.



(b) Electron mobility dependence on the temperature. All other model parameters are set: $E = 10^6 \text{ V/cm}$, $v_{sat} = 10^7 \text{ cm/s}$, and $\mu_0 = 0.03 \text{ cm}^2 \text{V}^{-1} \text{s}^{-1}$.



(c) Electron mobility dependence on the electric field. All other model parameters are set: $T = 300 \text{ K}$, $v_{sat} = 10^7 \text{ cm/s}$, and $\mu_0 = 0.03 \text{ cm}^2 \text{V}^{-1} \text{s}^{-1}$.

Figure 2.2: Analysis of the free electron mobility model in a dielectric material.

which hold for semiconductors, also apply for dielectric materials, until macroscopic evidences indicate otherwise. Thus we adapt the model to different materials simply by changing the value of μ_0 , and, eventually, by changing v_{sat} or the β model (2.8).

The electrical conductivity σ_n ($[S/cm]$) measures the ability of a material to conduct an electric current. It is related to the density of charge carriers and their mobility, in the case of electrons it is given by

$$\sigma_n = q n \mu_n . \quad (2.10)$$

In metals the conductivity is constant and has a very large value, of the order of $10^6 S/cm$ ([40]). Whereas, for other materials, the electrical conductivity will be spatial dependent since both the electron concentration and mobility vary according to the position in space.

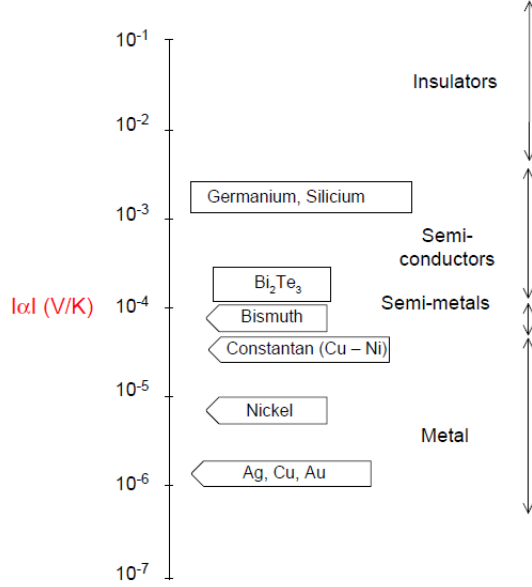
The thermal contribution to the total current can be written as ([33])

$$\mathbf{j}_n^{th} = -\sigma_n \nabla (-\alpha T) = \sigma_n \nabla (\alpha T) \quad (2.11)$$

where α is the thermopower ($[V/K]$). An applied temperature difference across a material causes the charge carriers in it to diffuse from the hot side to the cold side. Mobile charge carriers migrating to the cold side leave behind their oppositely charged and immobile nuclei at the hot side, thus giving rise to a thermoelectric field $-\nabla (\alpha T)$. The term thermoelectric refers to the fact that the voltage drop is created by a temperature difference.

The ratio of the developed voltage to the temperature difference ($\frac{\Delta V}{\Delta T}$) is related to an intrinsic property of the material called the Seebeck coefficient (α) or thermopower. The Seebeck coefficient is very low for metals, only a few $\mu V/K$, and much larger for semiconductors, typically a few $100 \mu V/K$ ([39]). It can be thought of as the heat per carrier over temperature or more simply the entropy per carrier, $\alpha \approx \frac{1}{q} C_Q$ where C_Q is the specific heat of a single charge carrier. Figure 2.3 shows the values of the Seebeck coefficient at room temperature for different types of materials.

In conclusion we consider three driving forces for the electron current. One is represented by the applied external electric field. One is formed by the concentration gradient of the same electrons. And finally, one is represented by the thermoelectric field induced by the temperature gradient.

Figure 2.3: Thermopower absolute values at $T = 300K$.

2.1.2 The thermal energy conservation law

Thermal energy is the portion of internal energy of a system which is responsible for the temperature of the system, and its density can be written as ([41])

$$\xi = \varrho c T$$

where ϱ is the material mass density ($[Kg/cm^3]$), and c is the specific heat ($[cm^2 s^{-2} K^{-1}]$) of the material. Considering Eq. (2.1), also in this case $\Upsilon = \Omega$ will represent the whole cell, while u will be the thermal energy density ($[J/cm^3]$) ξ of the physical system. We will not consider internal heat generation mechanisms, thus we will have $\mathcal{N}_T = 0$. Then we have

$$\varrho c \frac{\partial T}{\partial t} + \operatorname{div} \mathbf{j}_T = 0 \quad \text{in } \Omega \quad (2.12)$$

The flux function \mathbf{j}_T represents the temperature flux ($[W cm^{-2}]$), i.e., the amount of thermal energy that flows through a unit area per unit time. Following [34, 33], we can identify two contributions, one of electrical nature and one of thermal nature. Therefore \mathbf{j}_T is defined by the following constitutive relation

$$\mathbf{j}_T = \mathbf{j}_T^{th} + \mathbf{j}_T^{el}. \quad (2.13)$$

The thermal contribution to the temperature flux is described by the Fourier law

which states that the time rate of heat transfer through a material is proportional to the negative gradient of the temperature, and to the area through which the heat is flowing. The differential form of Fourier law shows that the local heat flux density is equal to the product of thermal conductivity k ($[W\text{cm}^{-1}\text{K}^{-1}]$) and the negative temperature gradient:

$$\mathbf{j}_T^{th} = -k\nabla T. \quad (2.14)$$

This law states the tendency of the temperature to spread until it settles to a certain equilibrium value, equal at all points of the material. The thermal conductivity is the property of a material to conduct heat. It is influenced by the material phase and temperature. Fig. 2.4 ([40]) shows the behavior of the thermal conductivity in a metal material. In metals conductivity is primarily due to free electrons. At temperatures higher than the Debye temperature (Θ_D), we find the well known Wiedemann-Franz law which states that the ratio k/σ of the thermal to the electrical conductivity of a great number of metals is directly proportional to the temperature. Fig. 2.5 ([40]) shows

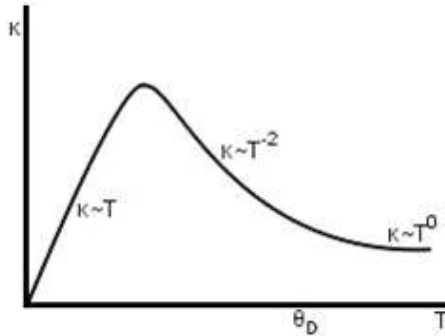


Figure 2.4: Thermal conductivity of a metal as a function of the temperature.

heat conductivity in non metals which is mainly due to lattice vibrations (phonons). At high temperatures, the total number of phonons increases, resulting in a reduction of their mean free path. Therefore the thermal conductivity decreases with increasing temperature. At very low temperatures it rises proportionally to the temperature ($k \sim T^3$), this rise continues until the thermal conductivity reaches a maximum, beyond which it will decline rapidly with increasing temperature. Table 2.1 shows typical values of thermal conductivity for some material at which we are interested when $T \sim 300\text{ K}$.

The second term in (2.13) is related to the fact that we consider electrons as temperature carriers. Each electron has a thermal energy which is transported during its

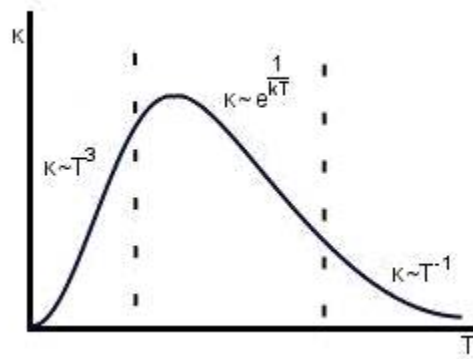


Figure 2.5: Thermal conductivity of a non-metal material as a function of the temperature.

Material	Thermal conductivity k [$W\text{cm}^{-1}\text{K}^{-1}$]
Al_2O_3	0.2-0.3
Pb	0.034-36
Al	2-2.5
Cu	3.8-4
Ti	0.16-0.23
<i>GST</i> alloy	0.002-0.004

Table 2.1: Values of thermal conductivity for different materials at room temperature.

motion. Thus we have a contribution on the temperature flux due to the electron current which can be written as (see [42])

$$\mathbf{j}_T^{el} = (\varphi + \alpha T) \mathbf{j}_n \quad (2.15)$$

where αT is the thermoelectric potential. This contribution represents the convective transport of thermal energy in the direction of the current, opposed to electron motion. Since the main contribution to the electron current is, in Ω_{AM} , the drift term, we replace the total electron current with the drift current:

$$\mathbf{j}_n^{drift,AM} = -q \mu_n n \nabla \varphi, \quad (2.16)$$

while, in metals, the current is simply given by

$$\mathbf{j}_n = -\sigma_n \nabla (\varphi + \alpha T). \quad (2.17)$$

In conclusion we consider two driving forces for the temperature flux: one formed by the gradient of temperature itself, and one represented by the product of the drift electron current and the sum of the thermal and electric potential.

2.2 Model Derivation

2.2.1 The general Poisson equation

In order to compute the electrostatic potential in the memory cell we use a slightly modified version of the Poisson equation, since the Poisson equation, as it is, can not be applied in metals.

The Poisson equation is derived from the Maxwell equations which we recall:

$$\text{rot} \mathbf{H} = \mathbf{J} + \frac{\partial \mathbf{D}}{\partial t} \quad (2.18)$$

$$\text{rot} \mathbf{E} = -\frac{\partial \mathbf{B}}{\partial t} \quad (2.19)$$

$$\text{div} \mathbf{D} = \rho \quad (2.20)$$

$$\operatorname{div} \mathbf{B} = 0 \quad (2.21)$$

where \mathbf{E} is the electric field ($[V\text{ cm}^{-1}]$), \mathbf{D} is the electric displacement field ($[C\text{ cm}^{-2}]$), \mathbf{H} is the magnetic field ($[A\text{ cm}^{-1}]$), \mathbf{B} is the vector magnetic flux ($[T]$), \mathbf{J} is the total current density and ρ is the net charge density. We recall also the constitutive relations:

$$\mathbf{E} = -\nabla\varphi \quad (2.22)$$

$$\mathbf{D} = \epsilon \mathbf{E} \quad (2.23)$$

$$\mathbf{B} = \mu \mathbf{H}$$

where ϵ is the material dielectric permittivity ($[F\text{ cm}^{-1}]$) and μ is the magnetic permeability ($[H\text{ cm}^{-1}]$). Since $\operatorname{div}(\operatorname{rot} \mathbf{A}) = 0$ for any vector \mathbf{A} , Eq. (2.21) is satisfied by introducing a vector potential \mathbf{A} such that $\mathbf{B} = \operatorname{rot} \mathbf{A}$. We replace it in (2.19) and we obtain

$$\operatorname{rot}(\mathbf{E} + \frac{\partial \mathbf{A}}{\partial t}) = 0.$$

From this we can state that exist a scalar potential φ such that

$$\mathbf{E} + \frac{\partial \mathbf{A}}{\partial t} = -\nabla\varphi. \quad (2.24)$$

We multiply (2.24) by ϵ , we apply the divergence operator and we obtain using (2.22), (2.23) and (2.20)

$$\rho + \frac{\partial \operatorname{div}(\mathbf{A})}{\partial t} = -\operatorname{div}(\epsilon \nabla \varphi).$$

We now assume that $\frac{\partial \mathbf{A}}{\partial t} = 0$ (quasi-static approximation) and we obtain the Poisson equation

$$\operatorname{div}(-\epsilon \nabla \varphi) = \rho. \quad (2.25)$$

Finally, since we do not consider holes nor chemical species in the cell, we can write ρ as

$$\rho = -q n.$$

In metals the dielectric permittivity is infinite, thus it is not possible to use Eq. (2.25) to compute the electrostatic potential within them. Nevertheless we can use

equation (2.4), which is equivalent to requiring that the current density is a solenoidal vector. From the physical point of view this means that the flow of current density is constant, and therefore the electron current through any section of the conductor is always the same, regardless of the section considered. Using the relation (2.17) to express the electron current in metals, we obtain the following “general Poisson equation”:

$$\begin{cases} \operatorname{div}(-\epsilon_0 \epsilon_r^{AM} \nabla \varphi) = -q n & \text{in } \Omega_{AM} \\ \operatorname{div}(-\epsilon_0 \epsilon_r^d \nabla \varphi) = 0 & \text{in } \Omega_d \\ \operatorname{div}(-\sigma_n^{M1} \nabla \varphi) = \operatorname{div}(\sigma_n^{M1} \nabla (\alpha^{M1} T)) & \text{in } \Omega_{M1} \\ \operatorname{div}(-\sigma_n^{M2} \nabla \varphi) = \operatorname{div}(\sigma_n^{M2} \nabla (\alpha^{M2} T)) & \text{in } \Omega_{M2} \end{cases} \quad (2.26)$$

where we have rewritten the dielectric permittivity ϵ as the product of the absolute permittivity $\epsilon_0 \simeq 8.854 \cdot 10^{-14} \frac{F}{cm}$ (permittivity in vacuum) and the relative permittivity ϵ_r . We remind that Ω_d is the cell portion corresponding to the dielectric material where there are no free charge carriers ($n = 0$).

2.2.2 Electro-thermal transport

Using Eq. (2.3) and (2.12) with the constitutive relations (2.6), (2.11), (2.14) and (2.15), we obtain for the transport in a resistive memory cell the following set of equations:

$$\begin{cases} q \frac{\partial n}{\partial t} - \operatorname{div}(q D_n \nabla n - q \mu_n n \nabla \varphi + q \mu_n n \nabla (\alpha^{AM} T)) = 0 & \text{in } \Omega_{AM}, t > 0 \\ c^{AM} \varrho^{AM} \frac{\partial T}{\partial t} + \operatorname{div}(-k^{AM} \nabla T + \alpha^{AM} T \mathbf{j}_n^{drift,AM}) = -\operatorname{div}(\varphi \mathbf{j}_n^{drift,AM}) & \text{in } \Omega_{AM}, t > 0 \\ c^{M1} \varrho^{M1} \frac{\partial T}{\partial t} + \operatorname{div}(-k^{M1} \nabla T + \alpha^{M1} T \mathbf{j}_n^{M1}) = -\operatorname{div}(\varphi \mathbf{j}_n^{M1}) & \text{in } \Omega_{M1}, t > 0 \\ c^{M2} \varrho^{M2} \frac{\partial T}{\partial t} + \operatorname{div}(-k^{M2} \nabla T + \alpha^{M2} T \mathbf{j}_n^{M2}) = -\operatorname{div}(\varphi \mathbf{j}_n^{M2}) & \text{in } \Omega_{M2}, t > 0 \\ c^d \varrho^d \frac{\partial T}{\partial t} + \operatorname{div}(-k^d \nabla T) = 0 & \text{in } \Omega_d, t > 0 \end{cases} \quad (2.27)$$

where $\mathbf{j}_n^{drift,AM}$ is defined by (2.16), and $\mathbf{j}_n^{M1}, \mathbf{j}_n^{M2}$ are given by (2.17). The last equation in (2.27) is obtained from (2.12) by observing that in an ideal dielectric material no electric current flows ($\mathbf{j}_n^d = 0$).

As regards the model parameters, we use the superscripts $M1$, $M2$, d and AM in order to identify the material (metal 1, metal 2, dielectric and active material, respectively) in which the parameter is defined. We assume that the electrical conductivity in metals, and the relative permittivity in metals and in the dielectric material are constant quantities. The mass density, the specific heat, the thermal conductivity and

the thermopower are regarded as constants in each material, possibly depending on the spatial coordinates in the active material. We assume the same for μ_0 and v_{sat} .

Complete Model

The complete model is given by the general Poisson equation (2.26) and the transport model (2.27).

2.2.3 Initial conditions

The proposed model requires initial conditions for the electron concentration in the active material, and the temperature over the whole structure. We impose the following constant initial conditions:

$$n(\mathbf{x}, 0) = n_0 \quad \forall x \in \Omega_{AM}$$

$$T(\mathbf{x}, 0) = T_{room} \quad \forall x \in \Omega$$

where T_{room} is the room temperature (300 K).

2.2.4 Boundary conditions

Please refer to Fig. 2.1 for the definition of the domain interfaces.

General Poisson equation boundary conditions - interface conditions

The interfaces Γ_{C1} and Γ_{C2} represent the contacts to which the voltages are applied. We will always consider the potential at Γ_{C2} as a reference, equal to zero, applying the potential pulse to Γ_{C1} . On the remaining device boundary Γ_{ext} , we impose no flux conditions, meaning that the field lines will depart from a contact and close on the other. Then we have Dirichlet boundary conditions on Γ_{C1} and Γ_{C2} , and homogeneous Neumann boundary conditions on Γ_{ext} . The boundary conditions are thus given by:

$$\varphi = 0 \quad \text{on } \Gamma_{C2}$$

$$\varphi = \bar{\varphi} + \frac{1}{q} \Delta W_f \quad \text{on } \Gamma_{C1}$$

$$-\nabla \varphi \cdot \boldsymbol{\nu} = 0 \quad \text{on } \Gamma_{ext}$$

where $\boldsymbol{\nu}$ is the outward unit normal vector to Γ_{ext} , $\bar{\varphi}$ is a given potential pulse, and $\Delta W_f = W_f^{C1} - W_f^{C2}$ is the difference between the contacts work functions ([eV]). The applied potential $\bar{\varphi}$ at Γ_{C1} can be time-dependent. In this case we suppose the voltage pulse to be a polyline. Thus the pulse is characterized by a list of time instants and a corresponding list of potential values which represent the endpoints of each segment of the polyline. The value $\bar{\varphi}$ to apply at a given time t is computed by identifying to which line segment t belongs and then using the information about the segment endpoints.

As regards the interface conditions, we want to impose the continuity of the electrostatic potential across the interfaces Γ_{m1} , Γ_{m2} , $\Gamma_{diel-met}$, Γ_{diel} . Therefore we set

$$[\varphi]_{\Gamma_{m1}} = [\varphi]_{\Gamma_{m2}} = [\varphi]_{\Gamma_{diel-met}} = [\varphi]_{\Gamma_{diel}} = 0 \quad (2.28)$$

where $[v]_{\Gamma_\zeta}$ denotes the jump of the function v across the interface Γ_ζ .

Continuity equation boundary conditions

We will use different boundary conditions for the continuity equation, depending on the test case that we will be simulating. The boundary conditions are thus given by the following general formula

$$-\eta_\zeta^n \mathbf{j}_n^{AM} \cdot \boldsymbol{\nu} = \gamma_\zeta^n (\delta n - \bar{n}_\zeta) \quad \text{on } \Gamma_\zeta, t > 0 \quad (2.29)$$

where $\zeta \in \{m1, m2, diel\}$, $\boldsymbol{\nu}$ is the outward unit normal vector to Γ_ζ , \mathbf{j}_n^{AM} is given by

$$\mathbf{j}_n^{AM} = q D_n \nabla n - q \mu_n n \nabla \varphi + q \mu_n n \nabla (\alpha^{AM} T), \quad (2.30)$$

and

$$\eta_\zeta^n = \begin{cases} 1 & \text{Neumann or Robin conditions} \\ 0 & \text{Dirichlet conditions} \end{cases}$$

$$\gamma_\zeta^n = \begin{cases} \text{surface recombination rate} & \text{Robin conditions} \\ 1 & \text{Dirichlet or Neumann conditions} \end{cases}$$

$$\delta = \begin{cases} 0 & \text{Neumann} \\ 1 & \text{Robin or Dirichlet conditions} \end{cases}$$

$$\bar{n}_\zeta = \begin{cases} \text{surface electron flow} & \text{Neumann conditions} \\ \text{reference concentration value} & \text{Robin conditions} \\ \text{surface concentration value} & \text{Dirichlet conditions} \end{cases}.$$

The surface recombination velocity ($[cm/s]$) is the speed wherewith the electrons “vanish” at the interface. In general we will use thermal velocity as surface recombination rate. The thermal velocity v_{th} is defined as the root mean square of the total velocity of the carrier thermal motion, i.e., $v_{th} = \sqrt{\frac{3k_B T}{m}}$, m being the electron rest mass ([2]).

Heat equation boundary conditions - interface conditions

As in the case of the continuity equation, we will use different boundary conditions for the heat equation, depending on the test case that we will be simulating. The boundary conditions are thus given by the following general formula

$$-\eta_\zeta^T (k^\zeta \nabla T - \alpha^\zeta T \mathbf{j}_n^\zeta) \cdot \boldsymbol{\nu} = \gamma_\zeta^T (\delta T - \bar{T}_\zeta) \quad \text{on } \Gamma_\zeta, t > 0 \quad (2.31)$$

where $\zeta \in \{C1, C2, ext\}$, $\boldsymbol{\nu}$ is the outward unit normal vector to Γ_ζ , and

$$\eta_\zeta^T = \begin{cases} 1 & \text{Neumann or Robin conditions} \\ 0 & \text{Dirichlet conditions} \end{cases}$$

$$\gamma_\zeta^T = \begin{cases} \text{heat transfer coefficient} & \text{Robin conditions} \\ 1 & \text{Dirichlet or Neumann conditions} \end{cases}$$

$$\delta = \begin{cases} 0 & \text{Neumann} \\ 1 & \text{Robin conditions or Dirichlet conditions} \end{cases}$$

$$\bar{T}_\zeta = \begin{cases} \text{surface heat flow} & \text{Neumann conditions} \\ \text{external temperature value} & \text{Robin conditions} \\ \text{surface temperature value} & \text{Dirichlet conditions} \end{cases}$$

$$\theta^{ext} = \begin{cases} \theta^{M1} & \text{on } \Omega_{M1} \cap \Gamma_{ext} \\ \theta^d & \text{on } \Omega_d \cap \Gamma_{ext} \\ \theta^{M2} & \text{on } \Omega_{M2} \cap \Gamma_{ext} \end{cases} \quad \theta^{C1} = \theta^{M1}, \quad \theta^{C2} = \theta^{M2} \quad \text{with } \theta = k, \alpha, \mathbf{j}_n .$$

The heat transfer coefficient ($[W \text{ cm}^{-2} K^{-1}]$) is the rate of the heat exchange at the interface.

In order to ensure the continuity of the temperature across the interfaces Γ_{m1} , Γ_{m2} , $\Gamma_{diel-met}$, Γ_{diel} we impose the following interface conditions:

$$[T]_{\Gamma_{m1}} = [T]_{\Gamma_{m2}} = [T]_{\Gamma_{diel-met}} = [T]_{\Gamma_{diel}} = 0 . \quad (2.32)$$

2.3 Generalized Model Form

We will now write a general all-embracing equation which will summarize the model described above. This substitution will prove very helpful when we will have to write the weak formulation of the model and when we will study its well-posedness, in addition to simplifying the notation and reducing the number of equations we deal with. We define the following coefficients:

$$A = \begin{cases} 0 & \text{for } u = \varphi \\ q & \text{for } u = n \\ c\varrho & \text{for } u = T \end{cases} \quad (2.33)$$

$$\mathcal{D} = \begin{cases} \sigma_\varphi & \text{for } u = \varphi \\ qD_n & \text{for } u = n \\ k & \text{for } u = T \end{cases} \quad \sigma_\varphi = \begin{cases} \sigma^{M1} & \text{in } \Omega_{M1} \\ \epsilon_0 \epsilon_r^{AM} & \text{in } \Omega_{AM} \\ \sigma^{M2} & \text{in } \Omega_{M2} \\ \epsilon_0 \epsilon_r^d & \text{in } \Omega_d \end{cases} \quad (2.34)$$

$$\mathcal{R} = \begin{cases} 0 & \text{for } u = \varphi \\ q\mu_n & \text{for } u = n \\ \alpha\sigma_T & \text{for } u = T \end{cases} \quad \sigma_T = \begin{cases} \sigma^{M1} & \text{in } \Omega_{M1} \\ q n \mu_n & \text{in } \Omega_{AM} \\ \sigma^{M2} & \text{in } \Omega_{M2} \\ 0 & \text{in } \Omega_d \end{cases} \quad (2.35)$$

$$\Phi = \begin{cases} 0 & \text{for } u = \varphi \\ \varphi_{te} & \text{for } u = n \\ -\varphi & \text{for } u = T \end{cases} \quad \varphi_{te} = \varphi - \alpha T \quad (2.36)$$

$$\lambda = \begin{cases} \Sigma & \text{for } u = \varphi \\ 0 & \text{for } u = n \\ \varphi\sigma_T & \text{for } u = T \end{cases} \quad \Sigma = \begin{cases} \sigma^{M1}\alpha^{M1} & \text{in } \Omega_{M1} \\ 0 & \text{in } \Omega_d \cup \Omega_{AM} \\ \sigma^{M2}\alpha^{M2} & \text{in } \Omega_{M2} \end{cases} \quad (2.37)$$

$$\vartheta = \begin{cases} T & \text{for } u = \varphi \\ 0 & \text{for } u = n \\ \varphi & \text{for } u = T \end{cases} \quad (2.38)$$

$$g = \begin{cases} f_\varphi & \text{for } u = \varphi \\ 0 & \text{for } u = n \\ 0 & \text{for } u = T \end{cases} \quad f_\varphi = \begin{cases} 0 & \text{in } \Omega_{M1} \\ -q n & \text{in } \Omega_{AM} \\ 0 & \text{in } \Omega_{M2} \\ 0 & \text{in } \Omega_d \end{cases}. \quad (2.39)$$

Then the general equation can be written as

$$A \frac{\partial u}{\partial t} - \operatorname{div} \mathbf{F}_1(u) = g + \operatorname{div} \mathbf{F}_2 \quad \text{in } \omega, t > 0 \quad (2.40)$$

with:

$$\mathbf{F}_1(u) = \mathcal{D}\nabla u - \mathcal{R}u\nabla\Phi \quad (2.41)$$

$$\mathbf{F}_2 = \lambda\nabla\vartheta \quad (2.42)$$

$$\omega = \begin{cases} \Omega & \text{for } u = \varphi, T \\ \Omega_{AM} & \text{for } u = n \end{cases}.$$

Finally we define:

$$\begin{aligned}
 u_0 &= \begin{cases} n_0 & \text{for } u = n \\ T_{room} & \text{for } u = T \end{cases} \\
 \eta^\varphi &= \begin{cases} 1 & \text{on } \Gamma_{ext}, t > 0 \\ 0 & \text{on } \Gamma_{C1} \cup \Gamma_{C2}, t > 0 \end{cases} \\
 \eta^n &= \eta_\zeta^n \text{ with } \zeta \in \{m1, m2, diel\} \quad \eta^T = \eta_\zeta^T \text{ with } \zeta \in \{C1, C2, ext\} \\
 \gamma^\varphi &= \begin{cases} 0 & \text{on } \Gamma_{ext}, t > 0 \\ 1 & \text{on } \Gamma_{C1} \cup \Gamma_{C2}, t > 0 \end{cases} \\
 \gamma^n &= \gamma_\zeta^n \text{ with } \zeta \in \{m1, m2, diel\} \quad \gamma^T = \gamma_\zeta^T \text{ with } \zeta \in \{C1, C2, ext\} \\
 \bar{\varphi} &= \begin{cases} 0 & \text{on } \Gamma_{C2}, t > 0 \\ \bar{\varphi} + \frac{1}{q} \Delta W_f & \text{on } \Gamma_{C1}, t > 0 \end{cases} \\
 \bar{n} &= \bar{n}_\zeta \text{ with } \zeta \in \{m1, m2, diel\} \quad \bar{T} = \bar{T}_\zeta \text{ with } \zeta \in \{C1, C2, ext\} .
 \end{aligned} \tag{2.43}$$

We refer to the previous sub-section for the characterization of the parameters η_ζ^n , η_ζ^T , γ_ζ^n , γ_ζ^T , $\bar{\varphi}$, \bar{n}_ζ , \bar{T}_ζ and δ . We remind that all the parameters we introduced are constant or piecewise constant functions of the space coordinates, thus $\theta \in L^\infty(\Omega)$ with $0 < \theta^{MIN} \leq \theta(\mathbf{x}) \leq \theta^{MAX}$ a.e. in Ω (θ being a generic coefficient).

The generalized form of the problem is then given by

$$\begin{cases} A \frac{\partial u}{\partial t} - \operatorname{div} \mathbf{F}_1(u) - \operatorname{div} \mathbf{F}_2 = g & \text{in } \omega, t > 0 \\ u(\mathbf{x}, 0) = u_0(\mathbf{x}) & \text{in } \omega \\ -\eta^u \mathbf{F}_1(u) \cdot \boldsymbol{\nu} = \gamma^u (\delta u - \bar{u}) & \text{on } \partial\omega, t > 0 \end{cases} . \tag{2.44}$$

Chapter 3

Numerical Methods

3.1 Time Semi-Discretization

We consider the generalized problem (2.44), Eq. (2.40) is of parabolic type. Let us start with its semi-discretization in time. A widely used scheme for time integration of parabolic equations is the so-called θ -method ([49, 50]).

We define t^k as the k th time level, and we denote by v^k the value of the variable v at the k th time level (i.e. $v^k = v(\mathbf{x}, t^k)$). The time step is then given by $\Delta t^k = t^k - t^{k-1}$, and, in general, it will not be constant. We also define T_F as the final instant of the time range that we want to study, and $N \in \mathbb{N}$ such that $t^N = T_F$, i.e., $\sum_{k=1}^N \Delta t^k = T_F$. The θ -method discretizes the time derivative with a simple finite difference, and replaces the other terms with a linear combination, depending on the real parameter θ ($0 \leq \theta \leq 1$), of the value at time t^k and that at time t^{k+1} . Applying the θ -method to (2.40) we obtain

$$A \frac{u^{k+1} - u^k}{\Delta t^{k+1}} - \operatorname{div} [\theta \mathbf{F}_1^{k+1}(u^{k+1}) + (1 - \theta) \mathbf{F}_1^k(u^k)] = \theta (g^{k+1} + \operatorname{div} \mathbf{F}_2^{k+1}) + (1 - \theta) (g^k + \operatorname{div} \mathbf{F}_2^k) \quad \text{in } \omega. \quad (3.1)$$

We chose to adopt the Backward Euler method (or implicit Euler method) which corresponds to set $\theta = 1$. Then Eq. (3.1) becomes

$$\frac{A}{\Delta t^{k+1}} u^{k+1} - \operatorname{div} \mathbf{F}_1^{k+1}(u^{k+1}) = g^{k+1} + \operatorname{div} \mathbf{F}_2^{k+1} + \frac{A}{\Delta t^{k+1}} u^k \quad \text{in } \omega. \quad (3.2)$$

The implicit Euler method has order of convergence equal to one. This means that at

a specific time t^k the error is $\mathcal{O}(\Delta t^k)$. Moreover this method is A-stable and L-stable ([49, 50]).

Now we have to address the non linearity of Eq. (3.2) which is hidden inside the formula (2.41), and also the non linearity of the complete model. In order to overcome this obstacle we replace Eq. (3.2) with

$$\frac{A}{\Delta t^{k+1}} u^{k+1} - \operatorname{div} \mathbf{F}_1^{k_p}(u^{k+1}) = g^{k_p} + \operatorname{div} \mathbf{F}_2^{k_p} + \frac{A}{\Delta t^{k+1}} u^k \quad \text{in } \omega \quad (3.3)$$

where

$$\mathbf{F}_1^{k_p}(u^{k+1}) = \mathcal{D}^{k_p} \nabla u^{k+1} - \mathcal{R}^{k_p} u^{k+1} \nabla \Phi^{k_p}$$

and k_p is understood as the last time level at which the solutions are known. It can be seen in Eq. (3.3) that all the constant terms (g and \mathbf{F}_2) and the parameters of the flux term \mathbf{F}_1 are referred to the previous time step k_p . In this way each equation of the complete model is independent of the others and can be solved separately. Moreover each equation is linear.

3.2 Continuous Weak Formulation

Let us write the weak formulation of the following semi-discrete in time generalized problem at the generic time level $t^k \in (0, T_F)$:

for $k = 0, \dots, N - 1$ find $u^{k+1} \in H^1(\omega)$ s.t.

$$\begin{cases} \frac{A}{\Delta t^{k+1}} u^{k+1} - \operatorname{div} \mathbf{F}_1^{k_p}(u^{k+1}) = g^{k_p} + \operatorname{div} \mathbf{F}_2^{k_p} + \frac{A}{\Delta t^{k+1}} u^k & \text{in } \omega \\ -\eta^u \mathbf{F}_1^{k_p}(u^{k+1}) \cdot \boldsymbol{\nu} = \gamma^u(u^{k+1} - \bar{u}) & \text{on } \partial\omega \end{cases} . \quad (3.4)$$

We denote by $\partial\omega_D$, $\partial\omega_N$, $\partial\omega_R$ the portions of the domain boundary $\partial\omega$ where we impose Dirichlet, Neumann and Robin conditions, respectively. Let them be such that $\partial\omega = \partial\omega_D \cup \partial\omega_N \cup \partial\omega_R$ and $\partial\omega_D \cap \partial\omega_N = \partial\omega_N \cap \partial\omega_R = \partial\omega_D \cap \partial\omega_R = \emptyset$. Then we have:

$$\partial\omega_D = \Gamma_{C1} \cup \Gamma_{C2} \quad \partial\omega_N = \Gamma_{ext} \quad \partial\omega_R = \emptyset \quad \text{for } u = \varphi$$

while for $u = n, T$, $\partial\omega_D$, $\partial\omega_N$ and $\partial\omega_R$ are not fixed, and will be specified for each simulation test.

Let v_u be a test function belonging to the space $H_{0,\partial\omega_D}^1(\omega)$, corresponding to the

unknown quantity u . We consider the equation (3.3), we multiply it by the test function, and we integrate over the domain. Integrating by parts we obtain

$$\begin{aligned} \int_{\omega} \frac{A}{\Delta t^{k+1}} u^{k+1} v_u + \int_{\omega} \mathbf{F}_1^{k_p} (u^{k+1}) \cdot \nabla v_u - \int_{\partial\omega} \mathbf{F}_1^{k_p} (u^{k+1}) \cdot \boldsymbol{\nu} v_u \\ = \int_{\omega} g^{k_p} v_u + \int_{\omega} (\operatorname{div} \mathbf{F}_2^{k_p}) v_u + \int_{\omega} \frac{A}{\Delta t^{k+1}} u^k v_u \end{aligned}$$

and, using the boundary condition in (3.4) we get

$$\begin{aligned} \int_{\omega} \frac{A}{\Delta t^{k+1}} u^{k+1} v_u + \int_{\omega} \mathbf{F}_1^{k_p} (u^{k+1}) \cdot \nabla v_u + \int_{\partial\omega_R} \gamma^u u^{k+1} v_u \\ = \int_{\omega} g^{k_p} v_u + \int_{\omega} (\operatorname{div} \mathbf{F}_2^{k_p}) v_u + \int_{\partial\omega_R \cup \partial\omega_N} \gamma^u \bar{u} v_u + \int_{\omega} \frac{A}{\Delta t^{k+1}} u^k v_u . \end{aligned}$$

We define the following functional spaces

$$V_{\bar{u}} = \{v \in H^1(\omega) \text{ s.t. } v|_{\partial\omega_D} = \bar{u}\} \quad \text{and} \quad V_0^u = H_{0,\partial\omega_D}^1(\omega) .$$

Now we can derive the general weak formulation

for $k = 0, \dots, N-1$ find $u^{k+1} \in V_{\bar{u}}$ s.t.

$$\int_{\omega} \frac{A}{\Delta t^{k+1}} u^{k+1} v_u + a_u(u^{k+1}, v_u) = F_u(v_u) + \int_{\omega} \frac{A}{\Delta t^{k+1}} u^k v_u \quad \forall v_u \in V_0^u \quad (3.5)$$

where

$$a_u(u^{k+1}, v_u) = \int_{\omega} \mathbf{F}_1^{k_p} (u^{k+1}) \cdot \nabla v_u + \int_{\partial\omega_R} \gamma^u u^{k+1} v_u$$

$$F_u(v_u) = \int_{\omega} g^{k_p} v_u + \int_{\omega} (\operatorname{div} \mathbf{F}_2^{k_p}) v_u + \int_{\partial\omega_R \cup \partial\omega_N} \gamma^u \bar{u} v_u .$$

We will now describe the bilinear form a_u and the linear functional F_u for each equation of the complete model.

3.2.1 General Poisson equation weak form

In the case of the general Poisson equation, since the parameter A is null, the weak form is simply the following:

for $k = 0, \dots, N - 1$ finding $\varphi^{k+1} \in V_{\bar{\varphi}}$ s.t.

$$a_{\varphi}(\varphi^{k+1}, v_{\varphi}) = F_{\varphi}(v_{\varphi}) \quad \forall v_{\varphi} \in V_0^{\varphi}$$

where we recall that $\partial\Omega_D = \Gamma_{C1} \cup \Gamma_{C2}$, and $\bar{\varphi}$ is given by (2.43).

As regards the bilinear form, we have

$$a_{\varphi}(\varphi^{k+1}, v_{\varphi}) = \int_{\Omega} \sigma_{\varphi} \nabla \varphi^{k+1} \cdot \nabla v_{\varphi} \quad (3.6)$$

σ_{φ} being defined in (2.34). In order to obtain (3.6) we used the equality

$$-\int_{\partial\Omega} \sigma_{\varphi} \nabla \varphi^{k+1} \cdot \boldsymbol{\nu} v_{\varphi} = \int_{\partial\Omega} \gamma^{\varphi} (\varphi^{k+1} - \bar{\varphi}) v_{\varphi} = 0$$

since $v_{\varphi} = 0$ on $\partial\Omega_D$, and $-\nabla \varphi^{k+1} \cdot \boldsymbol{\nu} = 0$ (or $\gamma^{\varphi} = 0$) on Γ_{ext} .

As regards the linear functional, we have

$$F_{\varphi}(v_{\varphi}) = \int_{\Omega} f_{\varphi}^{k_p} v_{\varphi} + \int_{\Omega} \Sigma \Delta T^{k_p} v_{\varphi} \quad (3.7)$$

with f_{φ} , Σ given by (2.39) and (2.37), respectively. We used $\int_{\partial\Omega} \gamma^{\varphi} \bar{\varphi} v_{\varphi} = 0$ since $v_{\varphi} = 0$ on $\partial\Omega_D$, $\gamma^{\varphi} = 0$ on Γ_{ext} , and the equality

$$\int_{\Omega} v_{\varphi} \operatorname{div}(\Sigma \nabla T) = \int_{\Omega} v_{\varphi} \Sigma \operatorname{div}(\nabla T) = \int_{\Omega} \Sigma \Delta T^k v_{\varphi}.$$

3.2.2 Continuity equation weak form

The weak formulation of the continuity equation is

for $k = 0, \dots, N - 1$ find $n^{k+1} \in V_{\bar{n}}$ s.t.

$$\int_{\Omega_{AM}} \frac{A}{\Delta t^{k+1}} n^{k+1} v_n + a_n(n^{k+1}, v_n) = F_n(v_n) + \int_{\Omega_{AM}} \frac{A}{\Delta t^{k+1}} n^k v_n \quad \forall v_n \in V_0^n.$$

The bilinear form a_n is given by

$$\begin{aligned} a_n(n^{k+1}, v_n) &= \int_{\Omega_{AM}} q D_n^{k_p} \nabla n^{k+1} \cdot \nabla v_n - \int_{\Omega_{AM}} q \mu_n^{k_p} n^{k+1} \nabla \varphi_{te}^{k_p} \cdot \nabla v_n \\ &\quad + \int_{\tilde{\Gamma}_R} v_{rec}^n n^{k+1} v_n \end{aligned}$$

with φ_{te} being defined in (2.36), v_{rec}^n being the surface recombination rate for electrons, and $\tilde{\Gamma}_R$ representing the portion of $\partial\Omega_{AM}$ where Robin conditions are imposed.

Since we have no constant terms (both g and \mathbf{F}_2 are zero), the linear functional is

$$F_n(v_n) = \int_{\tilde{\Gamma}_R \cup \tilde{\Gamma}_N} \gamma^n \bar{n} v_n$$

with $\tilde{\Gamma}_N$ representing the portion of $\partial\Omega_{AM}$ where Neumann conditions are imposed. .

3.2.3 Heat equation weak form

For the temperature equation the weak form is given by

for $k = 0, \dots, N - 1$ find $T^{k+1} \in V_{\bar{T}}$ s.t.

$$\int_{\Omega} \frac{A}{\Delta t^{k+1}} T^{k+1} v_T + a_T(T^{k+1}, v_T) = F_T(v_T) + \int_{\Omega} \frac{A}{\Delta t^{k+1}} T^k v_T \quad \forall v_T \in V_0^T.$$

The bilinear form a_T is the following

$$\begin{aligned} a_T(T^{k+1}, v_T) &= \int_{\Omega} k \nabla T^{k+1} \cdot \nabla v_T - \int_{\Omega} \alpha \sigma_T^{k_p} T^{k+1} \nabla(-\varphi) \cdot \nabla v_T \\ &\quad + \int_{\partial\Omega_R} \gamma^T T^{k+1} v_T \end{aligned}$$

with σ_T defined in (2.35), and $\partial\Omega_R$ being the portion of $\partial\Omega$ where Robin conditions are imposed.

Now, to compute the linear functional F_T , we recall that, in this case, $\mathbf{F}_2^{k_p} = \varphi^{k+1} \sigma_T^{k_p} \nabla \varphi^{k+1}$. Thus we can write

$$\begin{aligned} \operatorname{div}(\mathbf{F}_2^{k_p}) &= \sigma_T^{k_p} \nabla \varphi^{k+1} \cdot \nabla \varphi^{k+1} + \varphi^{k+1} \operatorname{div}(\sigma_T^{k_p} \nabla \varphi^{k+1}) \\ &= \sigma_T^{k_p} \nabla \varphi^{k+1} \cdot \nabla \varphi^{k+1} + \varphi^{k+1} \sigma_T^{k_p} \Delta \varphi^{k+1} \\ &\quad + \varphi^{k+1} \nabla \varphi^{k+1} \cdot \nabla (\sigma_T^{k_p}). \end{aligned}$$

Since the constant term g is null, then the linear functional is given by

$$\begin{aligned} F_T(v_T) = & \int_{\Omega} \sigma_T^{k_p} \nabla \varphi^{k+1} \cdot \nabla \varphi^{k+1} v_T + \int_{\Omega} \varphi^{k+1} \sigma_T^{k_p} \Delta \varphi^{k+1} v_T + \\ & \int_{\Omega} \varphi^{k+1} \nabla \varphi^{k+1} \cdot \nabla (\sigma_T^{k_p}) v_T + \int_{\partial\Omega_R \cup \partial\Omega_N} \gamma^T \bar{T} v_T \end{aligned}$$

with $\partial\Omega_N$ being the portion of $\partial\Omega$ where Neumann conditions are imposed.

3.3 Well-Posedness Analysis

In order to prove the existence and uniqueness of the solutions of the variational problems introduced in the previous section, we apply the Lax-Milgram theorem (see [51]) to the weak formulation (3.5).

We write the functional space $V_{\bar{u}}$ as the affine variety $V_{\bar{u}} = \bar{u} + V_0^u$. We have that V_0^u is an Hilbert space. To simplify notation, during this analysis we will denote by u and by Δt the unknown variable u and the time step at time level t^{k+1} , respectively. Moreover we will use the symbol $\hat{\cdot}$ to identify known variables and quantities at time level t^{k_p} . Then we can recast Eq. (3.5) as

$$\text{find } u \in V_0^u \text{ s.t. } B(u, v) = F(v) \quad \forall v \in V_0^u \quad (3.8)$$

with:

$$B(u, v) = \int_{\omega} \frac{A}{\Delta t} u v + a_u(u, v) \quad \text{and} \quad F(v) = F_u(v) + \int_{\omega} \frac{A}{\Delta t} \hat{u} v .$$

We recall that for each parameter θ of the model equations we assume $0 < \theta^{MIN} \leq \theta(\mathbf{x}) \leq \theta^{MAX}$ a.e. in Ω . Finally we assume that the boundary data $\bar{\varphi}$, \bar{n} and \bar{T} are sufficiently smooth functions so that the Sobolev trace inequality can be applied (see [51]).

3.3.1 General Poisson equation well-posedness

First we prove the existence and uniqueness for the solution of the general Poisson equation:

continuity of the bilinear form:

$$| \int_{\Omega} \sigma_{\varphi} \nabla \varphi \cdot \nabla v | \leq \sigma_{\varphi}^{MAX} \| \nabla \varphi \|_{L^2} \| \nabla v \|_{L^2} \leq \sigma_{\varphi}^{MAX} \| \varphi \|_{V_0^{\varphi}} \| v \|_{V_0^{\varphi}}$$

where we used the Cauchy-Schwarz inequality (see [51]).

coercivity of the bilinear form:

$$\int_{\Omega} \sigma_{\varphi} \nabla \varphi \cdot \nabla \varphi \geq \sigma_{\varphi}^{MIN} \| \nabla \varphi \|_{L^2}^2 \geq \frac{\sigma_{\varphi}^{MIN}}{c_P^{\Omega} + 1} \| \varphi \|_{V_0^{\varphi}}^2$$

where we used the Poincaré inequality (see [51], c_P^{Ω} is the Poincaré constant for the domain Ω).

continuity of the functional:

$$\begin{aligned} \left| \int_{\Omega} \widehat{f}_{\varphi} v + \int_{\Omega} v \operatorname{div} (\Sigma \nabla \widehat{T}) \right| &\leq \left| \int_{\Omega_{AM}} -q \widehat{n} v \right| + \left| \int_{\Omega} v \operatorname{div} (\Sigma \nabla \widehat{T}) \right| \\ &\leq q \| \widehat{n} \|_{L^2} \| v \|_{L^2} + \left| - \int_{\Omega} \nabla v \cdot \Sigma \nabla \widehat{T} \right| \\ &\quad + \left| \int_{\partial\Omega} v \cdot \Sigma \nabla \widehat{T} \cdot \boldsymbol{\nu} \right| \\ &\leq q \| \widehat{n} \|_{L^2} \| v \|_{V_0^{\varphi}} + \Sigma^{MAX} \| \nabla \widehat{T} \|_{L^2} \| v \|_{V_0^{\varphi}} \\ &\quad + \left| \int_{\partial\Omega} v \cdot \Sigma \nabla \widehat{T} \cdot \boldsymbol{\nu} \right| \end{aligned}$$

where we integrated by parts the second term of the functional, and we used the Cauchy-Schwarz inequality. Since $v \in V_0^{\varphi}$, $\left| \int_{\partial\Omega} v \cdot \Sigma \nabla \widehat{T} \cdot \boldsymbol{\nu} \right| = \left| \int_{\Gamma_{ext}} v \cdot \Sigma \nabla \widehat{T} \cdot \boldsymbol{\nu} \right|$. If we impose Dirichlet condition for the temperature on Γ_{ext} , then this integral vanish ($\nabla \overline{T} = 0$). If we impose Neumann or Robin condition, using trace inequality we obtain

$$\begin{aligned} \left| \int_{\Gamma_{ext}} v \cdot \Sigma \nabla \widehat{T} \cdot \boldsymbol{\nu} \right| &= \left| \int_{\Gamma_{ext}} v \cdot \Sigma \left(-\frac{\gamma^T}{k} \right) (\delta \widehat{T} - \overline{T}) \right| \\ &\leq \Sigma^{MAX} \frac{|\gamma^T|}{k^{MAX}} \left(c_T \delta \| \widehat{T} \|_{V_0^T} + |\Gamma_{ext}| |\overline{T}| \right) c_T \| v \|_{V_0^{\varphi}} \end{aligned}$$

with c_T being a constant depending on the domain Ω , and $|\Gamma_{ext}|$ being the measure of the surface Γ_{ext} .

Then we can state that there exists a unique solution of the general Poisson equation. Furthermore, the Lax-Milgram theorem gives an a priori estimate of the solution:

$$\| \varphi \|_{V_0^\varphi} \leq \frac{M}{\Lambda}$$

with

$$M = q \| \widehat{n} \|_{L^2} + \Sigma^{MAX} \| \nabla \widehat{T} \|_{L^2} \Sigma^{MAX} \frac{|\gamma^T|}{k^{MAX}} \left(c_T \delta \| \widehat{T} \|_{V_0^T} + |\Gamma_{ext}| \| \overline{T} | \right)$$

$$\Lambda = \frac{\sigma_\varphi^{MIN}}{c_P^\Omega + 1}.$$

3.3.2 Continuity and temperature equation well-posedness

Since the flux function $\mathbf{F}_1(u)$ in the continuity equation and in the temperature equation has the same form, we consider the generalized expression (2.41) to prove the continuity and the coercivity of the bilinear forms of both these equations. We assume that the potential is limited, i.e., $\widehat{\varphi} \in L^\infty(\Omega)$. Moreover, we assume $\widehat{\mathcal{D}}$, $\widehat{\mathcal{R}}$ and $\widehat{\Phi}$ are piecewise smooth functions on $\overline{\Omega}$, following [45]. This hypothesis is quite reasonable since, using the finite element method, these quantities will be polynomials on each element of the grid.

We define the quantity ψ such that

$$\nabla \psi = \frac{\mathcal{R}}{\mathcal{D}} \nabla \Phi.$$

We also assume that $0 < \psi^{MIN} \leq \psi(\mathbf{x}) \leq \psi^{MAX}$ a.e. in Ω . Finally we define $\tilde{u} = u \exp(-\psi)$, and we rewrite (3.8) as

$$\text{find } \tilde{u} \in V_0^u \text{ s.t. } B(\tilde{u}, v) = F(v) \quad \forall v \in V_0^u$$

with

$$B(\tilde{u}, v) = \int_{\omega} \frac{A}{\Delta t} \exp(\psi) \tilde{u} v + \int_{\omega} \widehat{\mathcal{D}} \exp \psi \nabla \tilde{u} \cdot \nabla v + \int_{\partial \omega_R} \gamma^u \exp(\psi) \tilde{u} v.$$

We will prove the existence and uniqueness of the unknown variable \tilde{u} . Thanks to the univocal relation between u and \tilde{u} , this ensures the existence and uniqueness of the solution u .

continuity of the bilinear form:

$$\begin{aligned} \left| \int_{\omega} \frac{A}{\Delta t} \exp(\psi) \tilde{u} v + \int_{\omega} \widehat{\mathcal{D}} \exp \psi \nabla \tilde{u} \cdot \nabla v + \int_{\partial \omega_R} \gamma^u \exp(\psi) \tilde{u} v \right| &\leq \exp(\psi^{MAX}) \left\{ \frac{A^{MAX}}{\Delta t} \| \tilde{u} \|_{V_0^u} \| v \|_{V_0^u} \right. \\ &\quad + \widehat{\mathcal{D}}^{MAX} \| \tilde{u} \|_{V_0^u} \| v \|_{V_0^u} \\ &\quad \left. + \gamma^{u,MAX} c_T^2 \| \tilde{u} \|_{V_0^u} \| v \|_{V_0^u} \right\} \end{aligned}$$

where we used the Cauchy-Schwarz inequality and the trace inequality (c_T is a constant depending on the domain).

coercivity of the bilinear form:

$$\begin{aligned} \int_{\omega} \frac{A}{\Delta t} \exp(\psi) \tilde{u}^2 + \int_{\omega} \widehat{\mathcal{D}} \exp \psi \nabla \tilde{u} \cdot \nabla \tilde{u} + \int_{\partial \omega_R} \gamma^u \exp(\psi) \tilde{u}^2 &\geq \exp(\psi^{MIN}) \left\{ \frac{A^{MIN}}{\Delta t} \| u \|_{L^2}^2 \right. \\ &\quad \left. + \widehat{\mathcal{D}}^{MIN} \| \nabla \tilde{u} \|_{L^2}^2 \right\} \\ &\geq \Lambda \| \tilde{u} \|_{V_0^u}^2 \end{aligned}$$

where we used the fact that $\int_{\partial \omega_R} \gamma^u \exp(\psi) \tilde{u}^2 \geq 0$, and we have

$$\Lambda = \exp(\psi^{MIN}) \min \left(\frac{A^{MIN}}{\Delta t}, \widehat{\mathcal{D}}^{MIN} \right).$$

continuity of the functional: in the case of the continuity equation we have

$$\begin{aligned} \left| \int_{\Omega_{AM}} \frac{q}{\Delta t} \hat{n} v + \int_{\tilde{\Gamma}_R \cup \tilde{\Gamma}_N} \gamma^n \bar{n} v \right| &\leq \frac{q}{\Delta t} \| \hat{n} \|_{L^2} \| v \|_{V_0^\varphi} \\ &\quad + \gamma^{n,MAX} c_T^2 \| \bar{n} \|_{V_0^u} \| v \|_{V_0^u} \end{aligned}$$

where we used the Cauchy-Schwarz inequality and the trace inequality (c_T is a constant depending on the domain).

In the case of the temperature equation we have

$$\begin{aligned} \left| \int_{\Omega} \frac{c\rho}{\Delta t} \hat{T} v + \int_{\partial \Omega_R \cup \partial \Omega_N} \gamma^T \bar{T} v + \int_{\Omega} \operatorname{div}(\hat{\varphi} \widehat{\sigma_T} \nabla \hat{\varphi}) v \right| &\leq \\ \frac{c\rho}{\Delta t} \| \hat{T} \|_{L^2} \| v \|_{V_0^\varphi} + \gamma^{T,MAX} c_T^2 \| \bar{T} \|_{V_0^u} \| v \|_{V_0^u} & \\ + \left| \int_{\Omega} \hat{\varphi} \widehat{\sigma_T} \nabla \hat{\varphi} \cdot \nabla v \right| + \left| \int_{\partial \Omega} v \hat{\varphi} \widehat{\sigma_T} \nabla \hat{\varphi} \cdot \boldsymbol{\nu} \right| & \end{aligned}$$

$$\begin{aligned}
& + \frac{c\rho}{\Delta t} \| \widehat{T} \|_{L^2} \| v \|_{V_0^\varphi} + \gamma^{T,MAX} c_T^2 \| \bar{T} \|_{V_0^u} \| v \|_{V_0^u} \\
& + \sigma_T^{MAX} \| \widehat{\varphi} \|_{L^\infty} \| \nabla \widehat{\varphi} \|_{L^2} \| v \|_{V_0^u} \\
& + \left| \int_{\partial\Omega} v \widehat{\varphi} \widehat{\sigma}_T \nabla \widehat{\varphi} \cdot \boldsymbol{\nu} \right|
\end{aligned}$$

where we used the Cauchy-Schwarz inequality. For the integral on the boundary $\partial\Omega$ we obtain, using the trace inequality (c_T is a constant depending on the domain)

$$\begin{aligned}
\left| \int_{\partial\Omega} v \widehat{\varphi} \widehat{\sigma}_T \nabla \widehat{\varphi} \cdot \boldsymbol{\nu} \right| &= \left| \int_{\Gamma_{C1} \cup \Gamma_{C2}} v \widehat{\varphi} \widehat{\sigma}_T \nabla \widehat{\varphi} \cdot \boldsymbol{\nu} \right| \\
&\leq \sigma_T^{MAX} \| \bar{\varphi} \| \| \nabla \widehat{\varphi} \cdot \boldsymbol{\nu} \|_{L^2_{\Gamma_{C1} \cup \Gamma_{C2}}} c_T \| v \|_{V_0^\varphi}
\end{aligned}$$

since $\nabla \widehat{\varphi} \cdot \boldsymbol{\nu} = 0$ on Γ_{ext} , $\widehat{\varphi} = \bar{\varphi} = \text{constant}$ on $\Gamma_{C1} \cup \Gamma_{C2}$, and also $\sigma_T = \text{constant}$ on $\Gamma_{C1} \cup \Gamma_{C2}$.

Then we can state that both the continuity and the temperature equation admit exactly one solution. Also in this case, an a priori estimate for the variable \tilde{u} can be written, but the theorem does not provide any estimate for the solution u .

3.4 Finite Element Discretization and Matrix Form

3.4.1 Galerkin approximation

In view of the finite element discretization of problem (3.4) let \mathcal{T}_h be a regular partition ([52]) of the domain ω into tetrahedral elements K of volume $|K|$. This is equivalent to assume that there exists a constant $\xi \geq 1$ such that $\frac{h_K}{\rho_K} \leq \xi \forall K \in \mathcal{T}_h$, h_k being the diameter of K and ρ_K being the diameter of the inscribed sphere to K . We denote by \mathcal{V}_h the set of all the vertices of \mathcal{T}_h , and by \mathcal{F}_h and \mathcal{E}_h the set of all the faces and the edges of \mathcal{T}_h , respectively. Finally, for each $K \in \mathcal{T}_h$ we denote by ∂K , $\boldsymbol{\nu}_{\partial K}$ and $\mathbf{t}_{\partial K}$ the boundary of the element and its outward unit normal and tangent vectors (according to a counterclockwise orientation along ∂K), respectively.

Let $V_{0,h}^u$ be a finite-dimensional subspaces of V_0^u such that

$$V_{0,h}^u = \{v_h \in C^0(\bar{\omega}) \text{ s.t. } v_h|_K \in \mathbb{P}^1(K) \forall K \in \mathcal{T}_h \wedge v_h|_{\partial\omega_D} = 0\}.$$

V_0^u is a proper Hilbert subspace of $V_{\bar{u}}$. We consider the affine variety $V_{\bar{u},h} = \bar{u}_h + V_{0,h}^u \not\subseteq V_{\bar{u}}$, where \bar{u}_h is a suitable approximation of \bar{u} , obtained, e.g., by interpolation or projection, then we have

$$V_{\bar{u},h} = \{v_h \in C^0(\bar{\omega}) \text{ s.t. } v_h|_K \in \mathbb{P}^1(K) \forall K \in \mathcal{T}_h \wedge v_h|_{\partial\omega_D} = \bar{u}_h\}.$$

The Galerkin approximation of problem (3.5) is then

for $k = 0, \dots, N - 1$ find $u_h^{k+1} \in V_{\bar{u},h}$ s.t.

$$\int_{\omega} \frac{A}{\Delta t^{k+1}} u_h^{k+1} v_u + a_u(u_h^{k+1}, v_{u,h}) = F_u(v_{u,h}) + \int_{\omega} \frac{A}{\Delta t^{k+1}} u_h^k v_{u,h} \quad \forall v_{u,h} \in V_{0,h}^u. \quad (3.9)$$

We remark that, looking for the approximated solution in the space $V_{\bar{u},h}$, we have that the interface conditions (2.28), (2.32) are automatically verified.

3.4.2 Matrix form

We denote by $\{\psi_j^u\}_{j=1}^{N_h}$ the Lagrangian basis of the space $V_{0,h}^u$, N_h being the finite dimension of the space. Then it is sufficient that (3.9) is verified for each basis function, because all functions belonging to $V_{0,h}^u$ are linear combinations of the functions ψ_j^u . Since $u_h^{k+1} \in V_{\bar{u},h}$, we can write $u_h^{k+1} = \bar{u}_h + \tilde{u}_h^{k+1}$ with $\tilde{u}_h^{k+1} \in V_{0,h}^u$. Being \bar{u}_h known, the actual unknown is \tilde{u}_h^{k+1} which can be expressed as

$$\tilde{u}_h^{k+1} = \sum_{j=1}^{N_h} u_j^{k+1} \psi_j^u$$

where u_j^{k+1} , $j = 1, \dots, N_h$ are unknown coefficients. Then the Galerkin problem (3.9) becomes:

for $k = 0, \dots, N - 1$ find u_j^{k+1} , $j = 1, \dots, N_h$ s.t.

$$\frac{1}{\Delta t^{k+1}} \mathcal{M} \mathbf{u}^{k+1} + \mathcal{A}^u \mathbf{u}^{k+1} = \mathbf{f}^u + \frac{1}{\Delta t^{k+1}} \mathcal{M} \mathbf{u}^k \quad (3.10)$$

where

$$\mathcal{M}_{ij} = \int_{\omega} \psi_i \psi_j \quad \mathcal{A}_{ij}^u = a_u(\psi_j, \psi_i) \quad \mathbf{f}_i^u = F_u(\psi_i).$$

\mathcal{M} is the mass matrix, while \mathcal{A}^u is the stiffness matrix and \mathbf{f}^u is the load vector. In order to construct the mass and stiffness matrices and the load vector, we first compute their local counterpart \mathcal{M}_K , \mathcal{A}_K^u , \mathbf{f}_K^u where all the integrals are defined on the single tetrahedron K , or its border ∂K , i.e.,

$$(\mathcal{M}_K)_{ij} = \int_K \psi_i \psi_j \quad (\mathcal{A}_K^u)_{ij} = a_u^K (\psi_j, \psi_i) \quad (\mathbf{f}_K^u)_i = F_u^K (\psi_i)$$

with

$$a_u^K (\psi_j, \psi_i) = \int_K \left(\mathbf{F}_1^{k_p} (\psi_j) \right)_h \cdot \nabla \psi_i + \int_{\partial K \cap \partial \omega_R} \gamma^u \psi_j \psi_i \quad (3.11)$$

$$F_u^K (\psi_i) = \int_K g_h^{k_p} \psi_i + \int_K \operatorname{div} \left(\mathbf{F}_2^{k_p} \right)_h \psi_i + \int_{\partial K \cap \{\partial \omega_R \cup \partial \omega_N\}} \gamma^u \bar{u}_h \psi_i. \quad (3.12)$$

Once we compute the local contributions for each element K , we can assemble the global matrices and load vector as follows: let I (J) be the global index of a generic vertex belonging to the partition \mathcal{T}_h , we denote by $\mathcal{T}_K : \mathcal{V}_{\mathcal{T}_h} \rightarrow \mathcal{V}_K$ the map which connects I (J) to its corresponding local index i (j), with $i = 1, \dots, 4$, in the element K . Then we have

$$M_{IJ} = \sum_{\forall K \in \mathcal{T}_h \text{ s.t. } \mathcal{T}_K(I), \mathcal{T}_K(J) \subset \mathcal{V}_K} (M_K)_{ij} \quad \text{with } M = \mathcal{M}, \mathcal{A}^u$$

and

$$(\mathbf{f}^u)_I = \sum_{\forall K \in \mathcal{T}_h \text{ s.t. } \mathcal{T}_K(I) \subset \mathcal{V}_K} (\mathbf{f}_K^u)_i.$$

3.4.2.1 The stiffness matrix

As regards the general Poisson equation, we have

$$a_\varphi^K (\psi_j, \psi_i) = \int_K \sigma_\varphi^K \nabla \psi_j \cdot \nabla \psi_i$$

Since σ_φ^K is a constant we have that the local stiffness matrix \mathcal{A}_K^φ is given by

$$\mathcal{A}_K^\varphi = \sigma_\varphi^K L^K$$

where L^K is the Laplacian matrix over K .

As regards the continuity equation and the temperature equation the construction of the stiffness matrix is a delicate issue. In fact those are parabolic conservation laws with possibly dominating advective and/or reactive terms. We will use a unified framework developed in [35] for finite element formulations that are characterized by:

- conservation properties for the flux vector variable,
- a discrete maximum principle for the scalar variable.

In particular we choose a nodal-based method which provides flux conservation across the Voronoi cell associated with each node of the domain triangulation: the Finite Volume Scharfetter-Gummel (FVSG) method.

The maximum principle on the continuous level states that ([35, 45])

$$\frac{A}{\Delta t^{k+1}} u^{k+1}(\mathbf{x}) - \operatorname{div} \mathbf{F}_1^{k+1}(u^{sk+1}(\mathbf{x})) \geq 0 \quad \forall \mathbf{x} \in \bar{\omega} \Rightarrow u^{k+1}(\mathbf{x}) \geq 0 \quad \forall \mathbf{x} \in \bar{\omega} \quad \forall k \geq 0$$

while the global flux conservation asserts that ([35])

$$\mathbf{F}_1^{k+1}(u^{k+1}(\mathbf{x}))|_K \cdot \boldsymbol{\nu}_{\partial K} - \mathbf{F}_1^{k+1}(u^{k+1}(\mathbf{x}))|_{K'} \cdot \boldsymbol{\nu}_{\partial K'} = 0 \quad \forall F_{K-K'} \in \mathcal{F}_h$$

with $F_{K-K'}$ being the face shared by the elements K and K' . The discretization method then must ensure the following properties:

- discrete maximum principle

$$g_h^{kp} + \operatorname{div} (\mathbf{F}_2^{kp})_h + \frac{A}{\Delta t^{k+1}} u_h^k \geq 0 \Rightarrow u_h^{k+1} \geq 0 \quad \forall k \geq 0$$

where g_h^{kp} and $(\mathbf{F}_2^{kp})_h$ are a suitable approximation of g^{kp} and \mathbf{F}_2^{kp} in $V_h = \{v_h \in C^0(\bar{\omega}) \text{ s.t. } v_h|_K \in \mathbb{P}^1(K)\}$, respectively;

- local flux conservation for $(\mathbf{F}_1^{kp}(u_h^{k+1}(\mathbf{x})))_h$, which means that, whenever source/sink and reaction term are absent ($g = \mathbf{F}_2 = 0$), we have $\forall k \geq 0$

$$-\int_{B_v} \operatorname{div} (\mathbf{F}_1^{kp}(u_h^{k+1}(\mathbf{x})))_h = -\int_{\partial B_v} (\mathbf{F}_1^{kp}(u_h^{k+1}(\mathbf{x})))_h \cdot \boldsymbol{\nu}_{\partial B_v} \quad \forall v \in \mathcal{V}_h$$

B_v being the Voronoi cell associated with the generic node v (see Appendix A in [44] for a detailed description of Voronoi cells in the case of tetrahedral elements).

In order to apply the FVSG method it is necessary to reformulate the flux function $\mathbf{F}_1(u)$ as

$$\forall K \in \mathcal{T}_h \quad \mathbf{F}_1(u)|_K = \mathcal{D}^K \nabla u - \mathcal{R}^K u \nabla \Phi = \mathcal{D}^K \exp(\Psi) \nabla [\exp(-\Psi) u]$$

with

$$\Psi = \frac{\Phi}{\Phi_{ref}} \quad \text{with} \quad \Phi_{ref} = \frac{\mathcal{D}^K}{\mathcal{R}^K}$$

where $\mathcal{D}^K, \mathcal{R}^K$ are the average values on the element K of the parameter \mathcal{D}, \mathcal{R} , respectively, and:

$$\Phi = \begin{cases} \varphi_{te} & \text{for } u = n \\ -\varphi & \text{for } u = T \end{cases} \quad \Phi_{ref} = \begin{cases} \frac{k_B T}{q} & \text{for } u = n \\ \frac{k}{\alpha q n \mu_n} & \text{for } u = T \end{cases}.$$

Now we consider the first term of the local bilinear form a_u^K in (3.11). It can be proved that (see [43])

$$\int_K \left(\mathbf{F}_1^{k_p}(\psi_j) \right)_h \cdot \nabla \psi_i = - \int_{\partial B_i} \left(\mathbf{F}_1^{k_p}(\psi_j) \right)_h \cdot \boldsymbol{\nu}_{\partial B_i} \quad (3.13)$$

where $B_i = B_v \cap K$, v being the i -th node of the tetrahedron K . We can thus express the integral over ∂B_i as

$$- \int_{\partial B_i} \left(\mathbf{F}_1^{k_p}(\psi_j) \right)_h \cdot \boldsymbol{\nu}_{\partial B_i} = - \sum_{F \in \mathcal{F}_{B_i}} \int_F \left(\mathbf{F}_1^{k_p}(\psi_j) \right)_h \cdot \boldsymbol{\nu}_F$$

$\boldsymbol{\nu}_F$ being the unit outward normal to the face F . The volume B_i is composed of three square-based pyramids, and it is bounded by three normal planes bisecting the edges connecting vertex i to the other vertices of the element, plus the three tetrahedron faces sharing vertex i (Appendix A in [44]). The contributions of the integrals over the element faces are canceled by the integrals over the same faces in the adjacent tetrahedra. This is due to the fact that the outward unit normal vectors to the faces of neighboring elements have opposite directions. Thus we consider only the contributions of the integrals over the planes bisecting the edges. As we said above, the planes are perpendicular to the edges connecting vertex i to the other vertices of the element, therefore the normal vectors to these planes will be parallel to such edges. Hence the

scalar product becomes

$$\left(\mathbf{F}_1^{k_p}(\psi_j) \right)_h \cdot \boldsymbol{\nu}_{P_{il}} = \left(\mathbf{F}_1^{k_p}(\psi_j) \right)_h \cdot (\pm \mathbf{t}_{il}) \quad \forall l \neq i \wedge l \in \mathcal{E}_K$$

where P_{il} and \mathbf{t}_{il} are the normal plane and the unit tangent vector to the edge \mathbf{e}_{il} connecting vertex l to i , respectively. For each edge $\mathbf{e}_{il} \in \mathcal{E}_K$ the tangential component of $\mathbf{F}_1^{k_p}(\psi_j)$ along the edge in the FVSG method is defined as

$$\left(\mathbf{F}_1^{k_p}(\psi_j) \right)_{h, \mathbf{e}_{il}} = \mathcal{D}^K \frac{\mathcal{B}\left(\Delta_{il}\Psi_h^{k_p}\right)\psi_j(\mathbf{x}_i) - \mathcal{B}\left(-\Delta_{il}\Psi_h^{k_p}\right)\psi_j(\mathbf{x}_l)}{|\mathbf{e}_{il}|} \quad (3.14)$$

where $\Delta_{il}\Psi_h^{k_p} = \Psi_h^{k_p}(\mathbf{x}_i) - \Psi_h^{k_p}(\mathbf{x}_l)$ and \mathcal{B} is the inverse of the Bernoulli function defined as:

$$\mathcal{B}(z) = \begin{cases} \frac{z}{\exp(z)-1} & \text{if } z \neq 0 \\ 1 & \text{if } z = 0 \end{cases}.$$

Using the equality (3.13) and the formula (3.14), we can build the local stiffness matrix $\mathcal{A}_{K,FVSG}^u$. $\mathcal{A}_{K,FVSG}^u$ has the following relevant properties (see [47] for the proof):

- $\sum_{j=1}^4 (\mathcal{A}_{K,FVSG}^u)_{ij} = - \int_K \mathcal{D}^K \nabla \Psi^{k_p} \cdot \nabla \psi_i \quad \text{with } i = 1, \dots, 4.$

This property states that in the case $u_h|_K = \text{constant}$, then the element flux $\left(\mathbf{F}_1^{k_p}(u_h^{k+1}(\mathbf{x})) \right)_h$ is purely advective.

- $\sum_{i=1}^4 (\mathcal{A}_{K,FVSG}^u)_{ij} = 0 \quad \text{with } i = 1, \dots, 4.$

This property states that $\int_K \left(\mathbf{F}_1^{k_p}(u_h^{k+1}(\mathbf{x})) \right)_h \cdot \nabla c = 0$ for a constant c .

- $(\mathcal{A}_{K,FVSG}^u)_{ij} \leq 0, (\mathcal{A}_{K,FVSG}^u)_{ii} > 0$ with $i \neq j$ and $i = 1, \dots, 4$.

The above properties allow to show that, when $\partial\omega_D$ has a non-vanishing measure, the global matrix \mathcal{A}^u of the FVSG method is an irreducible, diagonally dominant M-matrix with respect to its columns ([48]). This implies that the FVSG discretization scheme ensures the discrete maximum principle.

We still have to add the components of the local matrix due to the contributions of the boundary integrals in (3.11). We recall the generic boundary contribution to the bilinear form which is

$$\int_{\partial K \cap \partial\omega_R} \gamma^u \psi_j \psi_j \quad \text{for } i, j = 1, \dots, 4.$$

To compute this integral we use an approximating technique: the trapezoidal rule. The approximated integral over a generic element K of a generic function $f : \mathbb{R}^d \rightarrow \mathbb{R}$ (with $d \geq 1$) is

$$\int_K f d\mathbf{x} \approx \frac{|K|}{d+1} \sum_{i=1}^{d+1} f(\mathbf{x}_i)$$

where \mathbf{x}_i with $i = 1, \dots, d+1$ are the vectors of the spatial coordinates of the vertices belonging to K . Obviously, this approximation introduces an error which, however, is of order one with respect to the grid step. Since we are using a \mathbb{P}^1 finite element discretization which has an order of accuracy equal to one, the trapezoidal rule is very suitable and does not imply a larger error. Applying this approximation rule, we obtain an additional matrix $(\mathcal{A}_K^u)^{bound}$ which, added to $\mathcal{A}_{K,FVSG}^u$, provides the full local stiffness matrix \mathcal{A}_K^u .

The trapezoidal rule is also used to compute the local mass matrix.

3.4.2.2 The load vector

In order to compute the volume integrals in the load vector, again we use the trapezoidal rule.

In the case of the general Poisson equation the local load vector is

$$(\mathbf{f}_K^\varphi)_i = F_\varphi^K(\psi_i) = \int_K f_\varphi^{k_p} \psi_i + \int_K \Sigma \Delta T_h^{k_p} \psi_i = \int_K f_\varphi^{k_p} \psi_i .$$

since $T_h^k|_K \in \mathbb{P}^1(K) \forall k \geq 0$ (thus $\Delta T_h|_K = 0$).

In the case of the continuity equation we have

$$(\mathbf{f}_K^n)_i = F_n^K(\psi_i) = \int_{\partial K \cap \{\tilde{\Gamma}_R \cup \tilde{\Gamma}_N\}} v_{rec}^n \bar{n}_h \psi_i .$$

Finally, in the case of the temperature equation we have

$$\begin{aligned} (\mathbf{f}_K^T)_i &= F_T^K(\psi_i) = \int_K \sigma_T^{k_p} \nabla \varphi_h^{k_p} \cdot \nabla \varphi_h^{k_p} \psi_i + \int_K \varphi_h^{k_p} \sigma_T^{k_p} \Delta \varphi_h^{k_p} \psi_i \\ &\quad + \int_K \varphi_h^{k_p} \nabla \varphi_h^{k_p} \cdot \nabla (\sigma_T^{k_p}) \psi_i + \int_{\partial K \cap \{\partial \Omega_R \cup \partial \Omega_N\}} \gamma^T \bar{T}_h \psi_i \\ &= \int_K \sigma_T^{k_p} \nabla \varphi_h^{k_p} \cdot \nabla \varphi_h^{k_p} \psi_i + \int_{K \cap \Omega_{AM}} \varphi_h^{k_p} \nabla \varphi_h^{k_p} \cdot \nabla (\sigma_{T,AM}^{k_p}) \psi_i \\ &\quad + \int_{\partial K \cap \{\partial \Omega_R \cup \partial \Omega_N\}} \gamma^T \bar{T}_h \psi_i \end{aligned}$$

since $\varphi_h^k|_K \in \mathbb{P}^1(K)$ $\forall k \geq 0$, and $\sigma_T|_K$ is constant $\forall K \in \Omega_{M1} \cup \Omega_{M2} \cup \Omega_d$ (see (2.35)). We recall that $\sigma_{T,AM}^{k_p} = q n_h^{k_p} \mu_{n,h}^{k_p}$. In order to avoid numerical instability issues, we replace the electron mobility function with its average value over the tetrahedron $\bar{\mu}_{n,K}^{k_p} = \frac{1}{4} \sum_{i \in \mathcal{V}_K} \mu_{n,h}^{k_p}(\mathbf{x}_i)$. Thus we obtain

$$\int_{K \cap \Omega_{AM}} \varphi_h^{k_p} \nabla \varphi_h^{k_p} \cdot \nabla \left(\sigma_{T,AM}^{k_p} \right) \psi_i = q \bar{\mu}_{n,K}^{k_p} \nabla \varphi_h^{k_p} \cdot \nabla \left(n_h^{k_p} \right) \int_{K \cap \Omega_{AM}} \varphi_h^{k_p} \psi_i.$$

3.4.3 Enforcing the essential boundary conditions

So far, we have built the global matrix $\mathcal{K} = \frac{1}{\Delta t^{k+1}} \mathcal{M} + \mathcal{A}^u$ and the global load vector $\mathbf{b} = \mathbf{f}^u + \frac{1}{\Delta t^{k+1}} \mathcal{M} \mathbf{u}^k$, $\forall k \geq 0$, ignoring Dirichlet boundary conditions. These conditions can be introduced by modifying the algebraic system suitably. There are several ways to do that. We chose the “diagonalization” technique which does not alter the matrix pattern nor introduce ill-conditioning for the system. Let i_D be the generic index of a Dirichlet node (i.e., $\mathbf{x}_{i_D} \in \partial\omega_D$), we denote by \bar{u}_{i_D} the known value of the solution u_h^{k+1} at the node. We consider the Dirichlet condition as an equation of the form $a u_{i_D}^{k+1} = a \bar{u}_{i_D}$, where $a \neq 0$ is a suitable coefficient. In order to avoid degrading the global matrix condition number, we take a equal to the diagonal element of the matrix at the row i_D . Thus we perform ($\forall k \geq 0$) the imposition of the essential conditions as follows:

$\forall i_D$ s.t. $\mathbf{x}_{i_D} \in \partial\omega_D$:

1. We set to zero all off-diagonal elements of the row i_D in \mathcal{K} .
2. We set the element of the row i_D in \mathbf{b} equal to $\mathcal{K}_{i_D i_D} \bar{u}_{i_D}$.

Part III

Simulations and Results

Chapter 4

Implementation Details

4.1 Implemented Model and Solution Algorithm

In the present implementation, the heat flow equation is applied only in the simulation domain Ω_{AM} , so that the model actually used in the simulations is:

$$\begin{cases} \operatorname{div}(-\epsilon_0 \epsilon_r^{AM} \nabla \varphi) = -q n & \text{in } \Omega_{AM} \\ \operatorname{div}(-\epsilon_0 \epsilon_r^d \nabla \varphi) = 0 & \text{in } \Omega_d \\ \operatorname{div}(-\sigma_n^{M1} \nabla \varphi) = \operatorname{div}(\sigma_n^{M1} \nabla (\alpha^{M1} T)) & \text{in } \Omega_{M1} \\ \operatorname{div}(-\sigma_n^{M2} \nabla \varphi) = \operatorname{div}(\sigma_n^{M2} \nabla (\alpha^{M2} T)) & \text{in } \Omega_{M2} \\ q \frac{\partial n}{\partial t} - \operatorname{div}(q D_n \nabla n - q \mu_n n \nabla \varphi + q \mu_n n \nabla (\alpha^{AM} T)) = 0 & \text{in } \Omega_{AM}, t > 0 \\ c^{AM} \varrho^{AM} \frac{\partial T}{\partial t} - \operatorname{div}(k^{AM} \nabla T - \alpha^{AM} T \mathbf{j}_n^{drift, AM}) = -\operatorname{div}(\varphi \mathbf{j}_n^{drift, AM}) & \text{in } \Omega_{AM}, t > 0 \end{cases} \quad (4.1)$$

We refer to Chapter 2 for the characterization of the model parameters.

We consider the semi-discretization of the system (4.1), then we can formulate the general solution algorithm shown in fig. 4.1.

At each time level t^k , with $k = 0, \dots, N - 1$, we perform the following actions:

1. We compute Δt^{k+1} according to the L^2 -norm errors computed at the previous step. In fact, at the end of each time cycle in which the linear algebraic system computed from the numerical model is solved, the L^2 -norm errors $\| u^{k+1} - u^k \|_{L^2(\omega)}$ of the model equations are examined. If one of them is too high, of order of units, the time cycle is repeated with a new time step which is computed from the previous one as $\Delta t_{NEW}^{k+1} = \frac{\Delta t_{PREV}^{k+1}}{b_r}$, where b_r is a reducing factor (usually

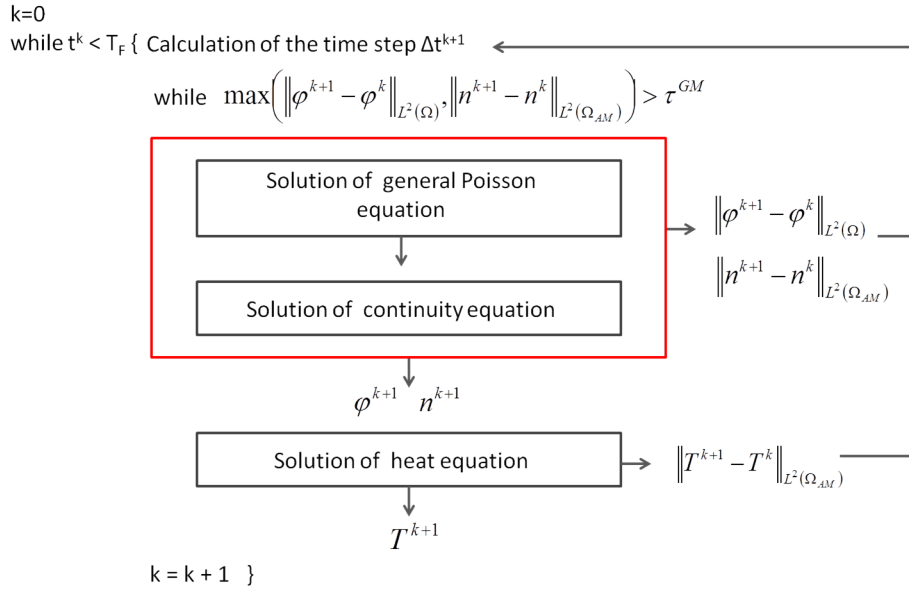


Figure 4.1: General solving algorithm for the model (4.1).

$b_r = 4 - 5$). If all the L^2 -norm errors are below a given tolerance, then the next time step is computed through the incrementation of the previous one as $\Delta t^{k+1} = b_{in} \Delta t^k$, with $b_{in} \sim 3 - 4$.

2. We start an inner loop which solves cyclically the general Poisson equation and the continuity equation. This loop is similar to the Gummel map which is a fixed point iteration method. However it differs from the Gummel map since we deal with the non linear terms in a slightly different way. The inner loop aims to ensure the consistency between the computed electrostatic potential and electron concentration. It ends when the L^2 -norm errors of both equations are below a given tolerance τ^{GM} , typically $\tau^{GM} = 10^{-3}$. We define m as the counter of this inner loop, then at each step of the loop we have:

- (a) for $m = 0 \dots M - 1$, given T^k, n^m , find φ^{m+1} s.t.

$$\begin{cases} -\operatorname{div}(\epsilon_0 \epsilon_r^{AM} \nabla \varphi^{m+1}) = -q n^m & \text{in } \Omega_{AM} \\ -\operatorname{div}(\epsilon_0 \epsilon_r^d \nabla \varphi^{m+1}) = 0 & \text{in } \Omega_d \\ -\operatorname{div}(\sigma_n^{M1} \nabla \varphi^{m+1}) = \operatorname{div}(\sigma_n^{M1} \nabla (\alpha^{M1} T^k)) & \text{in } \Omega_{M1} \\ -\operatorname{div}(\sigma_n^{M2} \nabla \varphi^{m+1}) = \operatorname{div}(\sigma_n^{M2} \nabla (\alpha^{M2} T^k)) & \text{in } \Omega_{M2} \end{cases}$$

where we set $n^0 = n^k$, and M is the maximum number of iterations for the inner loop

(b) given φ^{m+1} , find n^{m+1} s.t.

$$q \frac{n^{m+1}}{\Delta t^{k+1}} - \operatorname{div} \left(q D_n^{k,m+1} \nabla n^{m+1} - q \mu_n^{k,m+1} n^{m+1} \nabla \varphi_{te}^{k,m+1} \right) = q \frac{n^m}{\Delta t^{k+1}} \quad \text{in } \Omega_{AM}$$

with

$$\mu_n^{k,m+1} = \frac{\mu_0}{\left[1 + \left(\mu_0 \frac{|-\nabla \varphi^{m+1}|}{v_{sat}} \right)^\beta \right]^{1/\beta}} \quad \text{with } \beta = 1.109 \left(\frac{T^k}{300} \right)^{0.66}$$

$$D_n^{k,m+1} = \mu_n^{k,m+1} \frac{k_B T^k}{q} \quad \text{and} \quad \varphi_{te}^{k,m+1} = \varphi^{m+1} - \alpha^{AM} T^k$$

(c) increment $m = m + 1$.

3. We set $\varphi^{k+1} = \varphi^{m+1}$, $n^{k+1} = n^{m+1}$.

4. We solve the temperature equation:

given φ^{k+1} , n^{k+1} , find T^{k+1} s.t.

$$c^{AM} \varrho^{AM} \frac{T^{k+1}}{\Delta t^{k+1}} - \operatorname{div} \left(k^{AM} \nabla T^{k+1} - \alpha^{AM} T^{k+1} (\mathbf{j}_n^{drift,AM})^{k+1} \right) = \operatorname{div} \left(-\varphi^{k+1} (\mathbf{j}_n^{drift,AM})^{k+1} \right) + c^{AM} \varrho^{AM} \frac{T^k}{\Delta t^{k+1}} \quad \text{in } \Omega_{AM}$$

5. We increment the time counter k .

4.2 Resistive Memory Cell Geometries

4.2.1 The parallelepiped structure

We want to simulate three-dimensional devices, then the first and simplest structure we could think of is the parallelepiped shown in Fig. 4.2. The dimensions of the overall structure are $0.01 \mu m \times 0.01 \mu m \times 0.025 \mu m$. Metal 1 and Metal 2 represent the cell electrodes, active and counter for a ReRAM cell, top and bottom for a PCM cell. Figure 4.3(a) and figure 4.3(b) show the cross and longitudinal sections of the structure.

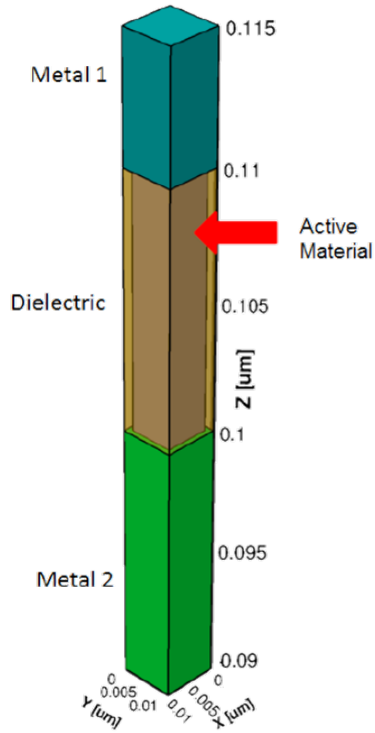
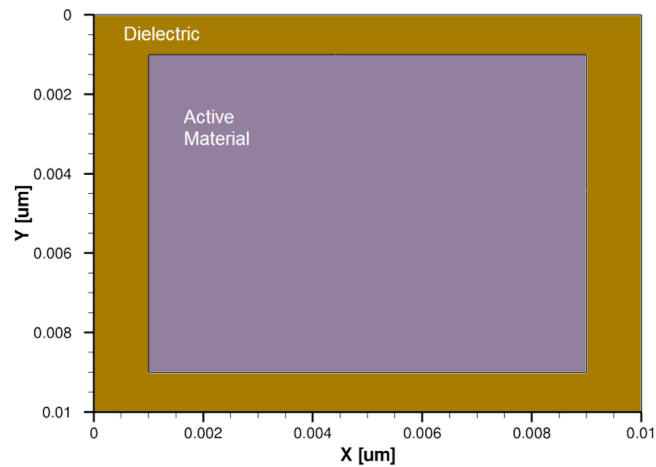


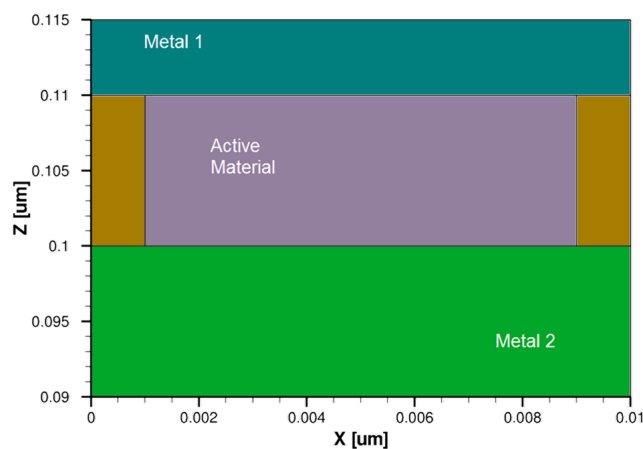
Figure 4.2: Parallelepiped structure representing a sample resistive memory cell.

We located the contacts, the surfaces to which the external potential is actually applied, at the upper face of Metal 1, and at the lower face of Metal 2 (Fig. 4.4). We will assume that across the cell electrodes there is a potential difference equal to 0.6 V. Furthermore, we will always consider the potential at Contact 2 as a reference, equal to zero, applying the potential pulse to Contact 1.

As we have already mentioned, transport processes occur only in the active material, therefore the computational domain of some equations is limited to that portion of the structure, shown in more details in Fig. 4.5.



(a) Cross section of the parallelepiped structure representing a sample resistive memory cell (at z coordinate equal to 0.1025 um).



(b) Longitudinal section of the parallelepiped structure representing a sample resistive memory cell (at y coordinate equal to 0.005 um).

Figure 4.3

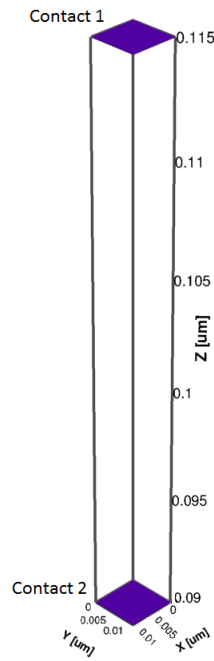


Figure 4.4: Illustration of the contacts of the parallelepiped structure representing a sample resistive memory cell.

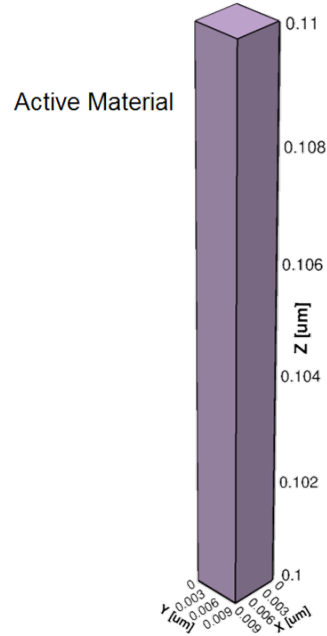


Figure 4.5: Illustration of the active material portion of the parallelepiped structure.

4.2.2 The cylindrical structure

The second, and slightly more complex structure we used to represent memory devices is a cylinder. The cylindrical structure (Fig. 4.6) has been obtained by a rotation around the x -axis of the longitudinal section of the parallelepiped structure (Fig. 4.3(b)). Fig. 4.7(a) and Fig. 4.7(b) show the cross and longitudinal section of the cylindrical structure.

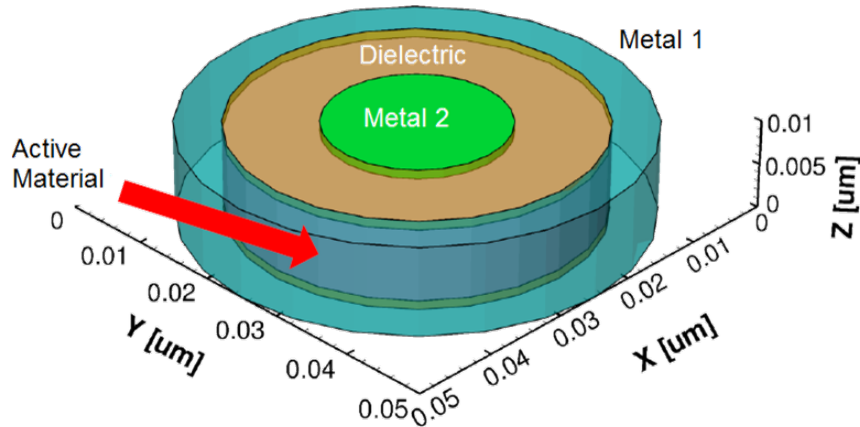
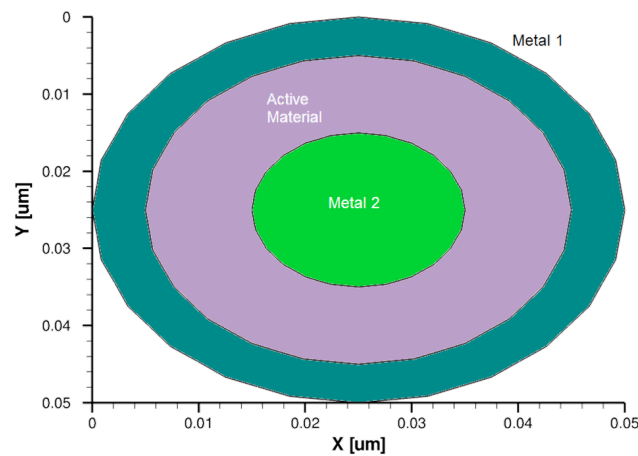


Figure 4.6: Cylindrical structure representing a sample resistive memory cell.

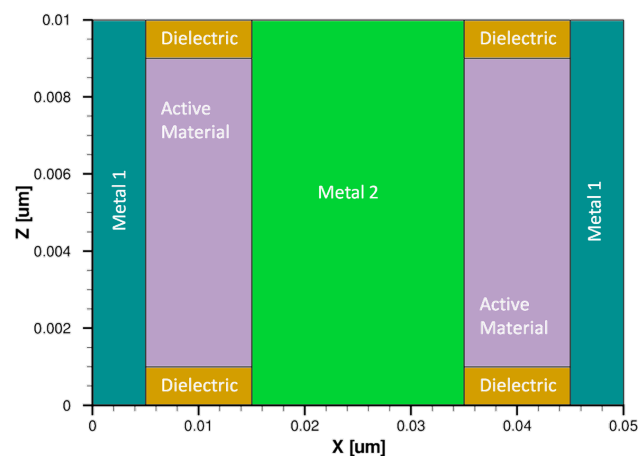
In this cylindrical cell we located the first contact along the lateral surface of Metal 1, and the second contact on the upper and lower faces of Metal 2 (Fig. 4.8).

Fig. 4.9 shows the portion of the cylindrical structure which represents the active material.

All the metals properties (physical and electrical) will be constant, functions only of the metal to which they refer. On the contrary the active layer properties will be functions of the spatial position since it may be composed of different materials. In particular, the AM properties may change along meaningful directions. For instance in the parallelepiped structure of Fig. 4.2 we will consider the AM properties as functions



(a) Cross section of the cylindrical structure representing a sample resistive memory cell (at z coordinate equal to 0.005 um).



(b) Longitudinal section of the cylindrical structure representing a sample resistive memory cell (at y coordinate equal to 0.025 um).

Figure 4.7

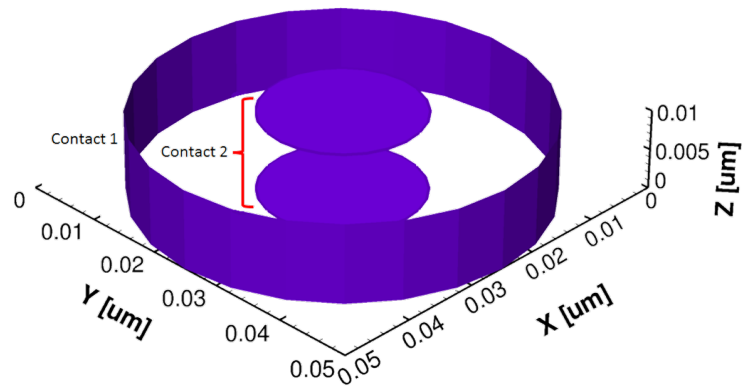


Figure 4.8: Illustration of the contacts of the cylindrical structure representing a sample resistive memory cell.

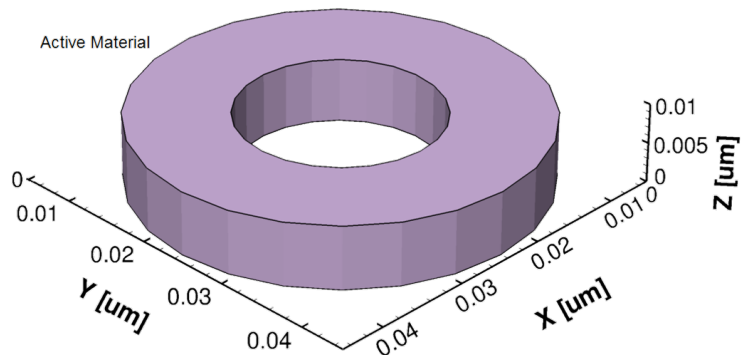


Figure 4.9: Illustration of the of the active material portion of the cylindrical structure.

of the coordinate z .

4.3 Information about the Code

As we have already mentioned, a C++ code was used to perform all numerical simulations. The code needs the following input information:

- Data about the domain grid;

The code does not deal with creating meshes. The construction of the device geometry and the corresponding mesh is controlled by a commercial software called TCAD Sentaurus. The tool Sentaurus Structure Editor has been employed to generate the 3D device geometry. Two different mesh generation tools were used to create the grids. Both tools produce finite-element meshes. For the parallelepiped structure (Fig. 4.2) we made use of the tool Sentaurus Mesh which is a robust Delaunay mesh generator producing axis-aligned meshes. Whereas for the cylindrical structure (Fig. 4.6) we used the tool Noffset3D which is an advancing front Delaunay mesh generator. As a matter of fact, this tool was more suitable for such structure since the meshes produced by it can contain layers of elements that are nearly parallel to given surfaces of the device geometry.

- Information concerning which equation must be solved;

For example the user has to specify which charge carriers (electrons and/or holes) exist in the device.

- Data about the equations parameter;

The values of the equations parameters (i.e., ϵ_r^d , ϵ_r^{AM} , σ_n^{M1} , σ_n^{M2} , μ_0 , v_{sat} , α^{AM} , k^{AM} , c^{AM} , ϱ^{AM}) must be given by the user.

- Data about the equations boundary conditions;

For each equation, the user must state the type of conditions (Dirichlet, Neumann or Robin) on each boundary surface. Furthermore, the following values have to be provided:

for Dirichlet conditions the value \bar{u} of the given solution on the surface (in the case of the potential, since $\bar{\varphi}$ can be time-dependent the user must provide the list of time instants and of the corresponding voltage values)

for Neumann conditions the value $\gamma^u \bar{u}$ of the given flow on the surface

for Robin conditions the reference value \bar{u} of the solution on the surface and the surface recombination/transfer rate γ^u .

- Data about the initial conditions;

The initial values for the electron concentration and the temperature must be provided.

- Data about the convergence criteria;

The user must specify the values of the tolerance τ^{GM} and the maximum number of iteration m_{MAX} for the inner loop (Poisson equation + continuity equation). He has also to state the value of the tolerance τ for the resolution of the algebraic systems. Unless we indicate otherwise, we choose:

$$\begin{aligned}\tau^{GM} &= 10^{-3} \\ m_{MAX} &= 10 \\ \tau &= 10^{-10}\end{aligned}$$

- Value of the maximum, minimum and initial time step, and of the initial and final instant.

Unless we indicate otherwise, we take $t^0 = \Delta t_{in} = 1\text{ ns}$, $\Delta t_{MIN} = 10^{-16}\text{ s}$ and $\Delta t_{MAX} = 1\text{ ms}$. As regards the final time instant, we usually perform the simulations until the steady solution is reached.

Chapter 5

Validation Tests

In order to prove the validity of the mathematical model (4.1) and of the implemented code, we provide some numerical results which we will compare with known exact solutions. In particular we will test the Poisson equation and the temperature equation in dielectric materials. As regards the validation of the continuity equation, we refer to INSERIRE CITAZIONE TESI GIOVANNI.

5.1 Validation of the Poisson Equation

We want to test the results of the Poisson equation within the active material. Thus the problem we are addressing is

find φ s.t.

$$\operatorname{div}(-\epsilon_0 \epsilon_r^{AM} \nabla \varphi) = -q n \quad \text{in } \Omega_{AM}$$

with the boundary conditions:

$$\varphi = 0 \quad \text{on } \Gamma_{m2} \quad \varphi = \bar{\varphi} \quad \text{on } \Gamma_{m1}$$

$$-\nabla \varphi \cdot \boldsymbol{\nu} = 0 \quad \text{on } \Gamma_d$$

where $\boldsymbol{\nu}$ is the outward unit normal vector to Γ_d .

We compare the numerical solutions obtained by our code, with the solutions of the same equation solved by the commercial software used in Micron, SDevice (a tool of TCAD Sentaurus) which uses the box discretization method ([54, 48, 55]) to discretize

the partial differential equations.

We applied $\bar{\varphi} = 4V$ at Γ_{m1} , and we set $\epsilon_r^{AM} = 10$. We performed the simulation on both the parallelepiped and the cylindrical memory cell. The results are shown in Fig. 5.1 for the parallelepiped structure and in Fig. 5.2 for the cylindrical structure. The images have been obtained applying two consecutive orthogonal cuts to the three-dimensional solutions, at $x = 0.005 \mu m$ and $y = 0.005 \mu m$ for the parallelepiped cell, and at $y = 0.025 \mu m$ and $z = 0.005 \mu m$ for the cylindrical structure. Both graphs present a very good concordance between the two potential curves.

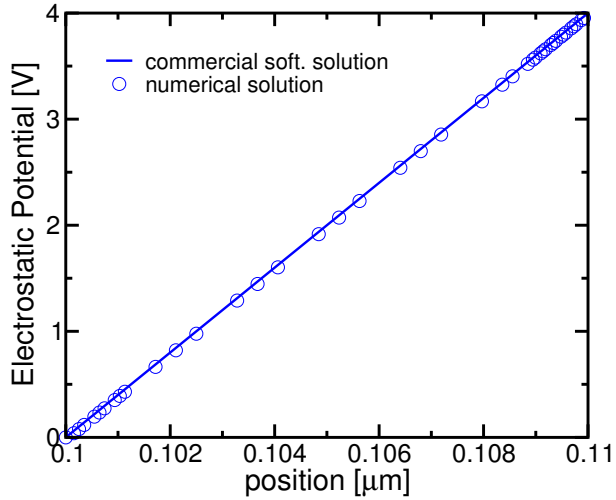


Figure 5.1: Poisson equation validation test: comparison between the potential computed with our code and the solution given by the commercial software in the parallelepiped structure.

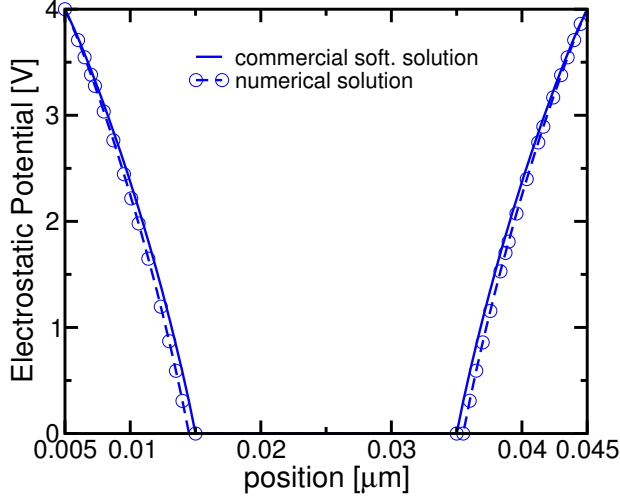


Figure 5.2: Poisson equation validation test: comparison between the potential computed with our code and the solution given by the commercial software in the cylindrical structure.

5.2 Validation of the Heat Equation

In order to validate the temperature equation, we consider a particular condition in which the three-dimensional model can be treated as a one-dimensional model of which the analytical solution can be easily computed. We use the parallelepiped structure in fig. 4.2. We set the electric field, the electron concentration and the electron mobility as constants. We also neglect the constant term (no Joule-heating effect). Thus the temperature equation becomes

for $k = 0 \dots N$, given T^k find T^{k+1} s.t.

$$\begin{aligned} c^{AM} \varrho^{AM} \frac{T^{k+1}}{\Delta^{k+1} t} - \operatorname{div} (k^{AM} \nabla T^{k+1} - c^{AM} \varrho^{AM} T^{k+1} \mathbf{v}^T) \\ = c^{AM} \varrho^{AM} \frac{T^k}{\Delta^{k+1} t} \end{aligned} \quad \text{in } \Omega_{AM} \quad (5.1)$$

where \mathbf{v}^T represents the transport speed of the temperature, given by

$$\mathbf{v}^T = \frac{\alpha^{AM}}{c^{AM} \varrho^{AM}} q n \mu_n \mathbf{E} .$$

We impose homogeneous Neumann conditions on the lateral surface of the active material, and Robin condition on the upper and lower faces with a quite high heat transfer coefficient:

$$-(k^{AM} \nabla T^{k+1} - c^{AM} \varrho^{AM} T^{k+1} \mathbf{v}^T) \cdot \boldsymbol{\nu} = 0 \quad \text{on } \Gamma_{dielectric}$$

$$\begin{aligned} - (k^{AM} \nabla T^{k+1} - c^{AM} \varrho^{AM} T^{k+1} \mathbf{v}^T) \cdot \boldsymbol{\nu} &= \gamma^T (T^{k+1} - T_{up}) \quad \text{on } \Gamma_{m1} \\ - (k^{AM} \nabla T^{k+1} - c^{AM} \varrho^{AM} T^{k+1} \mathbf{v}^T) \cdot \boldsymbol{\nu} &= \gamma^T (T^{k+1} - T_{down}) \quad \text{on } \Gamma_{m2}. \end{aligned}$$

Since $\mathbf{E} = E \mathbf{k}$ (\mathbf{k} being the z -axis), Eq. (5.1) can be reduced to the following one-dimensional equation

$$c^{AM} \varrho^{AM} \frac{T^{k+1}}{\Delta^{k+1} t} - \frac{\partial}{\partial z} \left(k^{AM} \frac{\partial}{\partial z} T^{k+1} - c^{AM} \varrho^{AM} T^{k+1} v^T \right) = c^{AM} \varrho^{AM} \frac{T^k}{\Delta^{k+1} t} \quad \text{in } (z_{in}, z_f) \quad (5.2)$$

with

$$v^T = \frac{\alpha^{AM}}{c^{AM} \varrho^{AM}} q n \mu_n E$$

and z_{in} , z_f being the initial and the final z -coordinate of the domain Ω_{AM} . The steady analytical solution of equation (5.2) is

$$T^{steady}(z) = C_1 + C_2 \exp \left(\frac{c^{AM} \varrho^{AM}}{k^{AM}} E z \right)$$

where C_1 and C_2 are constants given by the following boundary conditions

$$\begin{aligned} k^{AM} \frac{\partial}{\partial z} T^{steady}(z_{in}) - c^{AM} \varrho^{AM} T^{steady}(z_{in}) v^T &= \gamma^T (T^{steady}(z_{in}) - T_{up}) \\ -k^{AM} \frac{\partial}{\partial z} T^{steady}(z_f) + c^{AM} \varrho^{AM} T^{steady}(z_f) v^T &= \gamma^T (T^{steady}(z_f) - T_{down}). \end{aligned}$$

The local Péclet number for Eq. (5.2) is

$$Pe = \frac{v^T h_i}{2d} \quad \text{with} \quad d = \frac{k^{AM}}{c^{AM} \varrho^{AM}}$$

where $h_i = z_i - z_{i-1}$ (z_i being the nodes in (z_{in}, z_f)), and d is the thermal diffusivity ($cm^2 s^{-1}$). Hence we have that Pe is directly proportional to the temperature drift velocity v^T and inversely proportional to the thermal diffusivity d .

Table 5.1 contains the values of the parameters of the one-dimensional problem shown above that are common to all test cases. All the shown numerical solutions are steady-state and they are displayed as functions of the z -coordinate. Their images have been obtained applying two consecutive orthogonal cuts at $x = 0.005 \mu m$ and $y = 0.005 \mu m$ to the three-dimensional solutions.

z_{in}	z_f	c^{AM}	ϱ^{AM}	α^{AM}	μ_n	n_0
$0.1 \mu m$	$0.11 \mu m$	$8.8 M cm^2 s^{-2} K^{-1}$	$3980 mg cm^{-3}$	$100 \mu V K^{-1}$	$0.033 cm^2 V^{-1} s^{-1}$	$10^{20} cm^{-3}$

Table 5.1: Common parameters values for the one-dimensional model.

5.2.1 Test case 1: variation of the external temperature values

In this test we change the values of the reference external temperatures T_{up} and T_{down} . The values of the thermal conductivity, of the electric field magnitude and of the heat transfer coefficient are shown in table 5.2. We performed three simulations, fig-

k^{AM}	E	γ^T
$0.3 W cm^{-1} K^{-1}$	$-11.58 M V cm^{-1}$	$1170 W cm^{-2} K^{-1}$

Table 5.2: Temperature equation validation test 1: common parameters values.

ures 5.3(a), (b) and (c) show the comparison between the numerical steady solutions and the analytical solutions corresponding to the values

- a) $T_{up} = 300 K$ and $T_{down} = 310 K$,
- b) $T_{up} = 310 K$ and $T_{down} = 300 K$,
- c) $T_{up} = 300 K$ and $T_{down} = 900 K$.

The Péclet number in this test case is quite small (~ 0.001) although the electric field is high, because the value of the thermal conductivity is also high. We tested opposite temperature boundary conditions and also a quite high imposed temperature gradient. The heat transfer coefficient has a rather high value, therefore the Robin conditions at the boundaries are actually similar to Dirichlet conditions.

All the simulated cases indicate an excellent concordance between the analytical solutions and the computed steady solutions. The solutions of the cases (a) and (b), which have opposite boundary conditions ($T_{up}^{(a)} = T_{down}^{(b)}$, $T_{down}^{(a)} = T_{up}^{(b)}$) are perfectly symmetrical. In all the three cases the steady solution exhibits a linear characteristic, whence we can state that the diffusion is dominant over the transport.

5.2.2 Test case 2: variation of the thermal conductivity

In this test the thermal conductivity k^{AM} is varied in the range $0.003 - 3 W cm^{-1} K^{-1}$. The values of the boundary external temperatures, of the electric field magnitude and

T_{down}	T_{up}	E	γ^T
310 K	300 K	$-11.58 \text{ M V cm}^{-1}$	$1170 \text{ W cm}^{-2}\text{K}^{-1}$

Table 5.3: Temperature equation validation test 2: common parameters values.

of the heat transfer coefficient are shown in table 5.3. Figures 5.4(a), (b), (c) and (d) show the comparison between the numerical steady solutions and the analytical solutions corresponding to the values

- a) $k^{AM} = 0.003 \text{ W cm}^{-1}\text{K}^{-1}$,
- b) $k^{AM} = 0.03 \text{ W cm}^{-1}\text{K}^{-1}$,
- c) $k^{AM} = 0.3 \text{ W cm}^{-1}\text{K}^{-1}$,
- d) $k^{AM} = 3 \text{ W cm}^{-1}\text{K}^{-1}$.

Changing the thermal conductivity corresponds to modifying the Péclet number, the larger the value of k^{AM} , the more we are reducing the value of the Péclet number (see Table 5.4). We note that the concordance between the analytical solutions and the

k^{AM}	$0.003 \text{ W cm}^{-1}\text{K}^{-1}$	$0.03 \text{ W cm}^{-1}\text{K}^{-1}$	$0.3 \text{ W cm}^{-1}\text{K}^{-1}$	$3 \text{ W cm}^{-1}\text{K}^{-1}$
Pe	0.1	0.01	0.001	0.0001

Table 5.4: Temperature equation validation test 2: values of the Péclet number for different values of the thermal conductivity.

computed steady solutions are excellent for all the cases except for case (a). Such case has a very low value of the thermal conductivity, resulting in a higher value of the Péclet number. This means that in the case $k^{AM} = 0.003 \text{ W cm}^{-1}\text{K}^{-1}$ the advection is slightly dominant (it can also be seen by the fact that the solution is not exactly linear). The electric field is directed in the opposite direction to the z axis, and, indeed, the temperature is conveyed towards the surface Γ_{m2} . The result is that the numerical solution at $z = 0.1 \mu\text{m}$ is a little higher than the value T_{down} . We also notice that in case (d), the approximate solution at the boundaries distances itself, albeit slightly, from the imposed conditions. In this case the value of the thermal conductivity is quite high, thus the diffusion is dominant and tends to make the temperature uniform in the active material, thus lowering its value at the borders.

Finally we want to remark that with the decreasing of the thermal conductivity, the time needed to reach the steady solution increases (see Fig. 5.5).

5.2.3 Test case 3: dominant transport

In this test we want to check the reliability of the numerical solution in dominant advection condition. We set “extreme” conditions (see table 5.5): high electric field and wide imposed temperature gradient. We performed three simulations with very low

T_{down}	T_{up}	E	γ^T
900 K	300 K	$-11.58 \text{ MV cm}^{-1}$	$1170 \text{ W cm}^{-2} \text{K}^{-1}$

Table 5.5: Temperature equation validation test 3: common parameters values.

values of thermal conductivity

- a) $k^{AM} = 0.1 \text{ mW cm}^{-1} \text{K}^{-1}$,
- b) $k^{AM} = 0.5 \text{ mW cm}^{-1} \text{K}^{-1}$,
- c) $k^{AM} = 1 \text{ mW cm}^{-1} \text{K}^{-1}$.

Therefore in all the three cases the transport is dominant with respect to diffusion. Smaller the value of k^{AM} , the more the value of the Péclet number is increasing (see Table 5.6).

k^{AM}	$0.1 \text{ mW cm}^{-1} \text{K}^{-1}$	$0.5 \text{ mW cm}^{-1} \text{K}^{-1}$	$1 \text{ mW cm}^{-1} \text{K}^{-1}$
Pe	3	0.6	0.3

Table 5.6: Temperature equation validation test 3: values of the Péclet number for different values of the thermal conductivity.

Figures 5.6(a), (b) and (c) show the comparison between the analytical solutions and the computed numerical solution. The concordance is very good. The numerical solutions do not exhibit a linear characteristic, but, instead, they show an exponential behavior, more and more evident as k^{AM} decreases. This occurs because the transport acquires greater incidence compared to the diffusion. The transport effect is particularly visible in the case $k^{AM} = 0.1 \text{ mW cm}^{-1} \text{K}^{-1}$. As we mentioned in the previous section, the electric field is directed in the opposite direction to the z axis, thus the temperature is conveyed towards the surface Γ_{m2} . One can notice that even if the values of the thermal conductivity in the cases (b) and (c) are lower than $3 \text{ mW cm}^{-1} \text{K}^{-1}$, the advection is less evident with respect to the case (a) of the previous section. We recall that the driving force are two: the electric field and the temperature gradient on the active material. In all cases the temperature gradient has the opposite direction to the

electric field, but, in case (a) of test 2 the temperature gradient is quite small (10 K over $0.010\text{ }\mu\text{m}$), while in cases (b) and (c) of test 3 it is much larger (600 K over $0.01\text{ }\mu\text{m}$). Therefore, in the latter, we have that the diffusion has a greater weight, although the thermal conductivity values are lower.

5.2.4 Test case 4: variation of the heat transfer coefficient

In this test we change the value of the heat transfer coefficient. Table shows the values of the electric field, of the thermal conductivity and of the boundaries external temperatures. Figures 5.7(a), (b), (c) and (d) show the comparison between the numerical

T_{down}	T_{up}	E	k^{AM}
900 K	300 K	-11.58 MV cm^{-1}	$0.3\text{ W cm}^{-1}\text{K}^{-1}$

Table 5.7: Temperature equation validation test 4: common parameters values.

steady solutions and the analytical solutions corresponding to the values

- a) $\gamma^T = 0.117\text{ W cm}^{-2}\text{K}^{-1}$,
- b) $\gamma^T = 11.7\text{ W cm}^{-2}\text{K}^{-1}$,
- c) $\gamma^T = 1170\text{ W cm}^{-2}\text{K}^{-1}$,
- d) $\gamma^T = 117\text{ KW cm}^{-2}\text{K}^{-1}$.

The concordance between the analytical solutions and the computed numerical solutions is very good. We recall that the higher the value of the heat transfer coefficient, the more Robin conditions approach those of Dirichlet. This is quite evident from the images in Fig. 5.7. As a matter of fact, in correspondence to the lower values of the transfer coefficient the imposed external values T_{up} and T_{down} affect less and less the values of the temperature at the surfaces Γ_{m1} and Γ_{m2} , respectively. At the same time the internal driving forces influence increasingly the boundary values of the temperature. In this test the diffusion is dominant, thus we have that the temperature tends to become uniform in the active material. Therefore we have that the temperature values at the edge surfaces decrease as the heat transfer rate decreases. Finally we want to observe that with the decreasing of the heat transfer coefficient the time needed to reach the steady solution increases (see Fig. 5.8).

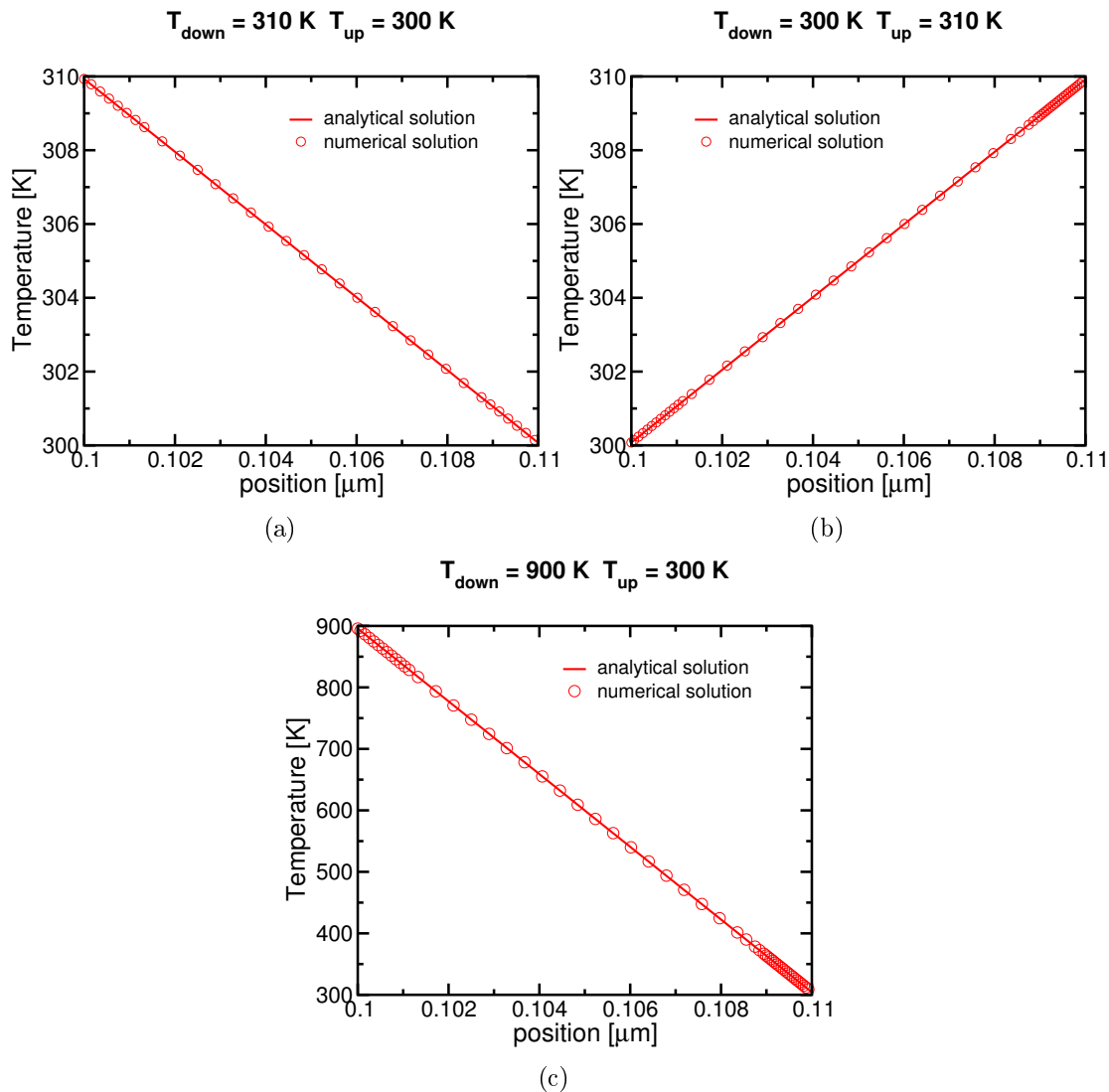


Figure 5.3: Temperature equation validation test 1: comparison between analytical solutions and numerical solutions with different values of the external temperatures for the boundary conditions.

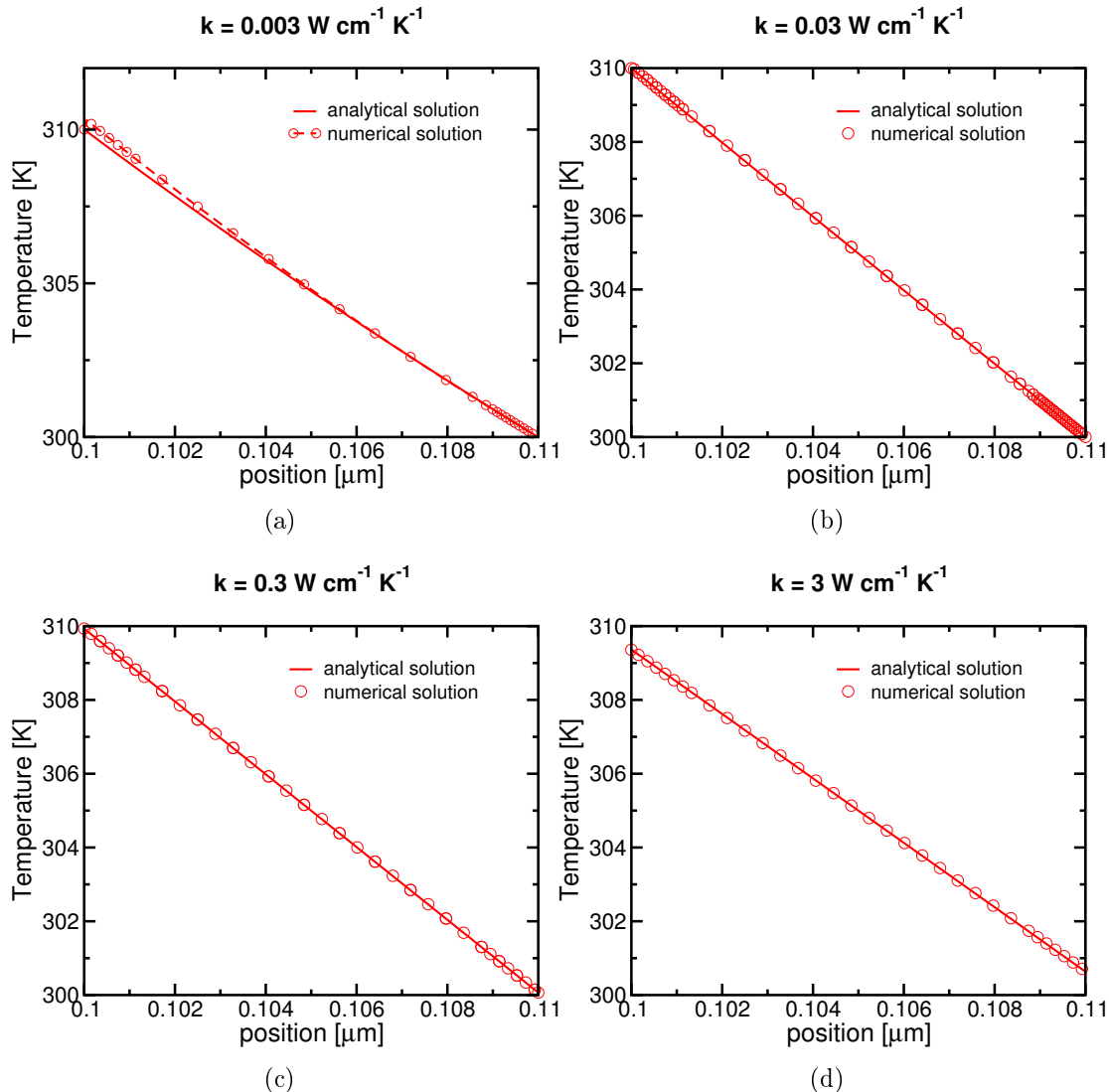


Figure 5.4: Temperature equation validation test 2: comparison between analytical solutions and numerical solutions with different values of the thermal conductivity.

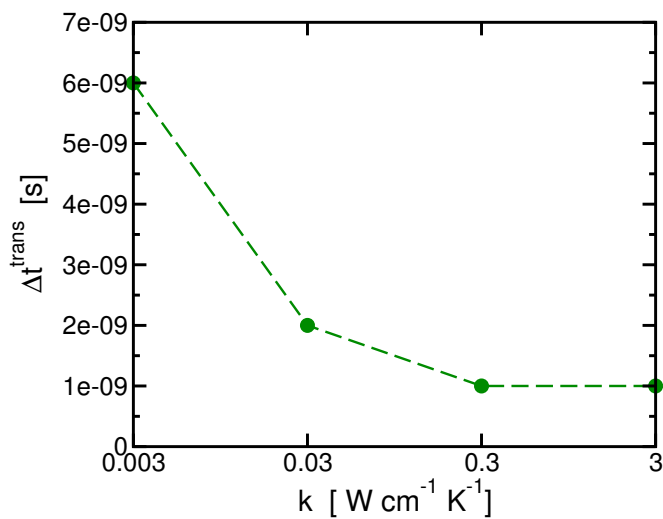


Figure 5.5: Temperature equation validation test 2: illustration of the duration of the transient regime Δt^{trans} as a function of the thermal conductivity.

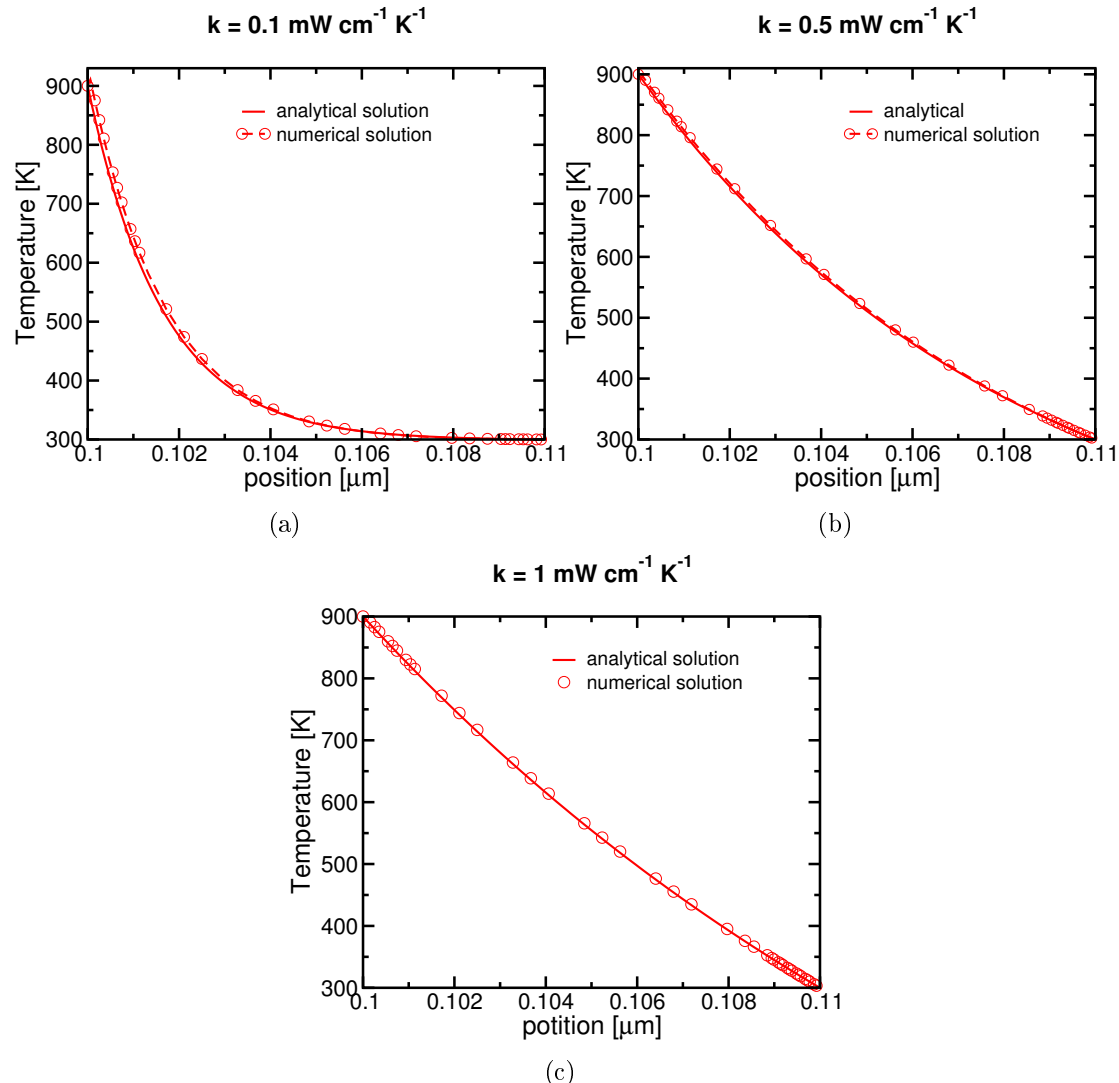


Figure 5.6: Temperature equation validation test 3: comparison between analytical solutions and numerical solutions with different values of the thermal conductivity.

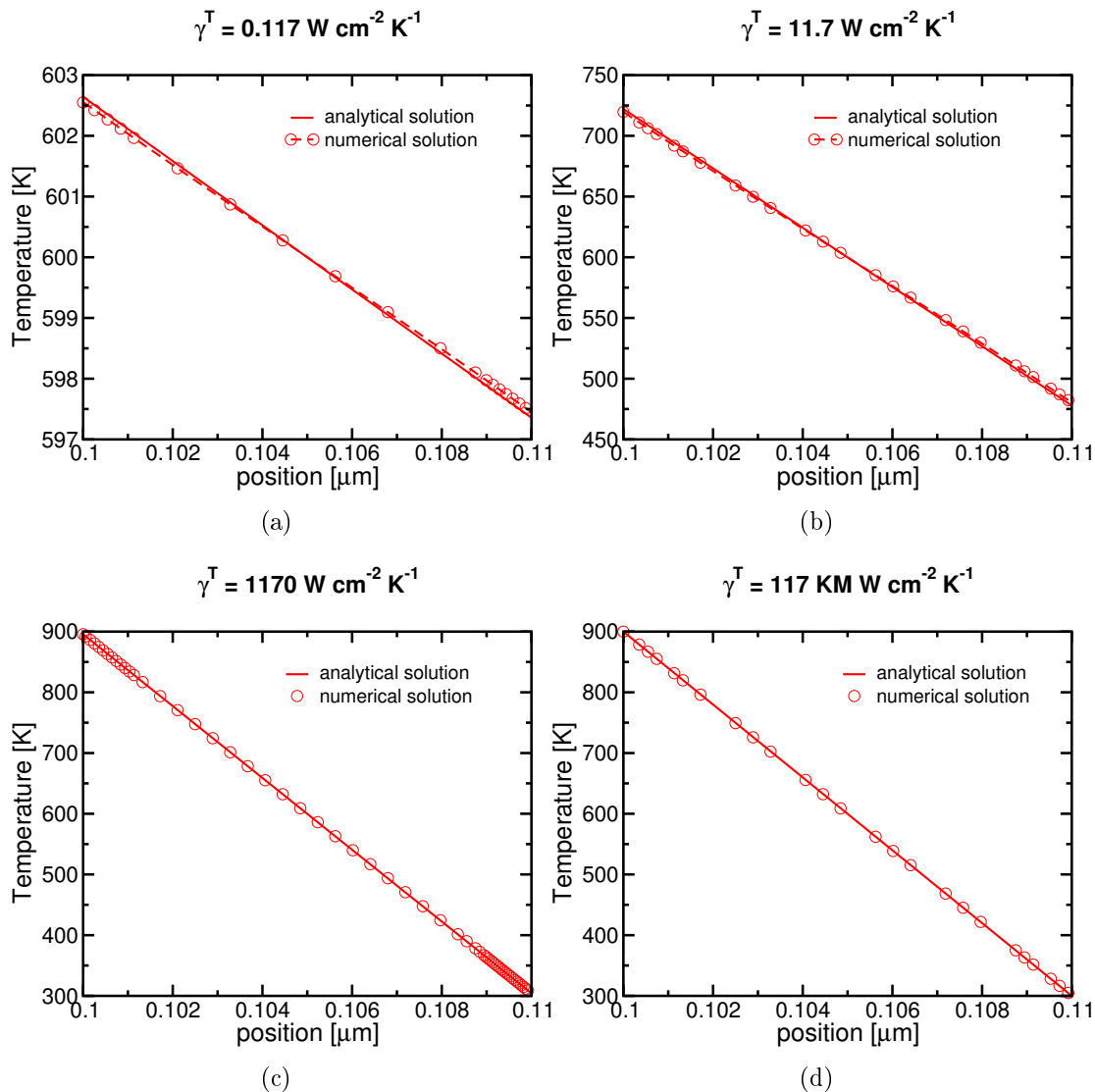


Figure 5.7: Temperature equation validation test 4: comparison between analytical solutions and numerical solutions with different values of the heat transfer coefficient.

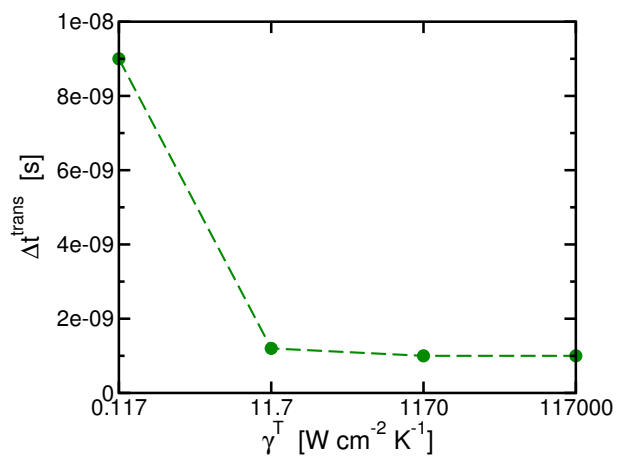


Figure 5.8: Temperature equation validation test 4: illustration of the duration of the transient regime Δt^{trans} as a function of the heat transfer coefficient.

Chapter 6

Simulations

All the shown numerical results are steady-state.

6.1 Analysis of the Thermal Shift of Electrons

We want to study the electron transport due to the thermal field $-\nabla(\alpha^{AM}T)$. As we said in the previous chapter, charge carriers tend to respond to a temperature gradient by moving in the opposite direction, i.e. from the hot end to the cold end. We will analyze the electron displacement as the thermoelectric field changes. We will vary the temperature gradient imposed through the boundary conditions, and the value of the thermopower. We perform the simulations on the parallelepiped structure (Fig. 4.2).

We impose homogeneous Neumann boundary conditions for the continuity equation, i.e.

$$-\mathbf{j}_n^{AM} \cdot \boldsymbol{\nu} = 0 \quad \text{on } \Gamma_{diel} \cup \Gamma_{m1} \cup \Gamma_{m2}$$

with \mathbf{j}_n^{AM} given by (2.30). The electron concentration is initially uniform (equal to n_0). With these boundary conditions we are confining the electrons in the active material so that they can move within it but not get out. For the temperature equations we impose the following conditions

$$-\mathbf{j}_T^{AM} \cdot \boldsymbol{\nu} = 0 \quad \text{on } \Gamma_{diel}$$

$$-\mathbf{j}_T^{AM} \cdot \boldsymbol{\nu} = \gamma^T (T - T_{up}) \quad \text{on } \Gamma_{m1} \quad -\mathbf{j}_T^{AM} \cdot \boldsymbol{\nu} = \gamma^T (T - T_{down}) \quad \text{on } \Gamma_{m2}$$

with

$$\mathbf{j}_T^{AM} = k^{AM} \nabla T - \alpha^{AM} T \mathbf{j}_n^{drift,AM}.$$

We make void the electric field. Tables 6.2 and 6.1 show the parameters used for the continuity equation and the heat equation, respectively.

v_{rec}^n	v_{sat}	μ_0	n_0
$11.7 M \text{ cm s}^{-1}$	$10 M \text{ cm s}^{-1}$	$0.03 \text{ cm}^2 \text{ V}^{-1} \text{ s}^{-1}$	10^{14} cm^{-3}

Table 6.1: Study of the thermal transport of electrons: common parameters values for the continuity equation.

c^{AM}	ϱ^{AM}	k^{AM}	γ^T
$8.8 M \text{ cm}^2 \text{ s}^{-2} \text{ K}^{-1}$	3980 mg cm^{-3}	$0.3 W \text{ cm}^{-1} \text{ K}^{-1}$	$1170 W \text{ cm}^{-2} \text{ K}^{-1}$

Table 6.2: Study of the thermal transport of electrons: common parameters values for the temperature equation.

First we set $\alpha^{AM} = 100 \mu \text{V K}^{-1}$, and we change the values of the external temperatures T_{up} and T_{down} . Figure 6.1 shows the temperature fields and the corresponding electron concentration curves referring to the values

a-b) $T_{down} = 300 \text{ K}$ and $T_{up} = 400 \text{ K}$,

c-d) $T_{down} = 400 \text{ K}$ and $T_{up} = 300 \text{ K}$,

e-f) $T_{down} = 300 \text{ K}$ and $T_{up} = 600 \text{ K}$.

The images are obtained cutting the structure at $y = 0.005 \mu\text{m}$, then applying a transformation to the reference system. The xz -plane becomes the xy -plane, while along the z -axis there is the value of the variable. Figure 6.2 shows the comparison between the electron concentration curves in the three cases above. The concentrations are displayed as functions of the z -coordinate, this is significant because the only driving force for the electrons is the temperature gradient which is directed as the z -axis. The image has been obtained cutting the structure at $x = 0.005 \mu\text{m}$ and then at $y = 0.005 \mu\text{m}$. In all simulations the electrons move towards the coldest point of the active material where the electron concentration increases with respect to the initial value n_0 . Accordingly the electron concentration in the hottest spot decreases. This is due to the fact that we imposed homogeneous Neumann conditions, therefore the quantity $\int_{\Omega_{AM}} n(\mathbf{x}) d\mathbf{x}$ is

preserved. We can observe that the first two cases present opposite values of the external temperatures and, indeed, the corresponding concentration curves are symmetric. Comparing the first and the last case we have that their temperature gradients have the same direction, thus, in both tests the electrons travel towards Γ_{m2} . Moreover, when the temperature gradient is larger, the value of the electron concentration is higher on this surface, and accordingly, it is lower at the opposite interface, Γ_{m1} .

Now we set $T_{down} = 300\text{ K}$ - $T_{up} = 400\text{ K}$, and we change the value of the thermopower α^{AM} . The temperature field then is the one in 6.1(a), while the in fig. 6.3 are shown the electron concentrations corresponding to the values

a) $\alpha^{AM} = 10^{-4}\text{ V K}^{-1}$,

b) $\alpha^{AM} = 10^{-3}\text{ V K}^{-1}$,

c) $\alpha^{AM} = 10^{-5}\text{ V K}^{-1}$.

Also in this case, the images are obtained cutting the structure at $y = 0.005\mu\text{m}$, and applying a transformation to the reference system. The xz -plane becomes the xy -plane, while along the z -axis there is the value of the variable. In figure 6.4 the electron concentration curves of the three cases above are compared as functions of the z -coordinate. The image has been obtained cutting the structure at $x = 0.005\mu\text{m}$ and then at $y = 0.005\mu\text{m}$. In all simulations the electrons move towards the coldest point of the active material, and the displacement is greater the more the value of the thermopower is high. When α^{AM} is very low (case c) the electron concentration remains almost unchanged, and thus uniform, with respect to the initial value n_0 . As the thermopower increases, the electrons travel from Γ_{m1} to Γ_{m2} .

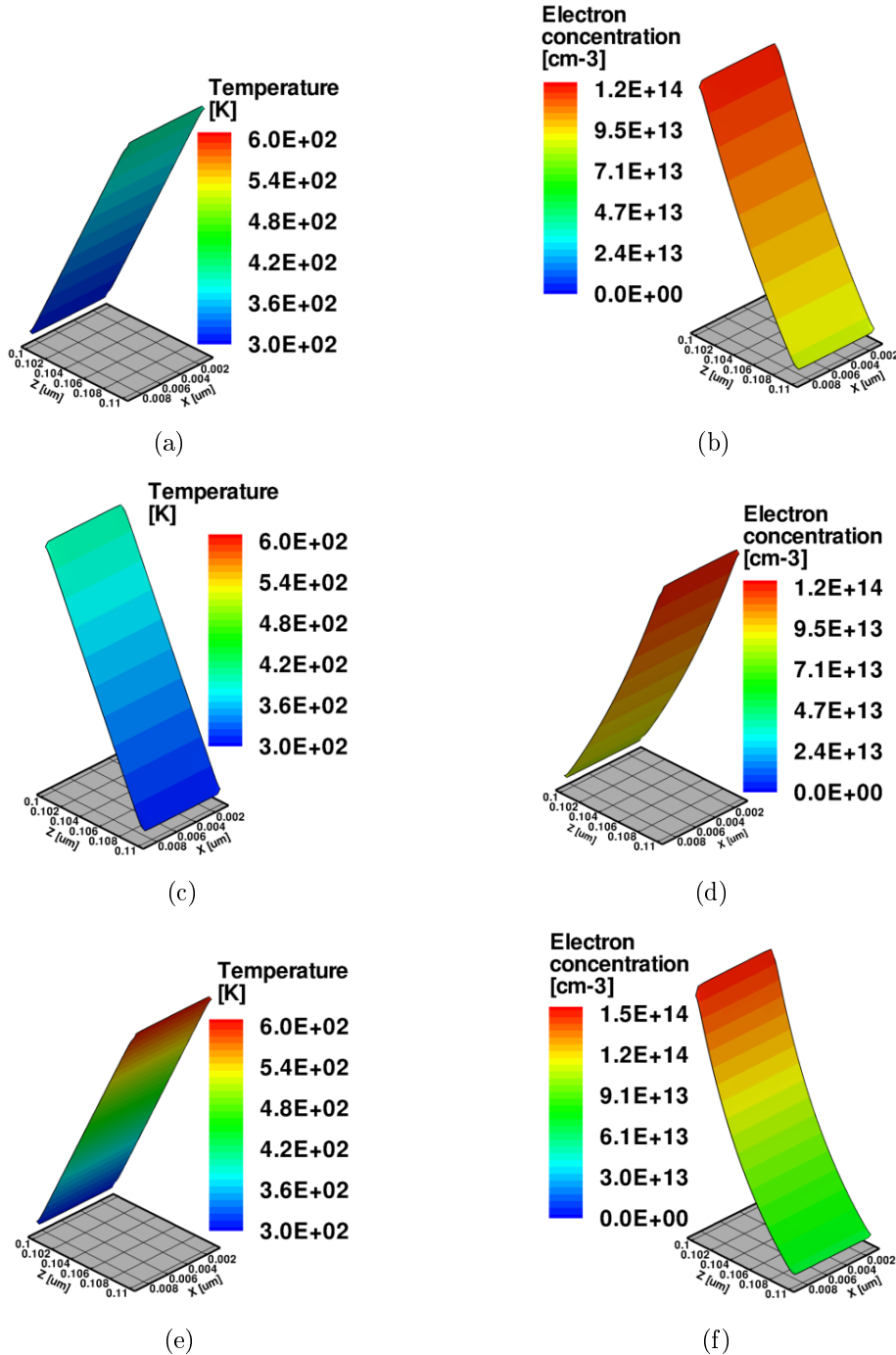


Figure 6.1: Study of the thermal transport of electrons: temperature fields and corresponding electron concentrations in the active material for different values of the external temperatures in the boundary conditions. The images are obtained cutting the structure at $\hat{z} = 0$, then applying a transformation to the reference system. The xz -plane becomes the xy -plane, while along the z -axis there is the value of the variable.

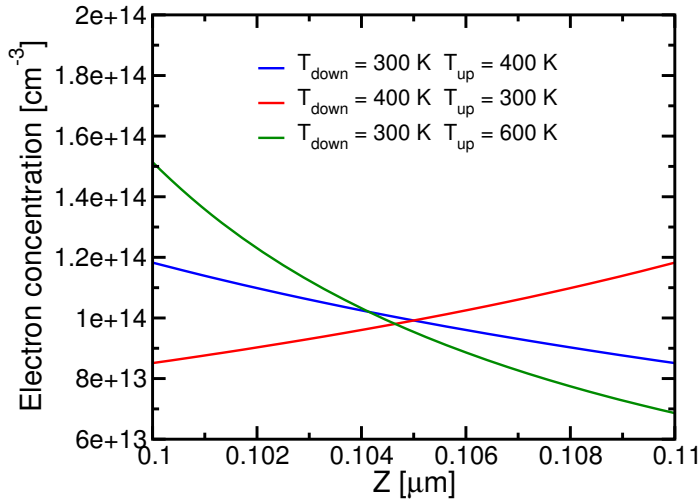


Figure 6.2: Study of the thermal transport of electrons: electron concentrations along the z -axis for different values of the external temperatures in the boundary conditions. The image has been obtained cutting the structure at $x = 0.005 \mu m$ and then at $x = 0.005 \mu m$.

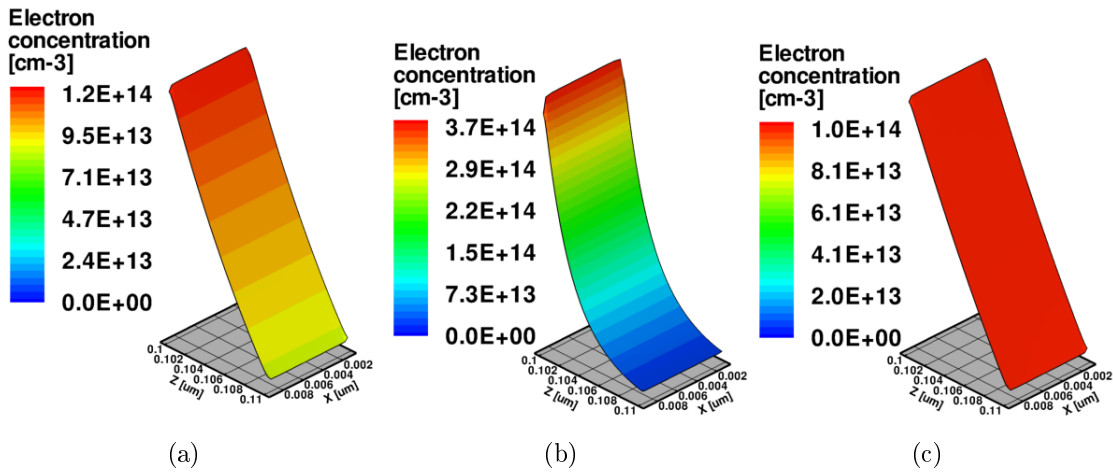


Figure 6.3: Study of the thermal transport of electrons: electron concentrations in the active material for different values of the thermopower. The images are obtained cutting the structure at $y = 0.005 \mu m$, then applying a transformation to the reference system. The xz -plane becomes the xy -plane, while along the z -axis there is the value of the electron concentration.

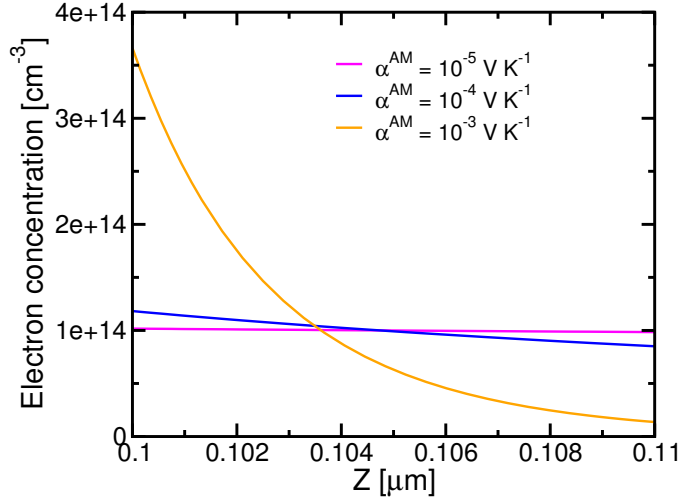


Figure 6.4: Study of the thermal transport of electrons: electron concentrations along the $-z$ -axis for different values of the thermopower. The image has been obtained cutting the structure at $x = 0.005 \mu m$ and then at $y = 0.005 \mu m$.

6.2 Heterogeneous Properties

As we explained in part II, the active material could be formed not from a single material, but from several different materials. Even in the case when it consists of one material, the active layer may have properties which are dependent on the spatial coordinates. However we always assume that the AM properties are piecewise constant. In this test we consider three different set of parameters for the active material, and we observe how they affect the temperature field and the electron concentration evolution. We performed the simulations on the parallelepiped structure (Fig. 4.2).

We applied $\bar{\varphi} = 1 V$ at Γ_{C1} , and we impose the following boundary conditions for the continuity equation

$$-\mathbf{j}_n^{AM} \cdot \boldsymbol{\nu} = v_{rec}^n (n - 10^{16}) \quad \text{on } \Gamma_{m1} \quad \text{and} \quad -\mathbf{j}_n^{AM} \cdot \boldsymbol{\nu} = v_{rec}^n (n - 10^{10}) \quad \text{on } \Gamma_{m2} \cup \Gamma_{diel}$$

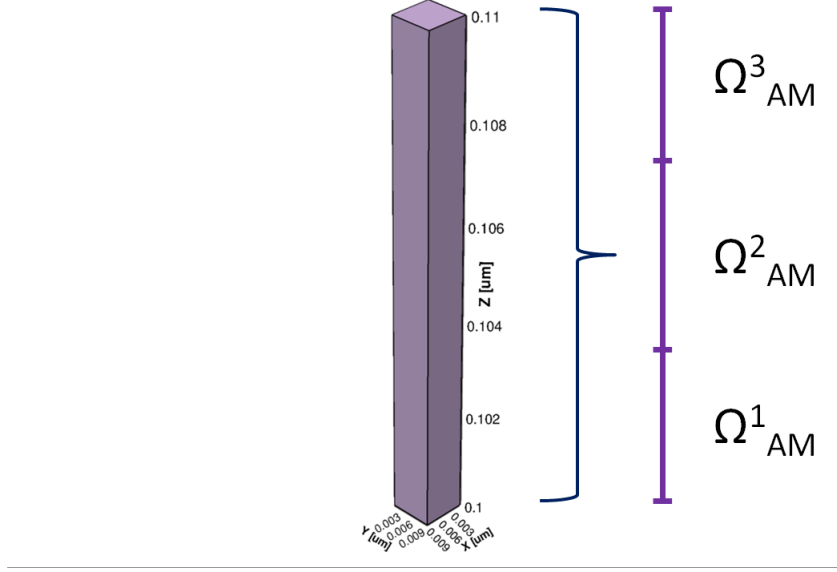
and for the temperature equation

$$\begin{aligned} -\mathbf{j}_T^{AM} \cdot \boldsymbol{\nu} &= \gamma^T (T - 600) \quad \text{on } \Gamma_{m1} \\ -\mathbf{j}_T^{AM} \cdot \boldsymbol{\nu} &= \gamma^T (T - 300) \quad \text{on } \Gamma_{m2} \cup \Gamma_{diel}. \end{aligned}$$

The values of the common parameters are shown in table 6.3 (where $\epsilon_r = \epsilon_r^{AM} = \epsilon_r^d$).

ϵ_r	σ_n^{M1}	σ_n^{M2}	v_{sat}	n_0	v_{rec}^n	γ^T
10	$10^{17} S \text{ cm}^{-1}$	$10^{18} S \text{ cm}^{-1}$	$10 M \text{ cm s}^{-1}$	10^{10} cm^{-3}	$20 K \text{ cm s}^{-1}$	$1000 W \text{ cm}^{-2} K^{-1}$

Table 6.3: Test on heterogeneous AM properties: values of the common parameters.

Figure 6.5: Test on heterogeneous AM properties: subdivision of the active material in three layers along the z -axis.

We split the active material in three layers along the z -axis, each characterized by different properties (Fig. 6.5). The sub-domains Ω_{AM}^1 , Ω_{AM}^2 , and Ω_{AM}^3 have dimensions equal to $0.008 \mu\text{m} \times 0.008 \mu\text{m} \times 0.003 \mu\text{m}$, $0.008 \mu\text{m} \times 0.008 \mu\text{m} \times 0.004 \mu\text{m}$, and $0.008 \mu\text{m} \times 0.008 \mu\text{m} \times 0.003 \mu\text{m}$, respectively. The properties that will vary in the active layer are the reference electron mobility, the specific heat, the mass density and the thermal conductivity. Thus the physical quantities which will actually be modified are the electron mobility and the thermal diffusivity. Tables 6.4, 6.5, and 6.6 show the values of the three set of parameters that we want to test.

Figure 6.6 shows the potential curve which is the same for all the parameter sets.

	μ_0	c^{AM}	ϱ^{AM}	k^{AM}
Ω_{AM}^1	$0.03 \text{ cm}^2 \text{V}^{-1} \text{s}^{-1}$	$8.8 M \text{ cm}^2 \text{s}^{-2} K^{-1}$	$3980 mg \text{ cm}^{-3}$	$0.3 W \text{ cm}^{-1} K^{-1}$
Ω_{AM}^2	$3 M \text{ cm}^2 \text{V}^{-1} \text{s}^{-1}$	$8.8 M \text{ cm}^2 \text{s}^{-2} K^{-1}$	$3980 mg \text{ cm}^{-3}$	$0.03 W \text{ cm}^{-1} K^{-1}$
Ω_{AM}^3	$3 \mu \text{ cm}^2 \text{V}^{-1} \text{s}^{-1}$	$8.8 M \text{ cm}^2 \text{s}^{-2} K^{-1}$	$3980 mg \text{ cm}^{-3}$	$3 W \text{ cm}^{-1} K^{-1}$

Table 6.4: Test on heterogeneous AM properties: parameter set A.

	μ_0	c^{AM}	ϱ^{AM}	k^{AM}
Ω_{AM}^1	$3 M \text{ cm}^2 \text{ V}^{-1} \text{ s}^{-1}$	$8.8 M \text{ cm}^2 \text{ s}^{-2} \text{ K}^{-1}$	3980 mg cm^{-3}	$0.003 W \text{ cm}^{-1} \text{ K}^{-1}$
Ω_{AM}^2	$3 M \text{ cm}^2 \text{ V}^{-1} \text{ s}^{-1}$	$8.8 M \text{ cm}^2 \text{ s}^{-2} \text{ K}^{-1}$	3980 mg cm^{-3}	$0.003 W \text{ cm}^{-1} \text{ K}^{-1}$
Ω_{AM}^3	$3 \mu \text{ cm}^2 \text{ V}^{-1} \text{ s}^{-1}$	$8.8 M \text{ cm}^2 \text{ s}^{-2} \text{ K}^{-1}$	3980 mg cm^{-3}	$3 W \text{ cm}^{-1} \text{ K}^{-1}$

Table 6.5: Test on heterogeneous AM properties: parameter set B.

	μ_0	c^{AM}	ϱ^{AM}	k^{AM}
Ω_{AM}^1	$3 M \text{ cm}^2 \text{ V}^{-1} \text{ s}^{-1}$	$88 M \text{ cm}^2 \text{ s}^{-2} \text{ K}^{-1}$	$3980 g \text{ cm}^{-3}$	$0.3 mW \text{ cm}^{-1} \text{ K}^{-1}$
Ω_{AM}^2	$3 \mu \text{ cm}^2 \text{ V}^{-1} \text{ s}^{-1}$	$88 M \text{ cm}^2 \text{ s}^{-2} \text{ K}^{-1}$	$3980 g \text{ cm}^{-3}$	$0.3 mW \text{ cm}^{-1} \text{ K}^{-1}$
Ω_{AM}^3	$0.03 cm^2 \text{ V}^{-1} \text{ s}^{-1}$	$8.8 M \text{ cm}^2 \text{ s}^{-2} \text{ K}^{-1}$	$3980 mg \text{ cm}^{-3}$	$3 W \text{ cm}^{-1} \text{ K}^{-1}$

Table 6.6: Test on heterogeneous AM properties: parameter set C.

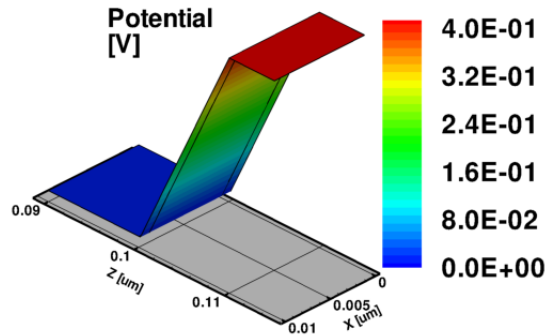


Figure 6.6: Test on heterogeneous AM properties: electrostatic potential. The image is obtained cutting the structure at $y = 0.005 \mu\text{m}$, then applying a transformation to the reference system. The xz -plane becomes the xy -plane, while along the z -axis there is the value of the electrostatic potential.

In Fig. 6.7 we have the graphs of the temperature and of the electron concentration for the three set of parameters which we are analyzing. As usual, the images are obtained cutting the structure at $y = 0.005 \mu m$, then applying a transformation to the reference system. The xz -plane becomes the xy -plane, while along the z -axis there is the value of the variable. Figure 6.8 shows the comparison of the temperature curves and of the electron concentrations of the different parameter sets, along the z -direction. The image has been obtained cutting the structure at $x = 0.005 \mu m$ and then at $y = 0.005 \mu m$. We observe that the temperatures are not so different, in fact, for set A and set B they are almost the same. We can conclude that changing only the value of the conductivity is not sufficient to significantly modify the thermal diffusivity. On the other hand, when we also increase the values of the specific heat and of the mass density, in set C, we obtain an evident change in the temperature curve. In fact, the temperature has no longer a linear behavior, but shows a lower growth.

In the parameter set A, we chose a medium value for the reference mobility in Ω_{AM}^1 , a very high value in Ω_{AM}^2 , and finally a very low value in Ω_{AM}^3 . As a results electrons move from Γ_{m2} at a moderate speed (the electron concentration at the surface is a little lower than the reference value $10^{16} cm^{-3}$), while Ω_{AM}^2 empties quickly, and, at the surface Γ_{m1} , there is a small accumulation of electrons (the concentration is above the reference value $10^{10} cm^{-3}$). In set B, we imposed a very high value for the reference mobility in Ω_{AM}^1 and Ω_{AM}^2 , and finally a very low value in Ω_{AM}^3 . Therefore electrons move very fast from Γ_{m2} (the electron concentration at the surface is much lower than the reference value), and in both Ω_{AM}^1 and Ω_{AM}^2 the electron concentration is quite low. At the surface Γ_{m1} , the accumulation of electrons has increased with respect to the case of parameter set A. This is due to the fact that the flux of electrons that arrive in Ω_{AM}^3 is larger, but the mobility in this sub-domain and the recombination speed at Γ_{m1} are unchanged. In set C, we fixed a very high value for the reference mobility in Ω_{AM}^1 , a very low value in Ω_{AM}^2 , and finally a medium value in Ω_{AM}^3 . Therefore electrons move very fast from Γ_{m2} (the electron concentration at the surface is much lower than the reference value), and Ω_{AM}^1 empties quickly. Then the electron flow is slowed in Ω_{AM}^2 , resulting in a change accumulation. Finally in Ω_{AM}^3 , the electrons speed increases again, leading the electron concentration to decrease.

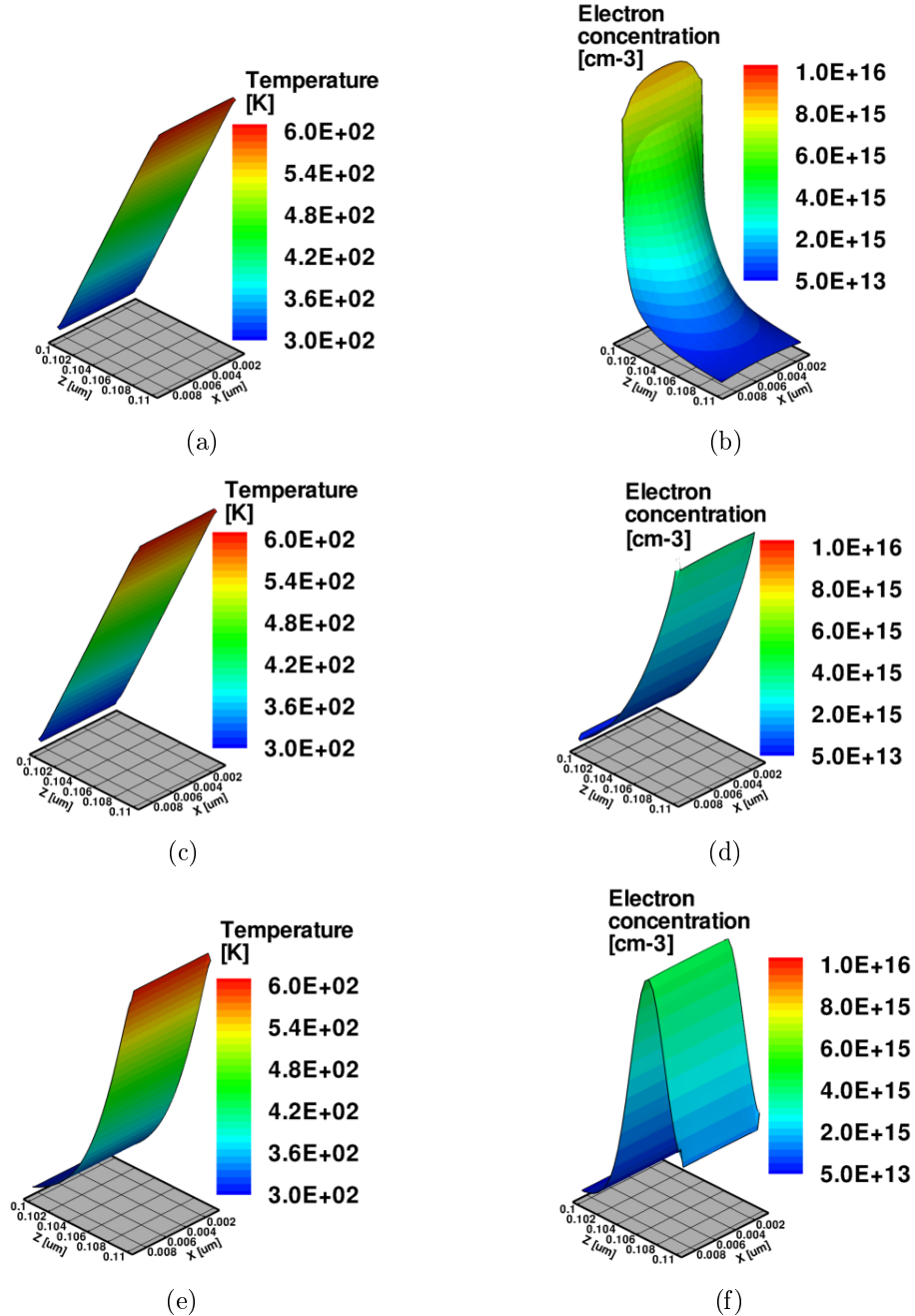


Figure 6.7: Test on heterogeneous AM properties:temperature fields and electron concentrations for set A (a-b), set B (c-d), and set C (e-f) of parameters. The images are obtained cutting the structure at $y = 0.005 \mu\text{m}$, then applying a transformation to the reference system. The xz -plane becomes the xy -plane, while along the z -axis there is the value of the variable.

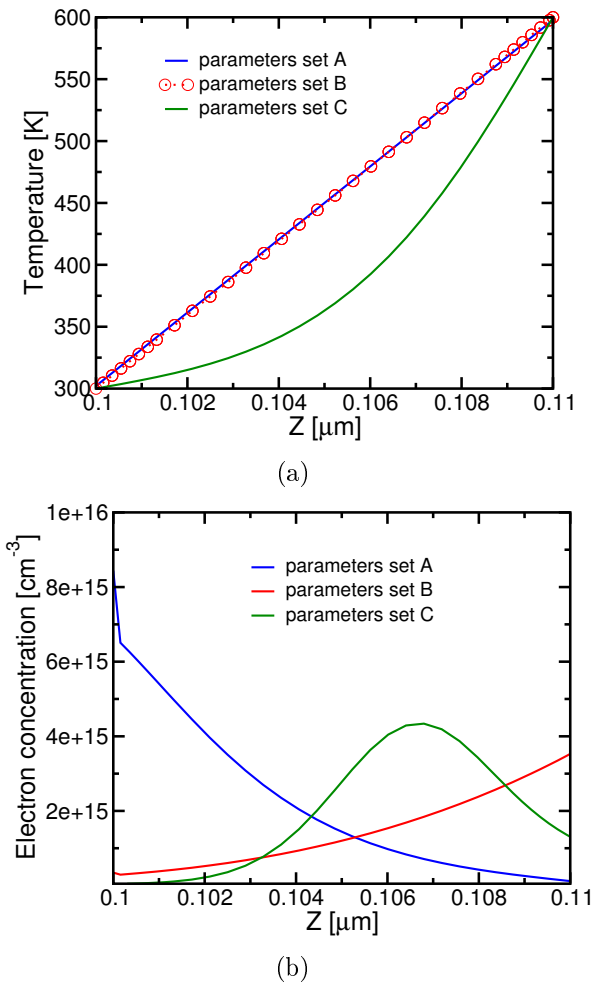


Figure 6.8: Test on heterogeneous AM properties: comparison of the temperature curves and of the electron concentrations along the z -axis. The images have been obtained cutting the structure at $x = 0.005 \mu\text{m}$ and then at $y = 0.005 \mu\text{m}$.

6.3 Thermo-Electric Transport in the Cylindrical Structure

All the simulations in this section are performed on the cylindrical structure (Fig. 4.6).

6.3.1 Electric transport

In this test we want to analyze the electron transport due to the electric field. In the case of the parallelepiped structure, since the potential curve was linear, the electric field was constant. Although the potential curve will still be linear along the radial direction, the electric field will not be constant over the cell because of its cylindrical geometry.

ϵ_r	σ_n^{M1}	σ_n^{M2}	v_{sat}	n_0	μ_0
10	$10^{17} \text{ S cm}^{-1}$	$10^{18} \text{ S cm}^{-1}$	10 M cm s^{-1}	10^{14} cm^{-3}	0.03 cm s^{-1}
c^{AM}		ϱ^{AM}	k^{AM}	α^{AM}	
$8.8 \text{ M cm}^2 \text{s}^{-2} \text{K}^{-1}$		3980 mg cm^{-3}	$0.3 \text{ W cm}^{-1} \text{K}^{-1}$	$100 \mu \text{V K}^{-1}$	

Table 6.7: Test on the electric transport in the cylindrical cell: parameters values.

Table 6.7 shows the values of the parameters used for this test. We impose homogeneous Neumann conditions for the continuity equation, and Dirichlet condition for the heat equation, with external temperature equal to 300 K . Fig. 6.9 shows the potential over the whole structure, and the electron concentration in the active material for different voltage applied at Γ_{C1}

$$\text{a-b)} \quad \bar{\varphi} = 1 \text{ V},$$

$$\text{c-d)} \quad \bar{\varphi} = 0 \text{ V}.$$

The images of the electron concentrations are obtained cutting the structure at $z = 0.005 \mu\text{m}$. Along the z -axis there is the value of the variable. The electrons show the expected behavior: they move towards the side of the structure where the potential is higher. In the case $\bar{\varphi} = 1 \text{ V}$, the electrons move outwards, accumulating at the surface Γ_{m1} , while, when $\bar{\varphi} = 0 \text{ V}$, they shift inwards and accumulate at Γ_{m2} .

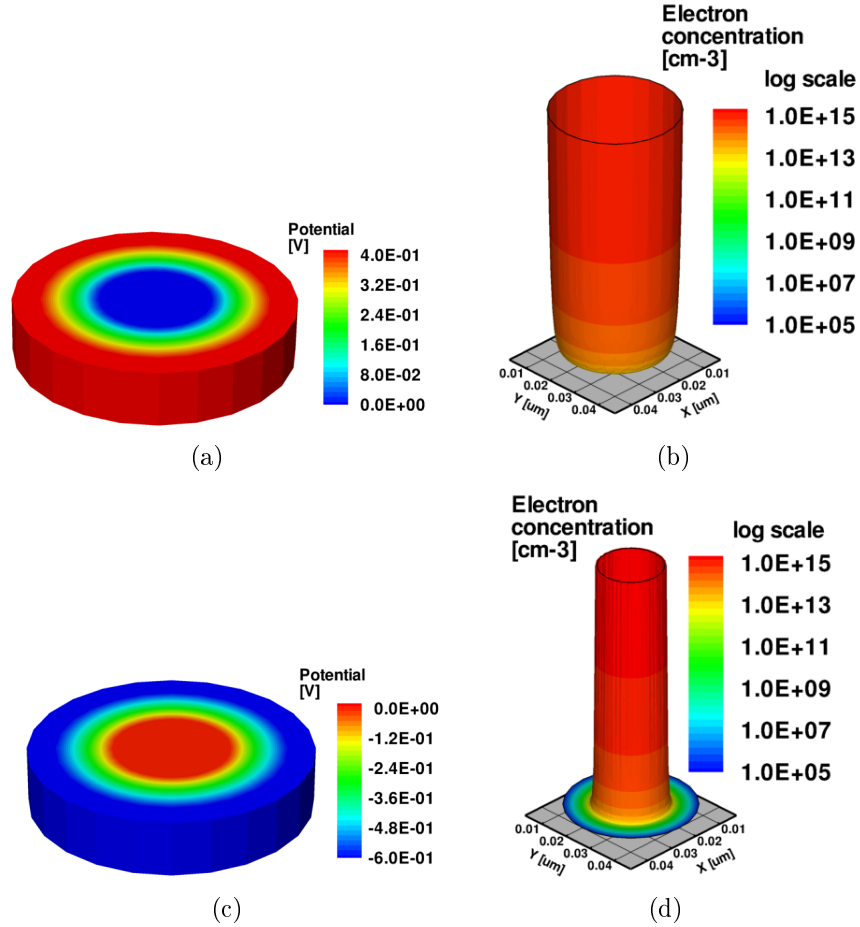


Figure 6.9: Test on the electric transport in the cylindrical cell: potential curves and corresponding electron concentration for different voltage applied. The images of the electron concentrations are obtained cutting the structure at $z = 0.005 \mu\text{m}$, with the value of the variable along the z -axis, while the potential curves are shown on the whole cell.

6.3.2 Electric field vs thermal field

We perform some simulations where electrons are affected by both the electric and the thermal field. We change the potential difference or the temperature gradient across the memory cell in order to see how this affects the electron distribution in the active material.

We impose the following Robin condition

$$-\mathbf{j}_n^{AM} \cdot \boldsymbol{\nu} = v_{rec}^n (n - 10^{18}) \quad \text{on } \Gamma_{m1} \quad \text{and} \quad -\mathbf{j}_n^{AM} \cdot \boldsymbol{\nu} = v_{rec}^n (n - 10^{14}) \quad \text{on } \Gamma_{m2} \cup \Gamma_{diel}$$

for the continuity equation, and

$$\begin{aligned} -\mathbf{j}_T^{AM} \cdot \boldsymbol{\nu} &= \gamma^T (T - T_{out}) \quad \text{on } \Gamma_{m1} \\ -\mathbf{j}_T^{AM} \cdot \boldsymbol{\nu} &= \gamma^T (T - 300) \quad \text{on } \Gamma_{diel} \\ -\mathbf{j}_T^{AM} \cdot \boldsymbol{\nu} &= \gamma^T (T - T_{in}) \quad \text{on } \Gamma_{m2} \end{aligned}$$

for the temperature equation. Table 6.8 shows the values of the parameters used in this test.

ϵ_r	σ_n^{M1}	σ_n^{M2}	v_{sat}	n_0	μ_0	v_{rec}^n
10	$10^{17} S cm^{-1}$	$10^{18} S cm^{-1}$	$10 M cm s^{-1}$	$10^{14} cm^{-3}$	$0.03 cm s^{-1}$	$20 K cm s^{-1}$
	c^{AM}	ϱ^{AM}	k^{AM}	α^{AM}	γ^T	
	$8.8 M cm^2 s^{-2} K^{-1}$	$3980 mg cm^{-3}$	$0.3 W cm^{-1} K^{-1}$	$10 \mu V K^{-1}$	$1000 W cm^{-2} K^{-1}$	

Table 6.8: Test on the thermal-electric transport in the cylindrical cell: parameters values.

First we fix the applied voltage at Γ_{C1} , $\bar{\varphi} = 1 V$, and we vary the imposed external temperatures at Γ_{m1} and Γ_{m2} . Therefore the potential curve is the one in Fig. 6.9(a), while figure 6.10 shows the temperature fields and the electron concentrations corresponding to the values

$$\text{a-b)} \quad T_{in} = 300 K \text{ and } T_{out} = 600 K,$$

$$\text{c-d)} \quad T_{in} = 600 K \text{ and } T_{out} = 300 K,$$

$$\text{e-f)} \quad T_{in} = 300 K \text{ and } T_{out} = 900 K.$$

All the images are obtained cutting the structure at $z = 0.005 \mu m$. In the electron concentration graphs, along the z -axis there is the value of the variable. The electric field tends to bring the electrons towards Γ_{m1} (where the potential is higher). When the temperature curve is the one shown in Fig. 6.10(a), the resulting thermal field is opposed to the electric field. Therefore the thermal field reduces the effect of the electric field. When the temperature gradient is the one shown in Fig. 6.10(b), both the thermal and the electric field urge the electrons outwards. Then, in Fig. 6.10(d) the electron concentration at Γ_{m2} is lower than in Fig. 6.10(b), while it has increased in the rest of the cell. In the case of Fig. 6.10(e), the temperature gradient is opposed to the electric field, but larger than the one in Fig. 6.10(a). Therefore the effect of the electric field is almost canceled, and, as a result, the active material has a lower electron concentration.

Then we fix the external temperatures $T_{in} = 300 K$ and $T_{out} = 600 K$, thus the temperature in the active material is the one illustrated in Fig. 6.10(a). This time we vary the voltage applied to Γ_{C1} . Figure 6.11 shows the potential curves and the electron concentrations corresponding to the values

$$\text{a-b)} \quad \bar{\varphi} = 0.5 V,$$

$$\text{c-d)} \quad \bar{\varphi} = 1 V,$$

$$\text{e-f)} \quad \bar{\varphi} = 1.5 V.$$

The images of the electron concentrations are obtained cutting the structure at $z = 0.005 \mu m$, with the value of the variable along the z -axis, while the potential curves are shown on the whole cell. The imposed temperature gradient tends to bring the electrons outwards. The potential of Fig. 6.11(a) creates an opposed electric field. As a result, the electrons barely move towards Γ_{m1} . The potential curves in Fig. 6.11(c) and (e) generate rising electric fields with the same direction of the thermal gradient. Therefore the electrons move outwards, and their concentration at the surface Γ_{m1} increases with the external voltage applied.

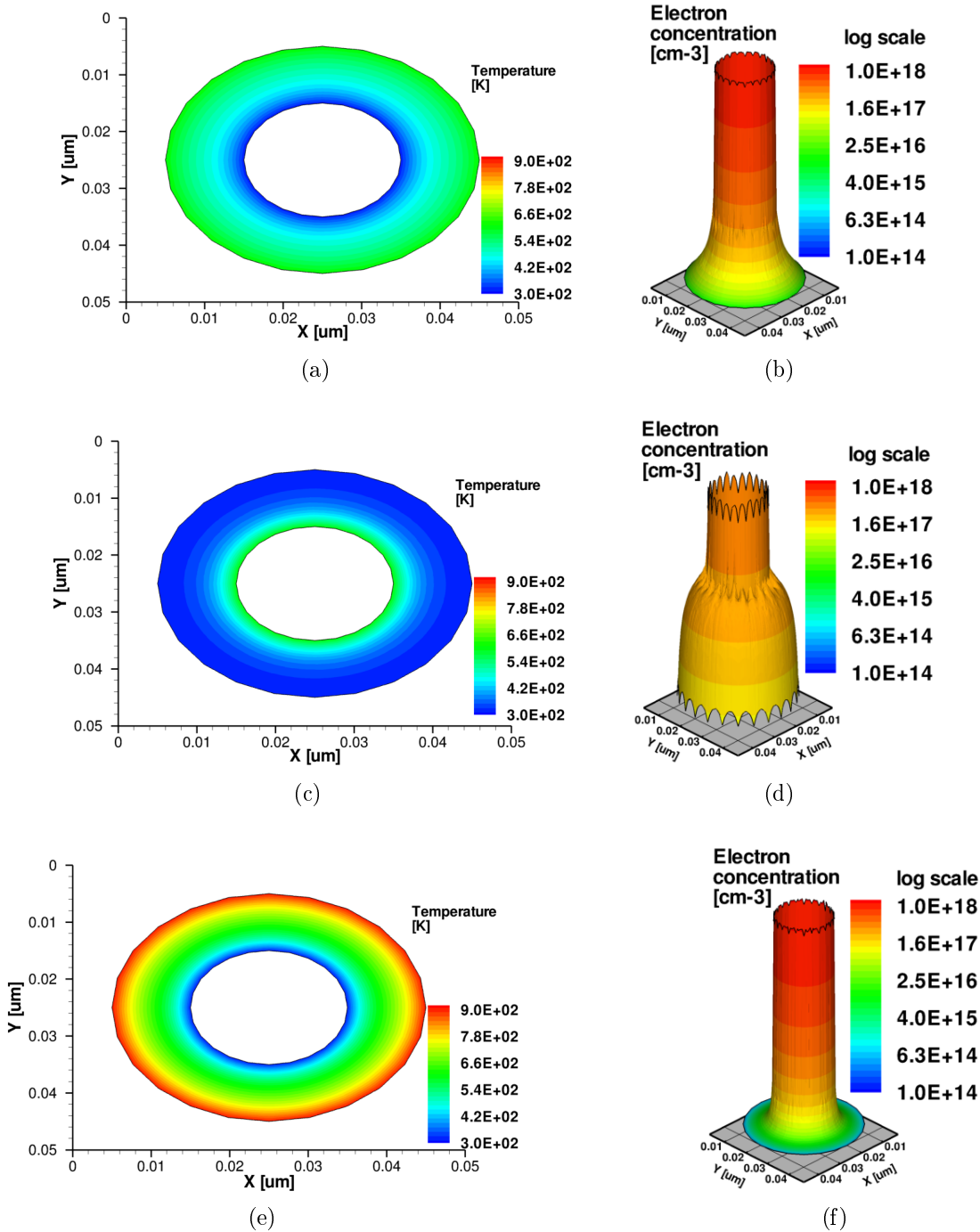


Figure 6.10: Test on the thermal-electric transport in the cylindrical cell: temperature curves and electron concentrations for different values of the external temperatures in the boundary conditions. All the images are obtained cutting the structure at $z = 0.005 \mu m$. In the electron concentration graphs, along the z -axis there is the value of the variable.

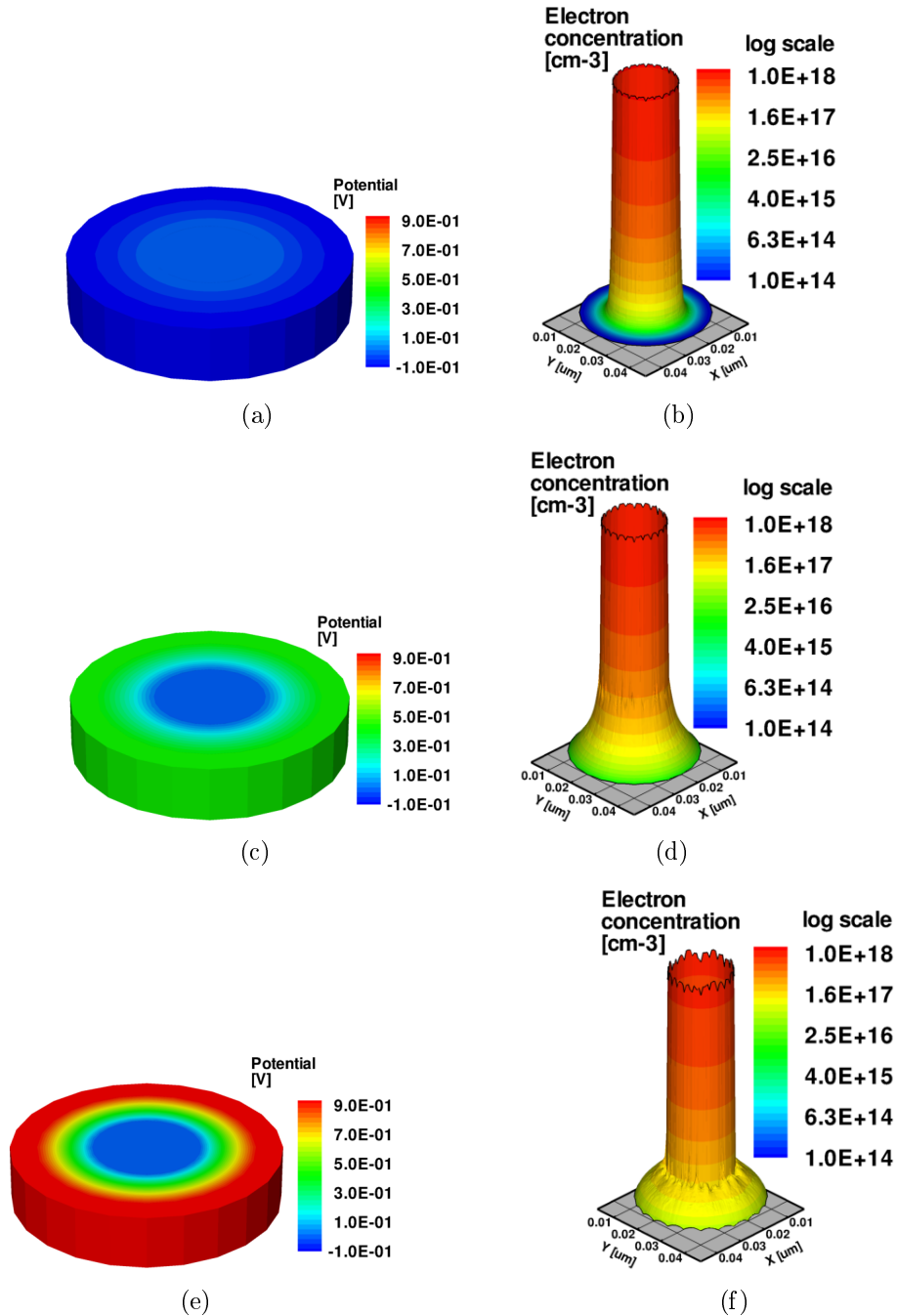


Figure 6.11: Test on the thermal-electric transport in the cylindrical cell: temperature curves and electron concentrations for different values of the voltage applied to Γ_{C1} . The images of the electron concentrations are obtained cutting the structure at $z = 0.005 \mu\text{m}$, with the value of the variable along the z -axis, while the potential curves are shown on the whole cell.

Conclusions and Future Works

In this MD Thesis, we have presented a mathematical model aiming to describe physical processes occurring in a generic resistive memory cell. Great efforts have been achieved in order to make the theoretical model as general as possible. We accomplished our goal: we provide a valid tool that can be used to investigate, through numerical simulations, the operation of the memory cell. The model focuses on the following aspects:

- it computes the electrostatic potential on the whole cell solving a general Poisson equation which considers both metals and non metallic materials,
- it computes the electron concentration in the most significant part of the cell, considering the electric field and the temperature gradient across the structure as driving forces of the electron transport,
- it computes the temperature in the memory cell, considering the electron drift current as the stream carrying the temperature and as the factor responsible, along with the electric field, for the joule heating.

In order to solve the non-linear system consisting of the three model equations, we used a functional iterations scheme which has proved to have a good robustness and convergence rate in all the simulation tests.

Concerning the numerical discretization of the proposed model, we chose the implicit Euler method for the discretization in time. As regards the space discretization we used the standard Galerkin \mathbb{P}^1 finite element method for the general Poisson equation, while for the other equations, we preferred a monotone \mathbb{P}^1 finite element scheme in order to correctly describe the required properties of flux conservation and positivity of the computed solutions. To fulfill these requirements, we selected a nodal-based exponentially fitted scheme called the Finite Volume Scharfetter-Gummel method. The chosen method have been successfully tested in three dimensional problems and with different domain geometries. Validation tests have been run to prove the accuracy of

the solutions computed by our code. In all simulations discrete maximum principle have been shown to hold, under appropriate constraints on the finite element meshes.

Despite our best efforts, there are still many issues to be addressed: the development of a module concerning the mechanical stress issues, and of a module allowing to treat semiconductor materials.

From the mathematical point of view, it would also be interesting to allow the user to choose different discretization methods. It would be helpful to include a primal or dual mixed formulation ([56, 57]) since these are particularly suited for the type of equations in the model. Finally an issue of great interest would be to seek alternative resolution algorithms that can provide a more rapid convergence.

Ringraziamenti

Questa tesi è il risultato di un anno di lavoro, un anno durante il quale ci sono stati molti momenti in cui ho davvero pensato che non ce l'avrei mai fatta. Se ci sono riuscita è merito di tante persone che mi sono state vicino e non mi hanno mai fatto mancare il loro sostegno. Primo fra tutti voglio ringraziare il mio tutor Aurelio, che durante il mio stage mi ha insegnato moltissimo, e non solo dal punto di vista lavorativo. Desidero poi ringraziare il mio relatore Riccardo Sacco che mi ha sempre incoraggiata e non ha mai smesso di credere nelle mie capacità. Un sentito ringraziamento infine va al Professor Verri che ci ha fornito un preziosissimo aiuto.

Voglio poi ringraziare i compagni di questa mia avventura, Giovanni e Giulio, le mie amiche di sempre, Viola, Marta, Sara, Lina e la Zia, gli amici e le amiche degli Heroes e in particolare Leila, la Fede e Gabbo, gli amici dell'università con cui ho condiviso gli ultimi cinque anni della mia vita, in modo particolare Laura.

Un immenso ringraziamento va alla mia famiglia, che mi ha fatto sentire più che mai tutto il suo amore e supporto, a Marco che anche dall'altra parte del mondo è riuscito a starmi vicino e infine alla mia “famiglia” alassina che attraverso telefonate e mail non ha mai smesso di farmi sentire il suo affetto.

Bibliography

- [1] Pavan, P., Bez, R., Olivo, P., Zanoni, E., *Flash Memory cells-An Overview*, IEEE Proceedings, 85, 1248-1271 (1997)
- [2] Taur, Y., Ning, T. H., *Fundamentals of Modern VLSI Devices*, Cambridge (2009)
- [3] Rubinstein, I., *Electro-Diffusion of Ions*, SIAM (1990)
- [4] Aritome, S., Shirota, R., Hemink, G., Endoh, T., Masuoka, F., *Reliability Issues of Flash Memory Cells*, IEEE Proceedings, 81, 776-788, (1993)
- [5] Prall, K., *Scaling Non-Volatile Memory below 30 nm*, IEEE Non-Volatile Semiconductor Memory Workshop, 22, 5-9 (2007)
- [6] Valov, I., Waser, R., Jameson, J. R., Kozicki, M. N., *Electrochemical metalization memories - fundamentals, application, prospects*, Nanotechnology, 22 (2011)
- [7] Ielmini, D., *Filamentary-switching model in RRAM for time, energy and scaling projections*, IEDM Tech. Dig., 409-412 (2011)
- [8] Kozicki, M. N., Gopalan, C., Balakrishnan M., Park, M., Mitkova, M., *Non-volatile memory based on solid electrolytes NVMTS*, Proc. Non-Volatile Memory Technology Symp., 10 (2004)
- [9] Schindler, C., Thermadam, S. C. P., Waser, R., Kozicki, M. N., *Bipolar and unipolar resistive switching in Cu-doped SiO₂*, IEEE Trans. Electron Devices, 54 (2007)
- [10] Galatsis, K., Wang, K., Botros, Y., Yang, Y., Xie, Y. H., Stoddart, J. F., Kaner, R. B., Ozkan, C., Liu, J., Ozkan, M., Zhou, C., Kim, K. W., *Emerging Memory Devices: Nontraditional Possibilities Based on Nanomaterials and Nanostructures*, IEEE Circuits & Devices Magazine, 6, 12-21 (2006)

- [11] Waser, R., Dittman, R., Staikov, G., Szot, K., *Redox-based Resistive Switching Memories - Nanoionic Mechanisms, Prospects and Challenges*, Adv. Material, 21, 2632-2663 (2009)
- [12] *The International Technology Roadmap for Semiconductors*, ITRS 2011 Edition, <http://www.itrs.net> (2011)
- [13] Aratani, K., Ohba, K., Mizuguchi, T., Yasuda, S., Shiimoto, T., Tsushima, T., Sone, T., Endo, K., Kouchiyama, A., Sasaki, S., Maesaka, A., Yamada, N., Narisawa, H., *A Novel Resistance Memory with High Scalability and Nanosecond Switching*, IEDM Techn. Dig., 783-786 (2007)
- [14] Kund, M., Beitel, G., Pinnow, C. U., Röhr, T., Schumann, J., Symanczyk, R., Ufert, K. D., Müller, G., *Conductive bridging RAM (CBRAM): An emerging non-volatile memory technology scalable to sub 20nm*, IEDM Techn. Dig., 754-757 (2005)
- [15] Sakamoto, T., Sunamura, H., Kawaura, H., Hasegawa, T., Nakayama, T., Aono, M., *Nanometer-scale switches using copper sulfide*, Appl. Phys. Lett., 82 (2003)
- [16] Gopalan C., Ma, Y., Gallo, T., Wang, J., Runnion, E., Saenz, J., *Koushan, F., Hollmer, S., Demonstration of Conductive Bridging Random Access Memory (CBRAM) in Logic CMOS Process*, Proc. IEEE Int. Memory Workshop, 50-53 (2010)
- [17] Kaeriyama, S., Sakamoto, T., Sunamura, H., Mizuno, M., Kawaura, H., Hasegawa, T., Terabe, K., Nakayama, T., Aono, M., *A nonvolatile programmable solid-electrolyte nanometer switch*, IEEE J. Solid-State Circuits, 40 (2005)
- [18] Dietrich, S., Angerbauer, M., Ivanov, M., Gogl, D., Hoenigschmid, H., Kund, M., Liaw, C., *A nonvolatile 2 Mbit CBRAM memory core featuring advanced read and program control*, IEEE J. Solid-State Circuits, 42 (2007)
- [19] Wong, P., Raoux, S., Kim, S., Liang, J., Reifenberg, J. P., Rajendran, B., Asheghi, M., Goodson, K. E., *Phase Change Memory*, IEEE Proceedings, 98, 2201-2227 (2010)
- [20] Ielmini, D., Lacaita, A. L., *Phase change materials in non-volatile storage*, Materials Today, 14, 600-607 (2011)

- [21] Gleixner, B., Pirovano, A., Sarkar, J., Ottogalli, F., Tortorelli, E., Tosi, M., Bez, R., *Data retention characterization of phase-change memory arrays*, Proc. 45th Annu. IEEE Int. Reliab. Phys. Symp., 542–546 (2007)
- [22] Atwood, G., Bex, R., *Current status of Chalcogenide phase change memory*, Device Research Conference Digest, 63, 29-33 (2005)
- [23] Ielmini, D., *Threshold switching mechanism by high-field energy gain in the hopping transport of chalcogenide glasses*, Phys. Rev., 78, 035308 (2008)
- [24] Pirovano, A., Lacaita, A. L., Benvenuti, A., Pellizer, F., Hudgens, S., Bex, R., *Scaling Analysis of Phase-Change Memory Technology*, Proc. IEEE Int. Electron Devices Meeting, 29.6.1–29.6.4. (2003)
- [25] Pirovano, A., Lacaita, A. L., Pellizzer, F., Kostylev, S. A., Benvenuti, A., Bez, R., *Low-field amorphous state resistance and threshold voltage drift in chalcogenide materials*, IEEE Trans. Electron Devices, 51, 714–719 (2004)
- [26] Boniardi, M., Redaelli, A., Pirovano, A., Tortorelli, I., Ielmini, D., Pellizzer, F., *A physics-based model of electrical conduction decrease with time in amorphous $Ge_2Sb_2Te_5$* , J. Appl. Phys., 105, 084506 (2009)
- [27] Reifenberg, J. P., *Thermal phenomena in phase change memory*, Ph.D. dissertation, Stanford Univ. (2010)
- [28] Lee, B. C., Ipek, E., Mutlu, O., Burger, D., *Phase Change Memory Architecture and the Quest for Scalability*, Communicaton of the ACM, 53, 99-106 (2010)
- [29] Xiong, F., Liao, A., Estrada, D., Pop, E., *Low-power Switching of Phase-Change Materials with Carbon Nano Tube Electrodes*, online in Science Express (2011)
- [30] Owen, A. E., Robertson, J. M., Main, C., *The threshold characteristics of chalcogenide-glass memory switches*, J. Non-Crystalline Solids, 32, 29–52 (1979)
- [31] Liang, J., Jeyasingh, R.G.D., Chen, H-Y., Wong, H-S. P., *A $1.4\mu A$ Reset Current Phase Change Memory Cell with Integrated Carbon Nanotube Electrodes for Cross-Point Memory Application*, Symp. VLSI Technology, 5B-4 (2011)
- [32] Kim, I.S., Cho, S.L., Im, D.H., Cho, E.H., Kim, D.H., Oh, G.H., Ahn, D.H., Park, S.O., Nam, S.W., Moon, J.T., Chung, C.H., *High Performance PRAM Cell*

- Scalable to Sub-20nm Technology with below 4F2 Cell Size, Extendable to DRAM Applications*, Symp. VLSI Technology, 19-3 (2010)
- [33] Cheremisin, M. V., *Peltier Effect Related Correction to Ohmic Resistance*, Semiconductor Device Research Symp., 274-277 (2001)
 - [34] Consiglieri, L., *On the posedness of thermoelectrochemical coupled systems*, Eur. Phys. J. Plus, 128 (2013)
 - [35] De Falco, C., *Quantum corrected drift-diffusion models and numerical simulation of nanoscale semiconductor device*, PhD thesis in Mathematics and Statistics for Computational Sciences, Università degli studi di Milano (2006)
 - [36] Selberherr, S., *Analysis and Simulation of Semiconductor Devices*, Springer Verlag (1984)
 - [37] Jerome, J. W., *Analysis of Charge Transport*, Springer-Verlag (1996)
 - [38] Canali, C., *Electron and Hole Drift Velocity Measurements in Silicon and Their Empirical Relation to Electric Field and Temperature*, IEEE Trans. Electron Devices, 22, 1045-1047 (1975)
 - [39] Tritt, T. M., *Thermoelectric Materials: Principles, Structure, Properties, and Applications*, Encyclopedia of Materials: Science and Technology, Elsevier Science Ltd, 1-11 (2002)
 - [40] Ashcroft, N. W., Mermin, N. D., *Solid State Physics*, Saunders College (1976)
 - [41] Speyer, R. F., *Material Engineering Series*, Vol 8: *Thermal Analysis of Materials*, Taylor & Francis (1994)
 - [42] Landau, L.D., Lifshitz, E. M., *Course of Theoretical Physics*, Vol 8: *Electrodynamics of Continuous Media*, Pergamon Press (1960)
 - [43] Bank, R. E., Coughram, W. M. Jr., Cowsar, L. C., *The Finite Volume Sharfetter-Gummel method for steady convection diffusion equation*, Computing and Visualization in Science, 1, 123-136 (1998)
 - [44] Ciampolini, P., Pierantoni, A., Liuzzo, A., Baccarani, G., *3D Simulations of Silicon Devices: Physical Models and Numerical Algorithms*, Process and Device Modeling for Microelectronics, Elsevier Science, 53-101 (1993)

- [45] Xu, Z., Zikatanov, L., *A Monotone Finite Element Scheme for Convection-Diffusion Equation*, Mathematics of Computation, 228, 1429-1446 (1999)
- [46] Lazarov, R. D., Zikatanov, L., *An Exponential Fitting Scheme for General Convection-Diffusion Equation of Tetrahedral Meshes*, Computational and Applied Math., 92, 60-69 (2005)
- [47] Gatti, E., Micheletti, S., Sacco, R., *A New Galerkin Framework for the Drift-Diffusion Equation in Semiconductors*, East West J. Numer. Math., 6, 101–135 (1998)
- [48] Varga, R.S., *Matrix Iterative Analysis*, Prentice-Hall, Englewood Cliffs (1962)
- [49] Quarteroni, A., *Modellistica numerica per problemi differenziali*, Springer-Verlag (2006)
- [50] Quarteroni, A., Sacco, R., Saleri, F., *Matematica Numerica*, Springer-Verlag (2008)
- [51] Salsa, S., *Equazioni a Derivate Parziali, metodi, modelli e applicazioni*, Springer-Verlag (2010)
- [52] Ciarlet, P.G., *The Finite Element Method for Elliptic Problems*, Elsevier (1978)
- [53] Tong, P., Rossettos, J. N., *Finite Element Method, basic technique and implementation*, Dover Publications (2008)
- [54] Bank, R. E., Rose, D. J., Fichtner, W., *Numerical Methods for Semiconductor Device Simulation*, IEEE Trans. Electron Devices, 30, 1031-1041 (1983)
- [55] Buturla, E. M., et al., *Finite-Element Analysis of Semiconductor Devices: The FIELDAY Program*, IBM J. of Research and Development, 25, 218-231 (1981)
- [56] Brezzi, F., Fortin, M., *Mixed and Hybrid Finite Element Methods*, Springer-Verlag (1991)
- [57] Roberts, J., Thomas, J. M., *Mixed and Hybrid Methods*, Handbook of Numerical Analysis 2, Finite Elements Methods - part I, P.G. Ciarlet and J.L.Lions, Elsevier Science, 523-639 (1991)